

**MICROPHYSICAL PROCESSES OF VOLCANIC ASH  
AGGREGATION AND THEIR IMPLICATIONS FOR VOLCANIC  
ERUPTION DYNAMICS**

A Dissertation  
Presented to  
The Academic Faculty

by

Jennifer Whitney Telling

In Partial Fulfillment  
of the Requirements for the Degree  
Doctor of Philosophy in the  
School of Earth and Atmospheric Sciences

Georgia Institute of Technology  
December 2013

**COPYRIGHT 2013 BY JENNIFER WHITNEY TELLING**

**MICROPHYSICAL PROCESSES OF VOLCANIC ASH  
AGGREGATION AND THEIR IMPLICATIONS FOR VOLCANIC  
ERUPTION DYNAMICS**

Approved by:

Dr. Josef Dufek, Advisor  
School of Earth and Atmospheric  
Sciences  
*Georgia Institute of Technology*

Dr. James Wray  
School of Earth and Atmospheric  
Sciences  
*Georgia Institute of Technology*

Dr. Andrew Newman  
School of Earth and Atmospheric  
Sciences  
*Georgia Institute of Technology*

Dr. Christian Huber  
School of Earth and Atmospheric  
Sciences  
*Georgia Institute of Technology*

Dr. Athanasios Nenes  
School of Chemical and Biomolecular  
Engineering  
*Georgia Institute of Technology*

Date Approved: August 8, 2013

For my Grandma, Irma Allardt Telling

## ACKNOWLEDGEMENTS

I would like to thank my advisor, Dr. Joe Dufek, for his continued support and encouragement. His input and advice have been invaluable and have helped me to become a better researcher. Thank you to the Dufek group: Mary, Ozge, Joe, Josh and Cindy, for their encouragement, support and willingness to act as a great sounding board. Thank you to Wim for the great advice that kick-started the writing of my thesis, and to Zach for all of the help with ArcGIS. I would also like to thank my committee for their involvement and aid.

I cannot thank my friends enough for all of their love and support these five years. I greatly appreciate everyone in the YJCF and at St. Thomas for understanding when work needed to come first and for distracting me when I needed a diversion. I would like to thank my graduate student friends who graduated before me and who have always been a great source of advice and support. Lastly, I would especially like to thank Cindy, John, Billy, Manny, Akshay and Erin for always being there to pick me up and make me laugh.

Lastly, I would like to thank God, my parents, my Aunt Mary and Shahin. Mom and Dad have been unwavering in their support and high expectations. I would like to thank my Aunt Mary for her advice and wisdom, which has always reminded me of the things that are most important in life. Lastly, I would like to thank Shahin for always being there to encourage, calm and support me ,and for always being ready with some ice cream when all else failed.

This work was supported by the Earth and Atmospheric Science Department at Georgia Tech and NSF grants EAR-0809321, 1144585, 1150794 and NASA Award Number NNX09AL20G, and I greatly appreciate the support.

# TABLE OF CONTENTS

|  | Page |
|--|------|
| ACKNOWLEDGEMENTS   | iv   |
| LIST OF TABLES   | viii |
| LIST OF FIGURES  | ix   |
| NOMENCLATURE   | xi   |
| SUMMARY  | xiii |
| <br><u>CHAPTER</u>   |      |
| 1 Introduction   | 1    |
| 2 Ash Aggregation Efficiency: The Effect of Collisional Energy | 8    |
| 2.1 Introduction   | 8    |
| 2.2 Methods  | 12   |
| 2.2.1 Experimental Setup                                       | 12   |
| 2.2.2 Data Collection  | 14   |
| 2.2.3 Post Processing  | 15   |
| 2.3 Results  | 20   |
| 2.4 Collision and Aggregation Mechanisms                       | 25   |
| 2.4.1 Wet Aggregation Processes                                | 26   |
| 2.4.2 Dry Aggregation Processes                                | 29   |
| 2.5 Conclusions  | 30   |
| 3 Ash Aggregation Efficiency: The Role of the Atmosphere       | 32   |
| 3.1 Introduction   | 32   |
| 3.2 Methods  | 34   |
| 3.3 Results  | 38   |

|   |    |
|---|----|
| 3.4 Discussion  | 40 |
| 3.4.1 Determining Wet and Dry Flow Regimes                  | 41 |
| 3.4.2 Stokes Number Analysis                                | 42 |
| 3.4.3 The Inertial-Electrostatic Ratio                      | 47 |
| 3.4.4 Implications for Volcanic Modeling                    | 49 |
| 3.5 Conclusions   | 53 |
| 4 Modeling Ash Aggregation at Kilauea                       | 55 |
| 4.1 Introduction  | 55 |
| 4.2 Methods   | 61 |
| 4.2.1 Model Characterization                                | 61 |
| 4.2.2 Incorporating Aggregation                             | 62 |
| 4.2.3 Topographic and Atmospheric Characteristics           | 64 |
| 4.2.4 Simulations   | 68 |
| 4.3 Results   | 68 |
| 4.4 Discussion  | 74 |
| 4.5 Conclusions   | 76 |
| 5 Conclusions   | 78 |
| 6 Continuing Work   | 82 |
| 6.1 Ash Dispersal and Aggregation Mechanisms                | 82 |
| 6.2 Volcanic Modeling                                       | 87 |
| 6.3 Planetary Applications                                  | 90 |
| APPENDIX A: Table of Experiment 1 Physical Run Parameters   | 91 |
| APPENDIX B: Table of Experiment 2 Physical Run Parameters   | 94 |
| APPENDIX C: Range of Eruptive Conditions at Kilauea Volcano | 97 |
| REFERENCES  | 98 |

## LIST OF TABLES

|   | Page |
|---|------|
| Table 2.1: Summary of previous coalescence efficiency studies | 10   |
| Table 4.1: Model initial particle size distribution           | 62   |

## LIST OF FIGURES

|   | Page |
|---|------|
| Figure 2.1: Diagram of the full experimental setup  | 14   |
| Figure 2.2: Diagram of particle location algorithm  | 16   |
| Figure 2.3: Raw image of particles experiencing light scattering effect   | 18   |
| Figure 2.4: Particle size distribution for ash and SiO <sub>2</sub> samples   | 22   |
| Figure 2.5: Aggregation efficiency as a function of relative humidity   | 23   |
| Figure 2.6: Aggregation efficiency as a function of CKE   | 25   |
| Figure 2.7: A comparison of aggregation efficiency- CKE studies   | 27   |
| Figure 3.1: Experimental chamber  | 35   |
| Figure 3.2: Aggregation efficiency as a function of collision kinetic energy<br>in four defined flow regimes                          | 39   |
| Figure 3.3: Aggregation efficiency as a function of residence time  | 40   |
| Figure 3.4: Aggregation efficiency as a function of Stokes number   | 44   |
| Figure 3.5: Aggregation efficiency and restitution coefficient, theoretical<br>and experimental relationships                         | 46   |
| Figure 3.6: Inertial-electrostatic ratio  | 48   |
| Figure 3.7: Probabilistic fits of aggregation efficiency to collision kinetic<br>for the dry and wet flow regimes                     | 52   |
| Figure 3.8: Probabilistic fit of aggregation efficiency to collision kinetic<br>energy for the full range of energies in the wet case | 53   |
| Figure 4.1: USGS map of Kilauea Volcano   | 56   |
| Figure 4.2: USGS photos of AL from the Footprints Ash, Kilauea  | 59   |
| Figure 4.3: Topographic map of Kilauea with AL distribution   | 59   |

|   |    |
|---|----|
| Figure 4.4: Description of the topographic profile used for modeling    | 65 |
| Figure 4.5: Wind speed and direction data for 2 months at PHTO          | 67 |
| Figure 4.6: Representative atmospheric soundings at Kilauea             | 67 |
| Figure 4.7: Mass of aggregates developing with time at Kilauea          | 70 |
| Figure 4.8: Relative humidity and aggregation rate for Ash-1 at 150 s   | 71 |
| Figure 4.9: Relative humidity and aggregation rate for Ash-2 at 150 s   | 71 |
| Figure 4.10: Relative humidity and aggregation rate for Ash-3 at 150 s  | 72 |
| Figure 4.11: Volume fraction for Ash-1, Ash-2, Ash-3 and Ash-4 at 150 s | 72 |
| Figure 4.12: Relative humidity and aggregation rate for Ash-2 at 100 s  | 73 |
| Figure 4.13: Volume fraction for Ash-2 at 100 s                         | 74 |

## NOMENCLATURE

|                                    |  |                                   |
|------------------------------------|--|-----------------------------------|
| 1, 2                               |  | Particle identifier               |
| d                                  |  | Particle diameter (m)             |
| dt                                 |  | Image time step (s)               |
| E                                  |  | Kinetic energy, CKE (J)           |
| $E_{elec}, E_{hyd}$                | Dissipative energy in charged and hydrous collisions         |                                   |
| $E_{acc}, E_b, E_{diss}, E_{visc}$ |  | Dissipative energy terms          |
| e                                  |  | Restitution coefficient           |
| $F_{aggr}$                         |  | Fractional aggregation            |
| $f_E$                              | Probability distribution for ash variability                 |                                   |
| $f_{coll}$                         | Probability distribution for collisional velocity            |                                   |
| $ff_{aggregate}$                   | Joint probability distribution for collision and aggregation |                                   |
| i,j                                |  | x, y component                    |
| k                                  |  | Coulomb's Constant ( $Nm^2/C^2$ ) |
| m                                  |  | Particle mass (kg)                |
| $m', m^*$                          |  | Reduced mass (kg)                 |
| n                                  |  | Image index number                |
| q                                  |  | Particle charge (C)               |
| r                                  |  | Particle radius (m)               |
| $r', r^*$                          |  | Reduced radius (m)                |
| s                                  |  | Particle location constant        |
| St                                 |  | Particle Stokes number            |
| $t_i$                              |  | Particle interaction time (s)     |
| u, v                               |  | Velocity component (m/s)          |

|                        |                                       |
|------------------------|---------------------------------------|
| $w$                    | Approach velocity (m/s)               |
| $x$                    | Physical coordinate (m)               |
| $\varepsilon$          | Aggregation efficiency                |
| $\theta$               | Granular temperature                  |
| $\mu$                  | Viscosity (Pa·s)                      |
| $\rho, \rho_p$         | Particle density (kg/m <sup>3</sup> ) |
| $\sigma_{\text{diss}}$ | Dissipative energy variance           |
| $\tau_i$               | Interaction time (s)                  |
| $\tau_r$               | Rebound time (s)                      |

## SUMMARY

Although numerous hazard models exist to assess possible ash fallout from explosive volcanic eruptions around the world, these models frequently neglect to consider ash aggregation or use a simple percent proxy to represent aggregation, without considering the varying processes at work throughout the volcanic flow. Eruption dynamics are sensitive to ash aggregation, and ash aggregates are commonly found in eruptive deposits, yet few experiments have been conducted on aggregation phenomena using natural materials. In this work, experiments were developed to produce both probabilistic and process-based relationships for the efficiency of ash aggregation with respect to particle size, collision kinetic energy, atmospheric water vapor and residence time. A synthetic ash proxy, ballotini, and ash from the 2006 eruption of Tungurahua, Ecuador, and the 1980 eruption of Mount St. Helens, WA, were examined for their aggregation potential.

Two aggregation regimes, wet and dry, were identified based on their potential for aggregation. The wet flow regime occurs when particles are circulated in high relative humidity environments long enough to develop a water layer with a thickness that exceeds the particle roughness scale. Hydrodynamic forces control aggregation in the wet flow regime. The dry flow regime includes particles in low relative humidity environments as well as those that circulate too briefly in high humidity environments to fully develop a water layer. Electrostatic forces control aggregation in the dry flow regime. Aggregation efficiency in both regimes was dominantly controlled by collision kinetic energy; however, this effect is significantly dampened in the wet flow regime.

Equations governing the relationships between aggregation efficiency, collision kinetic energy and the related forcings in the wet or dry flow regimes have been developed for implementation into large-scale numerical volcanic models.

The results of this experimental work have been developed into a probability distribution that has been integrated and incorporated into a multifluid numerical model. The numerical simulation was tested on a range of explosive depths and overpressure estimates from the 1790 eruption of Kilauea volcano, HI. The model output was compared to field data collected on the deposit thickness moving away from the source and the distribution, including both size and density, of aggregates. The mass fraction of ash removed from the eruption column in the form of aggregates was also calculated to examine how efficiently aggregation processes remove ash throughout the eruption. Cumulatively, the work presented here furthers our understanding of aggregation processes and the role they play in volcanic eruptions.

# CHAPTER 1

## INTRODUCTION

Explosive volcanic eruptions inject gasses, ash and other volcanic material into the atmosphere. A buoyant eruption column, which forms when the bulk density of the plume is less than that of the surrounding atmosphere, can extend tens of kilometers into the atmosphere, reaching the stratosphere (Carslaw et al., 2009; Niemeier et al., 2009). Collapsing columns, which have a higher density than the surrounding atmosphere, can form pyroclastic density currents (PDC's), which can travel tens of kilometers away from the volcanic vent (Brown et al., 2010) at speeds on the order of 100 m/s (Bursik and Woods, 1996). These eruptions pose substantial hazards for local communities (Gislason et al., 2011; Hall et al., 1999), regional areas (Gislason et al., 2011; Schumann et al., 2011) and aviation (Prata and Tupper, 2009; Schumann et al., 2011).

Depending on the type, buoyant or collapsing, size and duration of volcanic eruption, eruptive clouds can last on the order of days to years (Carslaw et al., 2009; Niemeier et al., 2009). Fine ash, which corresponds roughly in diameter to the coarse aerosol mode, typically has a lifetime on the order of days (Gislason et al., 2011; Niemeier et al., 2009). However, very fine ash, corresponding to the accumulation aerosol mode, can remain in the atmosphere for months to years if the eruption column reached the stratosphere (Niemeier et al., 2009). Carslaw et al. (2009) and Robock (2000) report a number of eruptions, including Grimsvötn in 1783, El Chichón in 1982 and Mt Pinatubo in 1991, that affected regional or global climate for years.

Increased volcanic monitoring over the last few decades has helped mitigate the risk posed to communities living around some volcanoes (Gislason et al., 2011). However, Folch (2012) and Taddeucci et al. (2011) both emphasize that significant improvements are needed in plume forecasting to be better able to predict and mitigate airborne volcanic hazards. In particular, the gap between volcanic and atmospheric aerosol transport models needs to be addressed (Folch, 2012).

The size and composition of volcanic ash depends on the source and type of eruption. Volcanic ash can refer to anything smaller than 2 mm in size (Rose and Durant, 2009). Particles larger than 2 mm are called aggregates or lapilli, depending on their structure. Ash aggregates, or pellets, are formed when individual ash grains stick together and typically have no structure (Brown et al., 2010). More complex aggregates can include well defined layers of ash that have formed as the aggregate has traveled through different regions of a volcanic flow (Brown et al., 2010). Rose and Durant (2009) estimate that 5-10%, by mass, of ash in a typical volcanic eruption is very fine, with a diameter of less than 1  $\mu\text{m}$ . Larger ash, between 10  $\mu\text{m}$  and 1mm, with residence times on the order of days (Niemeier et al., 2009) to hours, can comprise between 50-90% of the total ash content by mass, depending on the eruption conditions.

Volcanic ash is the product of the fragmentation of magma in a volcanic conduit prior to eruption (Yamamoto et al., 2008). As a column of magma begins to depressurize, volatiles exsolve, which lowers the average density of the magma and causes further decompression as the mixture accelerates towards the surface (Yamamoto et al., 2008). Fragmentation is defined as the transition from a continuous melt with a dispersed gas phase to disconnected fragments of glassy, quenched melt. The energy of the system at

fragmentation directly effects the distribution of ash sizes and more energetic eruptions produce more fine ash than less energetic ones (Zimanowski et al., 2003). Eruptions with more volatiles produce more energetic eruptions so volatile rich eruptions are more energetic and, consequently, produce a larger amount of fine ash than would otherwise be expected (Mather and Harrison, 2006).

Delmelle et al. (2005) and Lathem et al. (2011) both studied a range of ash chemical compositions and found that chemical composition has a minimal effect on water adsorption at the ash surface. The samples tested in both studies were found to be hygroscopic, or efficient at water uptake on the ash surface via adsorption. The ash samples were found to be relatively non-porous for diameters on the order of 100  $\mu\text{m}$  or smaller and surface chemistry did not seem to differ significantly across a range of eruptive conditions (Delmelle et al., 2005). Based on ash surface properties, Delmelle et al. (2005) predicts that ash should be able to accumulate a monolayer of water on the particle surface under subsaturated conditions.

Individual ash grains can combine to form aggregates. Gilbert and Lane (1994) detail a number of different aggregate possibilities but the two broadest categorizations for aggregates are dry and wet. Dry aggregates are agglomerations of ash bound by particle charging (Gilbert and Lane, 1994; James et al., 2002). Particle charging can occur from triboelectric charging, which occurs when particles come into contact in the flow, or fractoemission, which occurs in the conduit during fragmentation (Gilbert et al., 1991; James et al., 2002, 2003; Marshall et al., 2005). Charge to mass ratios for volcanic ash have been estimated experimentally to be between  $10^{-5}$  C/kg (Gilbert et al., 1991) and  $10^{-3}$  C/kg (James et al., 2003). In this charge range, electrostatic attraction can lead to the

aggregation of smaller ash particles that would otherwise have been diverted around a larger forming aggregate by laminar flow (Gilbert and Lane, 1994).

Wet aggregation is driven by the presence of water in a volcanic flow (Gilbert and Lane, 1994) and these aggregates are more likely to remain cohesive after being scavenged from the plume (James et al., 2003). Wet aggregates can form when liquid coated particles collide and stick together or when dry aggregates are scavenged by a water droplet (Gilbert and Lane, 1994). Gilbert and Lane (1994) examined water droplet scavenging and ash adhesion to a fixed polystyrene sphere. They found that aggregation efficiency, the number of aggregating particles as a fraction of the total number of particle collisions, increased with decreasing particle size and, consequently, with decreasing collision kinetic energy (CKE). The introduction of salts and other hygroscopic compounds to the experiment promoted aggregate formation, increased the strength of the aggregates and, in particular, increased aggregation rates under subsaturated conditions (Gilbert and Lane, 1994).

A number of experiments have examined pan aggregation of volcanic ash (Schumacher and Schmincke, 1995; Van Eaton et al., 2012). Pan aggregation refers to an experimental setup where an ash sample is dispersed in a circular metal pan and water is added by a sprayer above the pan (Schumacher and Schmincke, 1995; Van Eaton et al., 2012). The pan is shaken, either manually (Schumacher and Schmincke, 1995) or with a sieve shaker (Van Eaton et al., 2012), to simulate collisions between ash particles. Both studies found that ash aggregates began to form between 10-15 wt% of water. Aggregates increased in strength with the addition of water until roughly 30 wt% was reached, at which point the mixture turned into a slurry or muddy flow (Schumacher and Schmincke,

1995; Van Eaton et al., 2012). These experiments are useful to estimate how much water is required to form complex, large scale ( $>300\ \mu\text{m}$ ) aggregates but cannot fully describe how ash may behave in more dilute flows. Rose and Durant (2011) note that fine ash ( $<30\ \mu\text{m}$ ) should be able to remain in the atmosphere for days or weeks but is typically removed from the atmosphere within one day. Aggregation processes have been shown to be effective at collecting particles and removing them from the atmosphere in a number of experimental studies but the mechanisms and removal rates for ash in the atmosphere are still not well constrained (Rose and Durant, 2011).

Models using aggregation parameterizations show that plumes are sensitive to the formulation of aggregation warranting further study of this phenomenon (Folch et al., 2010; Textor et al., 2006b). Veitch and Woods (2001) used a numerical simulation to test the effect of aggregation on ash fallout from the 1980 Mt. St. Helens, WA eruption. When applied to the 1980 Mt. St. Helens eruption, the model predicted a bimodal ash distribution qualitatively similar to observational studies (Carey and Sigurdsson, 1982). However, the peak ash fallout location predicted in the model differed quantitatively from observations suggesting the need for an improved understanding of these processes. Textor et al. (2006a, 2006b) used the numerical plume model, ATHAM, to test the sensitivity of eruption dynamics to particle aggregation. The microphysical parameterization showed that the maximum aggregation efficiency of ash occurred in dense ash flows and in regions where liquid water was present. The amount of aerosol injected into the stratosphere was reduced substantially when aggregation processes were included in the model, reducing the transport distance of ash significantly.

Costa et al. (2010) propose a model that ignores dry aggregation but treats wet aggregation as a function of Stokes number, where aggregation efficiency decreases with increasing Stokes number. Folch et al. (2010) incorporated this model into the FALL3D volcanic simulation. The model was able to reproduce the secondary thickening seen at Mount St. Helens, WA and Crater Peak, AK. Folch et al. (2010) also concluded that both water from the plume and atmospheric water vapor, which has often been ignored (Folch, 2012), are important in the formation of wet aggregates.

Aggregation processes are widely known to alter volcanic plume dispersal patterns. More recently, the 2010 eruption of Eyjafallajökull, Iceland, demonstrated the importance of these processes (Stevenson et al., 2012; Taddeucci et al., 2011). The eruption produced an abundance of both fine ash, increasing concerns for long distance transport and widening the region concerned with the health impacts of the eruption, and coarse ash (Gislason et al., 2011; Ilyinskaya et al., 2011). However, aggregation processes, which were particularly active due to the wet nature of the eruption and local meteorological conditions, removed much of the fine ash close to the source, dampening the regional hazards (Taddeucci et al., 2011). Consequently, improving our understanding of aggregation processes and rates was identified as a key factor to improve hazard assessments for future eruptions (Folch et al., 2009, 2011; Taddeucci et al., 2011).

Volcanic flows pose a large hazard to neighboring communities and wider regional areas. Ash aggregation can significantly alter the life and behavior of an eruptive column or pyroclastic density current. However, aggregation behavior is still relatively poorly understood and more research is necessary to improve predictions of where and how efficiently it will occur. This work examines wet and dry aggregation processes

experimentally to determine what conditions each process dominates under. Relationships will be proposed to define how efficiently ash aggregates in each regime with respect to CKE, relative humidity, pressure and residence time. Finally, these relationships will be used to examine the historic eruption of Kilauea Volcano in 1790.

## **CHAPTER 2**

# **ASH AGGREGATION EFFICIENCY: THE EFFECT OF COLLISIONAL ENERGY**

### **2.1 Introduction**

Explosive volcanic plumes can reach the stratosphere and are capable of moving volcanic ash hundreds of kilometers away from its source, creating a widespread hazard (Prata and Tupper, 2009; Robock, 2000; Niemeier et al., 2009). The horizontal distribution of the plume depends on the rate of ash fallout and the wind field in the ambient atmosphere (Textor et al., 2006a; Barsotti and Neri, 2008; Schumacher and Schmincke, 1995). As the plume evolves, collisions between ash particles can produce aggregates (Gilbert and Lane, 1994; Schumacher and Schmincke, 1995). Aggregation, the adhesion of ash, can significantly reduce the transport distances of ash and can modify the dynamics of the plume (Veitch and Woods, 2001; Textor et al., 2006b). Aggregation is not confined to volcanic plumes; it also occurs in several other domains of explosive volcanism, including near-vent volcanic columns and pyroclastic density currents (Brown et al., 2010). Marzano et al. (2010) modeled ash fall from the November 2004 eruption of Grímsvötn, Iceland, and noted that the lack of information concerning aggregation mechanisms and efficiency is among the largest sources of uncertainty in tracking the ash plume. In order to improve our understanding of particle-laden eruptive flows and the hazard models used to predict the aftermath of volcanic eruptions, it is necessary to improve our understanding of the processes driving ash aggregation (Scollo et al., 2008; Veitch and Woods, 2001; Costa et al., 2010).

Ash aggregates have been broadly defined as any conglomerate of ash particles (Gilbert and Lane, 1994). Aggregates can be formed through turbulent mixing or gravity-driven differential acceleration, with or without the presence of moisture (Schumacher and Schmincke, 1995; Gilbert and Lane, 1994). Electrostatic aggregation of solid particles and droplet coalescence of fluid drops act as end-member proxies in the study of particle aggregation. Dry charged particles can aggregate through electrostatic attraction. This process does not necessarily require two particles to collide but only to pass within a small distance of one another; typically less than three particle diameters based on the charge density predicted for 100  $\mu\text{m}$  particles (Gilbert and Lane, 1994). At the other end of the spectrum, droplet coalescence assumes that both colliding particles are fully wetted and the initially interacting surface is that of water, not the solid particles. This fully saturated behavior may be found at plume margins, where gasses have expanded and cooled, or in pyroclastic density currents, which have cooled through the entrainment of ambient air to reach saturation. Regardless of how an aggregate is formed, ash aggregates, being larger and heavier than individual pieces of ash, return to the surface more quickly than individual ash grains, diluting and decreasing the transport distance of a plume (Brazier et al., 1982; Veitch and Woods, 2001).

Aggregation efficiency is defined as the fraction of colliding particles that stick together, typically for timescales longer than one second (Brown et al., 2010). With this information and an estimate of collision rate the aggregation rate for a parcel of the volcanic region can be assigned. Typically only a small fraction of the colliding particles will also successfully aggregate. Aggregation efficiency, when applied to colliding water

droplets, is termed coalescence efficiency because the droplets are becoming a single, larger, droplet (Beard et al., 2002).

Experimental studies on droplet coalescence and particle-droplet collisions provide a framework for discussing particle-particle aggregation. Coalescence efficiency depends on numerous factors including droplet sizes, mass, velocity and collision kinetic energy as summarized in Table 2.1 (Beard et al., 1979; Beard et al., 2002; Brazier-Smith et al., 1972; Low and List, 1982).

Table 2.1. Summary of previous coalescence efficiency studies.

| <b>Study</b>               | <b>Droplet Size (µm)</b> | <b>Material</b> | <b>Coalescence Efficiency</b> |
|----------------------------|--------------------------|-----------------|-------------------------------|
| Beard et al., 1979         | 81,20- pairs             | water           | 0.370                         |
| Beard et al., 2002         | 55-105                   | water           | 0.950                         |
| Brazier-Smith et al., 1972 | 150-750                  | water           | 0.100 – 0.600                 |
| Low and List, 1982         | > 200                    | water           | 0.500                         |

All four of the studies in Table 2.1 agree that droplet energies at the onset of a collision event are an important factor in determining whether or not coalescence will occur. However, only Low and List (1982) calculates the energy of collision for coalescing water droplets. The collision kinetic energy (CKE), a widely used characterization of the collisional energy of two particles, of the 200 µm drops is, at most,  $5 \times 10^{-7}$  J. CKE is calculated using the reduced radius and approach velocity of the colliding particles. Beard et al. (2001) conducted studies of droplet–droplet collisions and found that coalescence tends to happen more frequently at lower particle energies whereas, at higher energies, droplets are more likely to fully rebound or to coalesce briefly and then break up.

The aggregation of wet particles is physically different from droplet coalescence, especially in the case of porous and irregularly shaped ash which can accumulate water without developing a full surface coating, and experiments, beyond those conducted on droplet pairs, need to be conducted to better model their behavior. Volcanic flows contain large amounts of salts, particularly chloride and sulfide salts, which allow volcanic aerosols to condense before super-saturation is reached (Gilbert and Lane, 1994). However, recently Lathem et al. (2011) tested the hygroscopicity of seven ash samples and found six of them to correspond more closely to pure  $\text{SiO}_2$  than to sulfate salts. The exact role that salt deposition plays in ash hygroscopicity is still not well known. Though less hygroscopic than salts, Lathem et al. (2011) showed that ash is hygroscopic and highly reactive at its surface, making it a strong candidate for water adsorption. However, none of these studies provide a direct relationship between surface processes and aggregation efficiency.

Volcanic hazard models to date have either neglected to consider ash aggregation or used a generalized proxy, often based on droplet coalescence research (Textor et al., 2006a; Barsotti et al., 2008), which does not accurately reflect the microphysics of ash aggregation and is often inaccurate (Telling and Dufek, 2012). However, the unique composition and origin of ash, as well as the setting in which it is found, motivate the modeling of ash as a unique species. Our research explores the relationship between aggregation, sub-saturated water vapor and collisional energy specifically for volcanic ash in an experimental setting. Experiments were designed to collect data on thousands of particle collisions and their outcomes in order to produce a measure of aggregation efficiency that can be implemented into large-scale numerical models. The experiments

presented here provide new probabilistic relationships for ash aggregation at varying particle collisional energy.

## **2.2 Methods**

Lab experiments were designed to test the relationship between atmospheric humidity, collisional energy and the efficiency of ash aggregation. An enclosed tank, in which relative humidity could be adjusted and monitored, was built to house the experiments. Experimental samples were accelerated into the tank through a vertical nozzle and particle positions (and velocities) were determined with a Phantom MIRO-4 high-speed camera. Data analysis was completed using a particle image velocimetry method, which has been modified for the analysis of inertial and collisional particles.

### **2.2.1 Experimental Setup**

The tank was constructed out of 6.4 mm thick plexiglass and is 0.61 m × 0.15 m × 0.61 m. The particle jet assembly was constructed to inject ash samples upwards into the contained tank using a pressurized gas line connected to the bottom of the assembly. A plastic planar nozzle was affixed to the top to control the direction of particle flow out of the assembly and to increase the number of collisions in the plane probed by laser illumination. A stainless steel wire mesh, number 325, was inserted into the lower piece of copper piping, forming a stage that allowed pressurized air to move upwards, accelerating the sample loaded onto the top of the mesh, but was fine enough to not allow the sample to fall downwards into the gas line. A humidifier, with a variable output control, was connected to the tank via a sealed connection, allowing for careful regulation of the humidity in the tank. An Omega OM-73 temperature and humidity gauge was attached to the inside wall of the tank so that conditions could be monitored and recorded

during trials. The temperature and humidity in the tank were measured immediately before each trial and checked at the end of every trial to verify that neither had changed during the duration of the experiment.

An Nd:YAG laser, wavelength 532 nm, output 20 mW, was situated above the tank oriented parallel to the nozzle opening at the top of the particle jet assembly. The light illuminated the  $\sim 100 \mu\text{m}$  size ash so that discrete particles could be resolved during the lab trials. The beam was approximately  $200 \mu\text{m}$  wide, approximately twice the width of two particles placed side to side.

A Phantom MIRO 4 high speed camera was arranged in front of the tank to capture the motion of the particles. The lens was focused on the plane of the laser light aligned with the top of the jet nozzle. The average field of view was  $0.045\text{m} \times 0.044\text{m}$ , with a pixel resolution of  $256 \times 256$  pixels, and trials were conducted at speeds ranging from 1800 to 3000 frames per second. This corresponds to a spatial resolution of approximately  $176 \times 172 \mu\text{m}$ . The bottom of the field of view was oriented  $0.4 \text{ m}$  above the top of the particle jet in order to allow the sample to slow down and disperse. The camera recording was triggered directly prior to the triggering of the gas line into the tank so that the full motion of the particles could be captured as they moved through the field of view. Figure 2.1 illustrates the full experimental setup.

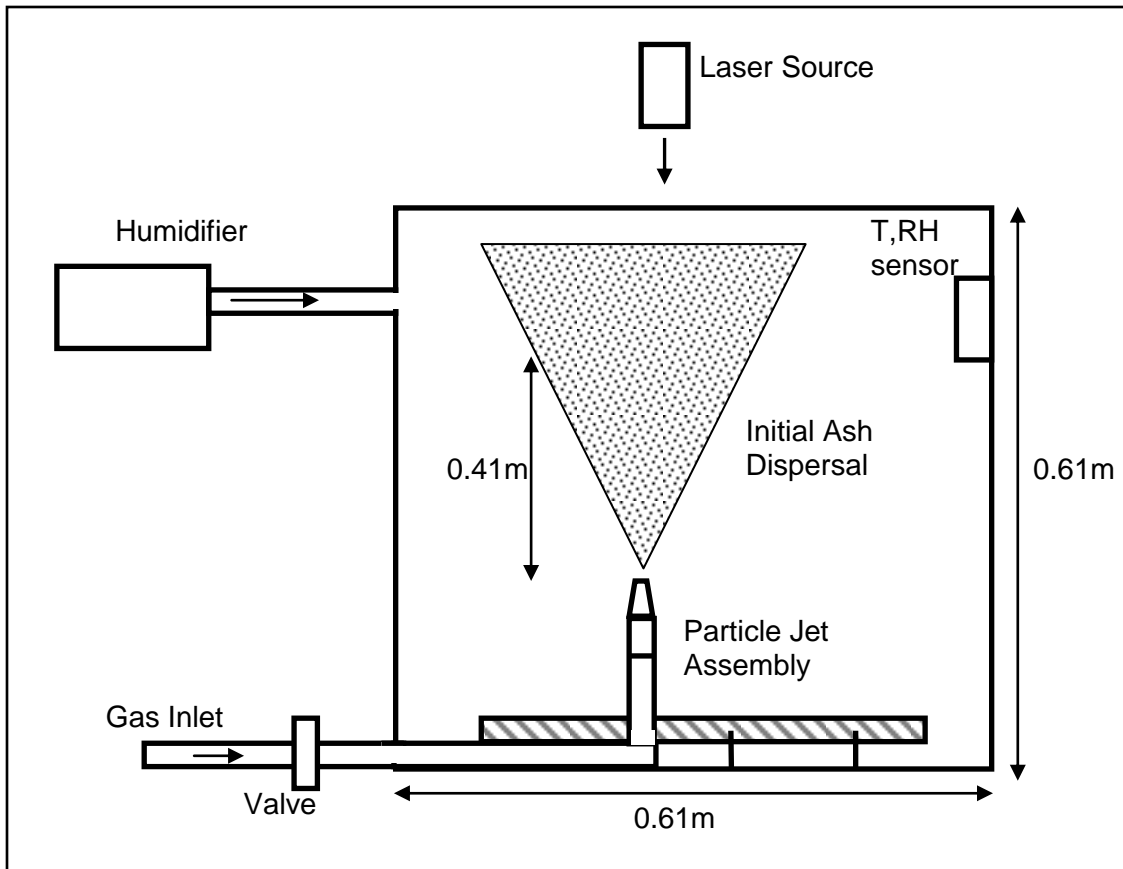


Figure 2.1. Diagram of the full tank setup. The camera position is not shown on this 2D rendering but would be situated directly in front of the particle jet assembly, 0.41m above the top of the nozzle. Not to scale.

### 2.2.2 Data Collection

Two different particle samples were used in the trials. The first sample was mono-disperse spherical silica with a diameter between 90 – 150  $\mu\text{m}$ . The second sample was an ash sample collected in the field from Tungurahua, Ecuador in 2006. Ash grains in the second sample were primarily glass fragments with some fragmented crystals. The sample was sieved to three size ranges: 106 – 125  $\mu\text{m}$ , 125 – 212  $\mu\text{m}$  and 212 – 250  $\mu\text{m}$ . The ash sample was dried on a hot plate prior to being used in the experiment to ensure that water on the sample was a product of the humidity in the tank alone.

Once a sample was loaded into the particle jet assembly and the assembly was mounted onto the stage, the tank was closed. Low humidity cases relied on the ambient relative humidity at the time of the experiment, typically 20-30%. Higher humidity trials were run by sealing the tank and running the humidifier until the desired humidity was reached. The humidifier was then used to maintain the humidity in the tank within +/- 0.5% from the value recorded at the beginning of each trial. The temperature, relative humidity and camera recording parameters were recorded for each trial. Each trial lasted between 30-60 seconds. Once completed, the digital files from each trial were reviewed and extracted into individual frames for analysis.

### **2.2.3 Post Processing**

The images were first analyzed using an adapted form of particle image velocimetry technique (PIV), a commonly used technique in analyzing fluid flows (Santiago et al., 1998; Prasad, 2000; Aanen, 2002). The algorithm was developed in Matlab specifically for use in these experiments because standard PIV assumes that particles follow the fluid flow field and do not interact with each other, which is not appropriate for these experiments. The algorithm tagged all of the particles in a series of images discreetly and tracked their movement by assuming that the particle in a successive image (n+1) would be closest to itself in the previous image (n). This assumption was checked by predicting each particle position out to one additional time step (n+2) and then determining whether a particle was physically present at the expected location within a tolerance factor (Figure 2.2). The center coordinates for each particle were determined by averaging the left and right and upper and lower bounds of each particle, for the x and y positions respectively. Matlab image analysis tools also

interpolated the particle boundaries based on pixel brightness. Due to this interpolation particle positions and sizes are recorded in terms of partial or fractional pixels. This modified PIV algorithm was used to tag and track particles that remained in the field of view over the course of four or more high-speed video frames in order to measure the energy and result of individual particle collisions. This algorithm can only measure motion and collisions occurring in the nearly 2D plane of the laser illumination. As we are only concerned with measuring the aggregation probability from numerous collisions it is not necessary to detect every collision in the 3D flow field.

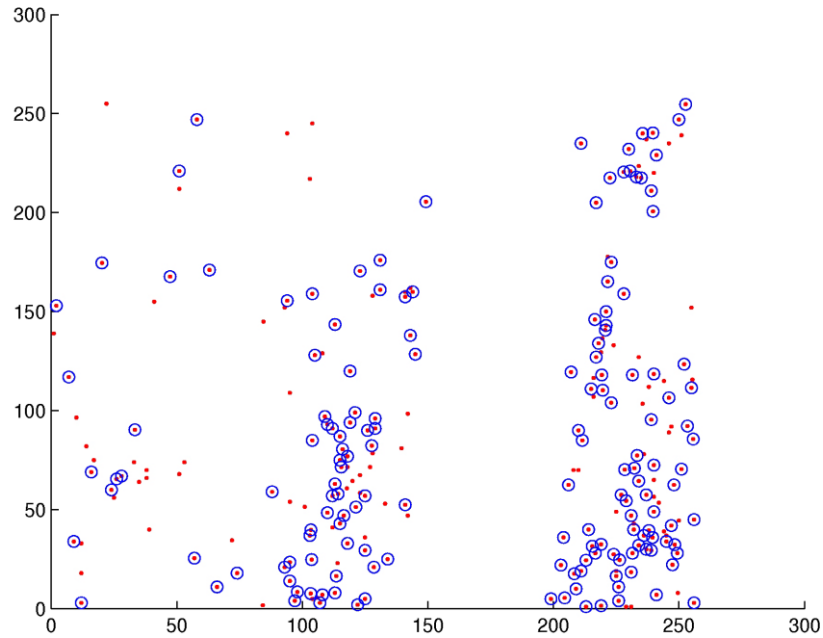


Figure 2.2. A computer rendering of the particle distribution in one frame of a trial with  $\text{SiO}_2$  particles. The identified particles in the current frame are shown as red dots and the particle positions predicted from the previous frame (Eq. 1 and 2) are drawn with open blue circles. This procedure removes particles that are not moving in the plane of the laser.

Particle collisions and aggregation were analyzed based on the initial flow field data. Collisions were predicted using the velocity vectors found through PIV. Particles

that were collocated in space and time were found by predicting particle locations one time step after particle velocity was determined (Eq. 2.1).

$$x_i^{n+1} = x_i^n + (u_i^n \cdot dt) \quad \text{Eq. 2.1}$$

where  $x$  denoted the physical coordinate of the particle in the  $i$  dimension,  $u$  is the particle velocity and  $dt$  is the lapse time between images. The superscripts refer to the time step in a four image series. All mathematical notation used, along with the appropriate units, are listed in Nomenclature. In this formulation we neglect drag over the time step,  $dt$ . The impact of drag on the particles is accounted for in the tolerance used to verify particle positions after aggregation and is discussed in more detail below. While particles were being tracked by the location of their center, each particle did have a physical size so particles did not have to be perfectly collocated in either space or time for a collision to occur. Beard et al. (2001) employed a method to solve for the period of time,  $t_i$ , in which two particles would interact (Eq. 2.2). The difference between the interaction time in the  $x$  and  $y$  directions had to be less than the time step between images (Eq. 2.3).

$$t_{i_x} = \frac{s \cdot (r_1 + r_2)}{u_1 - u_2} \quad \text{and} \quad t_{i_y} = \frac{s \cdot (r_1 + r_2)}{v_1 - v_2} \quad \text{Eq. 2.2}$$

$$t_i = |t_{i_x} - t_{i_y}| < dt \quad \text{Eq. 2.3}$$

where  $r_1$  and  $r_2$  are the two particle radii,  $u_i$  describes the velocity in the  $i$  dimension and the subscripts (1 and 2) denote which particle the velocity is attributed to. The factor of  $s$  in the numerator is a dimensionless tolerance on particle proximity. Beard et al. (2001) set  $s$  equal to 2. In this analysis a tighter tolerance was used and  $s$  was set equal to 1 to counteract the effect of light scattering around particles and the disparity in particle and

pixel sizes. With this formalism, particles that have a time threshold,  $t_i$ , that is less than  $dt$  will collide. Light scattering could make particles appear larger than they actually were. Additionally,  $\text{SiO}_2$  particles and, to a lesser extent, some ash particles had diameters that were smaller than the physical width of a pixel, further increasing their apparent computed size. We calculated that together these effects can increase the apparent particle size by two to three times the actual particle size (Figure 2.3).

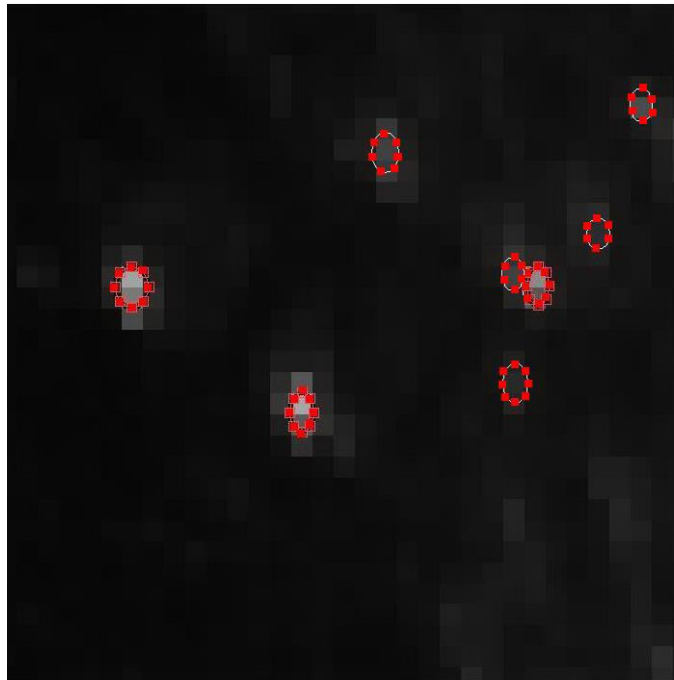


Figure 2.3. A raw image zoomed in to show a region  $0.0042 \times 0.0042 \text{m}$  from a  $\text{SiO}_2$  trial. Several particles have been overlaid with their actual particle size, roughly  $100 \mu\text{m}$  in diameter. The light gray pixels directly around the highlighted particles are the effect of light scattering.

One hundred separate identified events were hand checked for anomalous collision identifications. The time threshold value of Equation 2.3 was varied, but always less than the time between frames, during the analysis to verify that the number of detected collisions decreased as the time constraint was tightened. Less than 8% of the events tested were anomalous once this value was reduced to  $1/10,000$ . Further reduction

of the time threshold did not improve accuracy. This adjusted PIV algorithm, which solved for the 2D particle equation of motion (including drag and gravitational forces), was also tested on a set of computer-generated images of particles moving through space over a series of time steps. Particles in the images interacted with one another, bouncing or aggregating, similar to the behavior expected from physical particles. Less than 5% of the identified events from the computer generated images were false. Once a collision was detected, the involved particles were analyzed in the aggregation algorithm. Data concerning the particle sizes, velocity vectors and the result of the interaction were saved to an output file for every collision event.

To determine whether a collision resulted in an aggregation event, a simplified momentum equation (Eq. 2.4) for the colliding particles was solved to predict the final velocity of a possible aggregate,

$$u_i^{n+3} = \frac{(m_1 \cdot u_{i_1}^{n+2}) + (m_2 \cdot u_{i_2}^{n+2})}{m_1 + m_2} . \quad \text{Eq. 2.4}$$

In this equation,  $m_1$  and  $m_2$  are the masses of the two particles. The final position of the aggregate was predicted, based on these velocities, for the frame following the collision event. As the momentum equation is not exact and there was some variation in the mass of the ash particles a region around the projected position was examined. A maximum value of +/- 2 pixels, in the x and y directions, was determined for the aggregation tolerance to account for the effect of gravity and drag on particle location (Raju and Meiburg, 1995; Burgisser et al., 2005). Conservatively, the algorithm required that the predicted particle position must coincide with an actual particle within +/- 1 pixel in both the x and y directions in order for the event to be considered a successful aggregation event. The solutions to over 100 positive aggregation identifications were checked

manually and, of these, only 2-3% of detected events were found to be incorrect solutions. This number did not decrease significantly as the tolerance was further reduced.

Trials, at varying humidity, were run for both the silica (ballotini) and ash samples. Fifty three trials were run using the silica particulate and twenty two trials were run with the ash samples from Tungurahua, for a total of seventy five trials. The ballotini sample was primarily composed of SiO<sub>2</sub> (Potters Industries Inc.) The major oxide composition for the Tungurahua ash samples is from the same eruptive unit sampled by Samaniego et al. (2011). The physical parameters for these trials have been reported in Appendix A.

A bulk output file summarizes the run once it was complete, complementing the individual data recorded for each collision event. The file included the total number of particles in the run, the number of collision and aggregation events and the frequency of collisions (per second) averaged over the run. This bulk data, as well as the event specific data on collision and aggregation events, was used for data analysis.

### **2.3 Results**

The effective particle size distribution for the ash and SiO<sub>2</sub> samples that was measured during image analysis has been reported in Figure 2.4. The distribution includes both aggregate and individual particles and records all frames analyzed and includes  $4.2 \times 10^5$  SiO<sub>2</sub> particles and  $1.8 \times 10^5$  ash particles. The physical size of an individual SiO<sub>2</sub> particle ranged from 90-150  $\mu\text{m}$ . A few factors may impact the slight increase in particle size between the known distribution of sizes and the sizes measured in post-processing. Light scattering around the particles can increase the imaged size of

particles, likely by no more than a factor of 1.5 to 2. Particles also might be captured by more than one pixel, enhancing their size in the high-speed images. The ash sample had a wider initial size distribution, ranging from 100 – 250  $\mu\text{m}$ , though more trials were run with the larger ash size samples. Light scattering is less prominent for the ash sample because it is dark in color and scatters light less effectively than the white  $\text{SiO}_2$  sample. Ash particles may overlap adjacent pixels, increasing their recorded size. No more than 35% of a particle sample, with a size distribution between 90 – 150  $\mu\text{m}$ , was artificially enlarged enough to fall outside of its anticipated size range. Affected particles were enlarged by two to three times their actual size. Particle diameters were used to estimate mass and momentum of particles but particle size alone was not used to estimate the efficiency of particle aggregation because it is not necessarily possible to tell if a particle has aggregated or is scattering light based on its size alone.

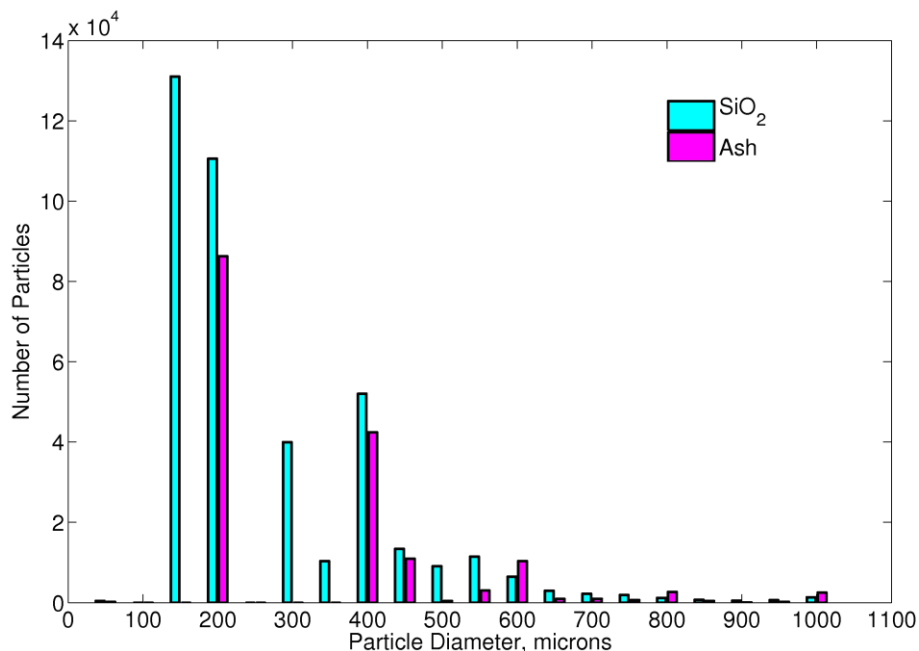


Figure 2.4. Particle size distribution for ash and SiO<sub>2</sub> samples. Effective particle diameters were measured along the longest axis of each particle for every particle identified and counted in 50 μm wide bins. Particle diameters were not altered to adjust for light scattering since the effect is not uniform across all particles. Light scattering around SiO<sub>2</sub> particles could increase the apparent particle diameter by approximately a factor of two times its actual size, though light scattering was not observed around every SiO<sub>2</sub> particle. Light scattering was less effective around ash particles due to the darker color of the volcanic ash and increased the size of these particles by a factor of less than two.

Aggregation efficiency was determined in the same way that coalescence efficiency is determined for water droplets (Glickman, 2000), as a function of the number of collisions in a given series of images, and reported as a percentage. The bulk data was averaged over ranges of 5% relative humidity. The reported error is the standard deviation for the averaged results in each bin (Figure 2.5). The total number of bounce and aggregations events in each bin has been reported next to the corresponding data point. Due to the darker color of ash particulate and the blurring effect that was sometimes observed in very high humidity, RH > 70%, SiO<sub>2</sub> trials; no ash trials were

conducted at relative humidity greater than 65%. The data exhibits little to no trend for increased aggregation with increasing relative humidity in this humidity range.

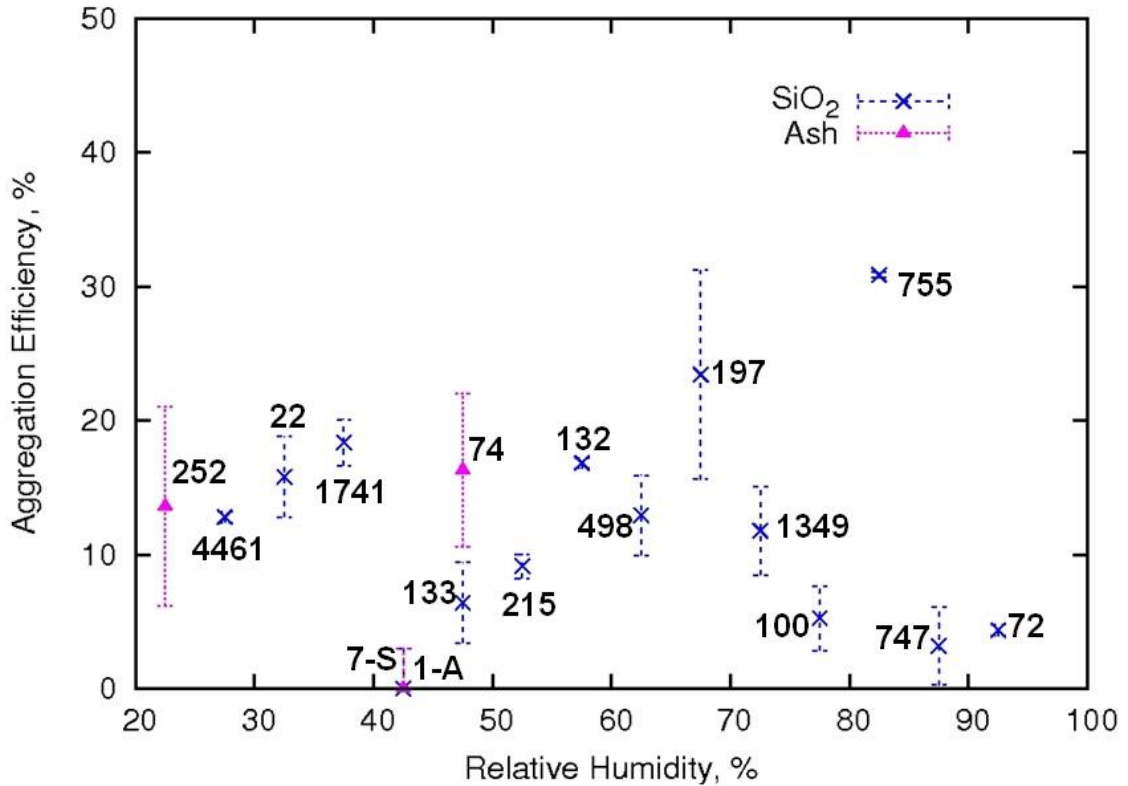


Figure 2.5. Aggregation efficiency as a function of relative humidity. Bins with a width of 5% relative humidity were used to average the data and calculate error. The number of bounce and aggregation events for each bin was recorded and used to produce the aggregation efficiency for that bin and the reported error is the standard deviation for each set of data points. The bin for which standard deviation could not be calculated, due to dearth of data, has a 3% error attached to it, the maximum error on the number of aggregation events calculated by hand checking bounce and aggregation solutions from the PIV algorithm. The number of data points in each bin is reported next to the bin average. Little to no correlation between relative humidity and aggregation efficiency was observed.

Aggregation efficiency was also calculated for a range of CKE values (Figure 2.6). The technique of averaging data points within a bin was used again to handle the large quantity of data collected over fifty seven trials. CKE bins were created to maximize the number of data points per bin, minimizing the error. Each bin has a

minimum of 200 SiO<sub>2</sub> events or 50 ash events, respectively. The maximum CKE of a SiO<sub>2</sub> bounce event was 8.52 x 10<sup>-4</sup> mJ and the maximum CKE of aggregation was 3.64 x 10<sup>-4</sup> mJ. The difference between the maximum CKE of ash bounce, 2.80 x 10<sup>-4</sup> mJ, and ash aggregation, 3.60 x 10<sup>-6</sup> mJ, was much larger than that recorded for SiO<sub>2</sub>.

The least squares method was used to fit the SiO<sub>2</sub> and ash data series (Eq. 2.5 and 2.6) and the maximum asymptotic standard error was 22%. Increasing CKE leads to a decrease in aggregation efficiency. Aggregation efficiency becomes very low above a threshold CKE value.

$$\varepsilon_{SiO_2} = (-16.02 \cdot \ln(E)) - 222.73 \text{ for CKE} \leq 9.0 \times 10^{-7} \text{ mJ} \quad \text{Eq. 2.5}$$

$$\varepsilon_{ash} = (-13.57 \cdot \ln(E)) - 194.43 \text{ for CKE} \leq 6.0 \times 10^{-7} \text{ mJ} \quad \text{Eq. 2.6}$$

In this set of equations (Eqs. 5 and 6),  $\varepsilon$  is the aggregation efficiency and E is the CKE of a collision event.

The relationship between CKE and aggregation efficiency was also examined at specific humidity ranges. The aggregation efficiency, as a function of CKE, was determined for the SiO<sub>2</sub> and ash events with relative humidity values between 20-50% and 50-80%. Additionally, the relationship was also determined for SiO<sub>2</sub> particles between 80-100% relative humidity. However, no further correlation between relative humidity, CKE and aggregation efficiency was determined.

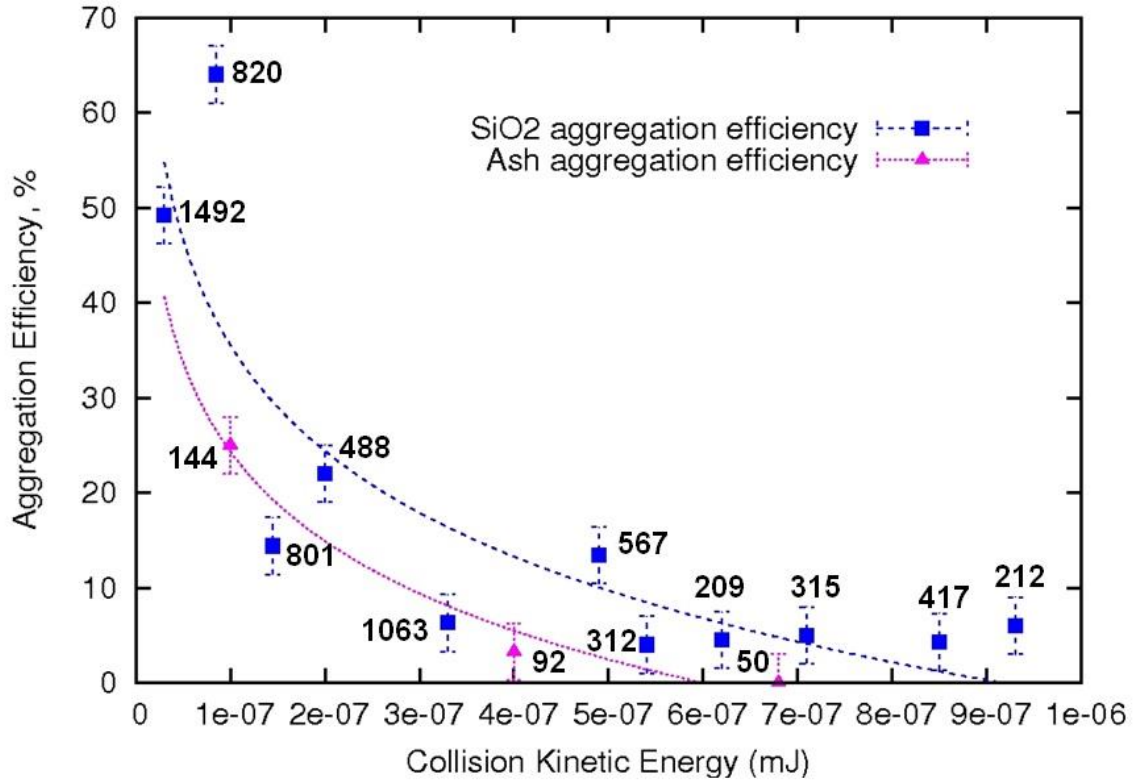


Figure 2.6. Aggregation efficiency as a function of CKE. Data binning along the x-axis was also utilized here however bins were created to maximize the number of events in each bin, reducing error, and are not evenly sized. Bins have at least 200 SiO<sub>2</sub> events or 50 ash events. The trend lines applied to the data describe the relationship between CKE and aggregation efficiency for energies below a threshold,  $6 \times 10^{-7}$  mJ for ash and  $9 \times 10^{-7}$  mJ for SiO<sub>2</sub>. Above these values it can be assumed that the aggregation efficiency is very low but not equal to zero.

## 2.4 Collision and Aggregation Mechanisms

Electrostatic attraction and capillary forces are the two end-member cases driving aggregation events (Schumacher and Schmincke, 1995) but it is probable that both forces work to drive particle aggregation in a volcanic setting. Individual particle charges are typically small though they can affect particle collisions over distances of three particle diameters or less (Gilbert and Lane, 1994). Conversely, capillary forces rely on direct

collisions between wetted particles but are orders of magnitude greater than electrostatic forces when acting to bond particles together (Schumacher and Schmincke, 1995).

#### **2.4.1 Wet Aggregation Processes**

Gilbert and Lane (1994) and Beard et al. (1979, 2002) both conducted laboratory experiments on droplet aggregation. A comparison of the results of these papers to the current work has been provided in Figure 2.7. Gilbert and Lane (1994) use fully wetted SiO<sub>2</sub> and volcanic ash samples and observed a similar trend for increasing aggregation efficiency with decreasing CKE. The CKE values in the Gilbert and Lane (1994) study range from 10<sup>-6</sup> to 10<sup>-5</sup> mJ and correspond to aggregation efficiencies of 5-11%. Compared to the results presented here, Gilbert and Lane (1994) provide an insight into the behavior of fully wetted ash collisions, which are able to produce aggregates at higher energies. The trend seen in the Gilbert and Lane (1994) data shows an asymptotic approach toward zero aggregation efficiency at high CKE that is not seen in the current data, highlighting the difference between the behaviors of ash in sub- and super-saturated flows.

In Figure 2.7 we compare three distinct cases in the study of wet aggregation; droplet-droplet coalescence, particle aggregation in supersaturated flows and particle aggregation in sub-saturated flows, illustrating the importance of treating each regime separately in order to accurately model aggregation in complex multiphase flows. The Beard et al. studies used water droplets to model aggregation. Beard et al. (1979) used 20 and 81 μm drops, while the Beard et al. (2002) study used larger drops, 55 to 105 μm, with a smaller difference in size, ranging up to only 25 μm between the largest and smallest drops.

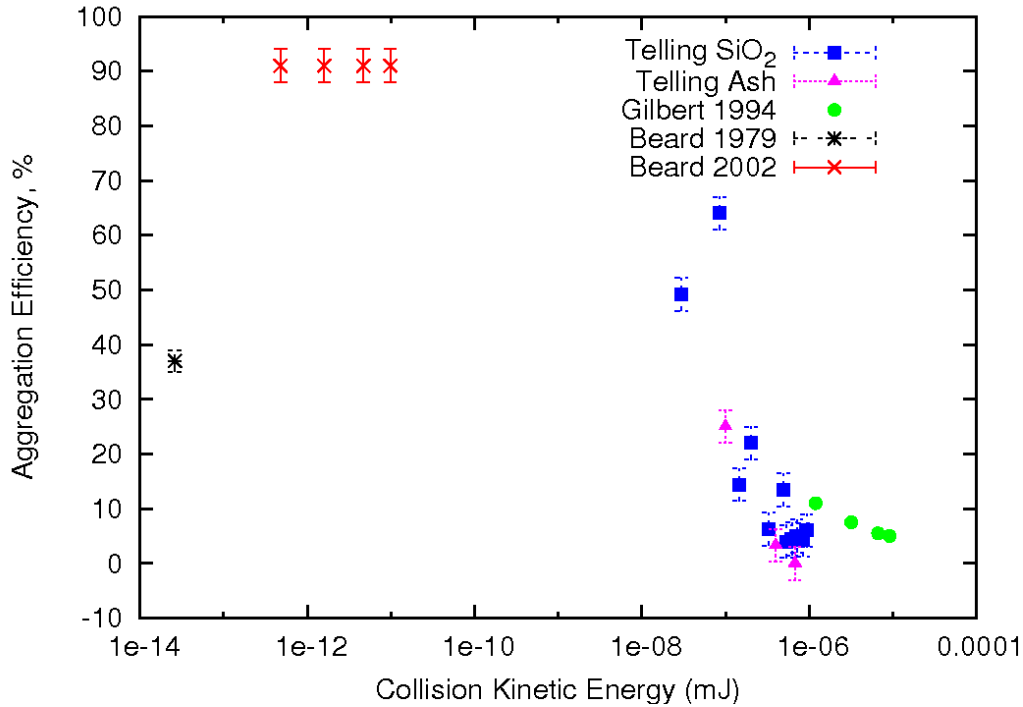


Figure 2.7. A comparison of previous work to the current results. Gilbert and Lane (1994) use SiO<sub>2</sub> traveling through a high humidity chamber while Beard et al. (1979, 2002) use water droplets only. Error data for Gilbert and Lane (1994) was unavailable.

Schmeeckle et al. (2001) considered the outward force that a thin layer of air or water will exert on two colliding particles, although at much larger particle scale than the ash particles considered here. Bounce interactions were most commonly found to be the result of high particle velocities, which produce rebound, but can also result from low particle velocities, which are unable to move particles through the layer of air or water separating them. Montgomery (1971) studied this behavior for the case of gravity driven collision and coalescence, estimating that collisions were most likely to result in full coalescence when droplet velocities did not exceed 50% of the terminal velocity. Orme (1997), however, also suggests that there is a lower bound on the CKE that will produce droplet coalescence. As two droplets move to collide, a layer of air between them must be moved out of the way before coalescence can take place. Low and List (1982) calculated

the CKE typical to coalescence events in their experiments and found it to typically be on the order of  $10^{-8}$  -  $10^{-6}$  J. The CKE of aggregation events in this study was much lower, ranging from  $10^{-11}$  -  $10^{-9}$  J. Particles in a sub-saturated flow, like those in this study, rebound at the higher energies expected to produce coalescence for similarly sized water droplets.

Mikhailov et al. (2009) investigated the hygroscopicity of aerosols and found that water uptake on particles was typically accelerated above 80% relative humidity. Lathem et al. (2011) found that monolayer coverage of ash occurs between 70-80% but that ash activation, the point at which ash is fully coated with liquid and begins to behave like a droplet, is unlikely below 100% saturation. Trials conducted in this study, above 80% relative humidity, did not show a clear increase in aggregation efficiency. Since it is possible for monolayer coverage of ash to develop in this high humidity range, the sample may not have circulated long enough for full coverage to be reached. It is also possible that monolayer coverage of particles is insufficient to drive aggregation.

The surface chemistry of ash particles is permanently altered through interaction with hygroscopic compounds in volcanic flows (Rose, 1977; Delmelle et al., 2007) so the ash used in the experiments already contained hygroscopic compounds on its surface whereas the synthetic  $\text{SiO}_2$  particles did not. However, little difference was seen between the behavior of  $\text{SiO}_2$  and ash when the aggregation efficiencies were plotted against relative humidity (Fig. 2.5). The lack of distinction between particle species and the lack of increased aggregation efficiency at high values of relative humidity both suggest that, in sub-saturated conditions, aggregation is more likely to be driven by electrostatic forcing than condensed water vapor.

## 2.4.2 Dry Aggregation Processes

Mechanisms for particle charging in plumes are incompletely understood. However, Gilbert et al. (1991) proposed two plausible mechanisms- triboelectric charging, charge exchange between particles with different work function, and fracto-emission, charged particles generated during fragmentation, in the plume. James et al. (2002, 2003) have both shown that fragmentation in a laboratory setting is sufficient to produce aggregates that are many times larger than their component particles. Fragmentation of particles is unlikely to occur in the experiments presented here because the initial sample is already micrometer scale particulate. However, triboelectric charging may occur during particle–particle collisions, resulting in charge exchange and particle charging. Gilbert and Lane (1994) compare wet and dry aggregation processes and offer a method for calculating the possible effect of charging on the system.

Assuming triboelectric charging is driving aggregation in these experiments, a minimum particle charge density can be determined by considering the CKE of particle collisions. In order for an electrostatic aggregate to form, the electrostatic force attracting two particles must be stronger than the inertial force of the particles rebounding after a collision event. Equation 2.7 utilizes the CKE to determine the minimum particle charge,  $q_i$ , necessary for two colliding particles to aggregate assuming equal (and opposite) charge density on each particle:

$$q_i = \left( \frac{E \cdot (r_1 + r_2)}{k} \right)^{1/2} \quad \text{Eq. 2.7}$$

where  $k$  is Coulomb's constant.  $E$  is the average CKE of the ash and ballotini aggregation events,  $2.7 \times 10^{-7}$  mJ. This corresponds to an aggregation efficiency of 19.6%,

when calculated using Eqn. 2.5. Using a radius of  $100\mu\text{m}$ , and density,  $\rho = 2700 \text{ kgm}^{-3}$ , we can calculate the average charge density on the particulate. The average charge density necessary for particle aggregation was found to be  $3.8 \times 10^{-5} \text{ Cm}^{-2}$ , or  $2.2 \times 10^{-4} \text{ Ckg}^{-1}$ . The first value is the charge per surface area assuming a sphere, and the second value is the mass charge density. These values are on the same order of magnitude as those reported by Gilbert et al. (1991) and Gilbert and Lane (1994). James et al. (2003) found that the maximum charge produced by fracto-emission in a laboratory setting was on the order of  $10^{-3} \text{ Ckg}^{-1}$ , slightly higher than the charges produced by triboelectric charging in the current research and the work of Gilbert et al. (1991) and Gilbert and Lane (1994). Additional experiments will be necessary to more fully understand the role and magnitude of particle charging in these experiments but, in a sub-saturated regime, electrostatic forcing is the most likely mechanism for particle aggregation.

## 2.5 Conclusions

Aggregation is a dynamically important process in volcanic columns and we have conducted experiments to constrain the aggregation efficiency for ash particles. The behavior of hundreds of thousands of particles, resulting in over 10,000 recordable particle interactions, was analyzed under varying relative humidity conditions to improve our understanding of particle aggregation driving mechanisms. When collision kinetic energy (CKE) and relative humidity are considered separately, CKE provides a much more distinct picture of aggregation behavior in subsaturated conditions. Aggregation efficiency drops rapidly as the CKE of a specific event increases. Relative humidity was shown to have little influence on aggregation efficiency below saturation over the time scales studied here. Consequently, electrostatic forces were found to be the driving

mechanism for particle aggregation. Using information about the energy of particle collisions, a minimum charge density on aggregates was determined in order for the particles to stick together after colliding.

Previously, many volcanic plume models have relied on the aggregation characteristics of water droplets to model ash aggregation. A comparison of the droplet coalescence studies in Table 2.1 and the results of Gilbert and Lane (1994), Costa et al. (2010) and the current research shows that water is a poor proxy for the behavior of ash in under-saturated conditions. Aggregation efficiency is significantly reduced in studies of ash or ash proxies and shows a strong correlation with CKE. Further study of particle charging and activation are needed to better understand and model aggregation processes.

# CHAPTER 3

## ASH AGGREGATION EFFICIENCY: THE ROLE OF THE ATMOSPHERE

### 3.1 Introduction

The residence time of volcanic ash emitted into the atmosphere during explosive volcanic eruptions ultimately determines the extent and duration of airborne-ash hazards [e.g. *Ilyinskaya et al.*, 2011; *Folch et al.*, 2010; *Taddeucci et al.*, 2011]. One of the largest sources for uncertainty in determining ash residence time is our limited understanding of the mechanisms and rates of ash aggregation, the process by which ash particles adhere to each other in the atmosphere. While aggregation rates remain poorly understood, their presence is documented in many recent eruptions and they are prominent in the depositional record [*Brand and White*, 2007; *Branney and Brown*, 2011; *Brown et al.*, 2010; *Scollo et al.*, 2007; *Stevenson et al.*, 2012; *Veitch and Woods*, 2001]. Recent volcanic eruptions, including the eruption of Eyjafjallajökull in 2010, highlighted current gaps in our understanding and quantification of the aggregation mechanisms [*Folch et al.*, 2009; *Taddeucci et al.*, 2011; *Folch*, 2012]. Integrating new information on ash aggregation mechanisms into numerical models has been suggested as a critical factor needed to improve their accuracy [*Scott and McGimsey*, 1994; *Veitch and Woods*, 2001; *Scollo et al.*, 2007; *Folch et al.*, 2010; *Textor et al.*, 2006b].

Few experiments have been designed to study ash aggregation directly and, until recently [*Van Eaton et al.*, 2012], it has either not been considered in models or water droplet coalescence has been used as a proxy for this behavior [*Gilbert and Lane*, 1994; *James et al.*, 2002, 2003; *Barsotti et al.*, 2008]. Models assuming liquid coated ash cite

the need for constraints on the efficiency of the process [*Textor et al.*, 2006a; *Costa et al.*, 2010]. In the limited parameter space that has been tested experimentally, droplet coalescence has been found to be an inaccurate proxy [*Gilbert and Lane*, 1994; *Telling and Dufek*, 2012]. Decreasing collision kinetic energy (CKE) has been found to increase efficiency of both aggregation [*Gilbert and Lane*, 1994; *Telling and Dufek*, 2012] and droplet coalescence [*Low and List*, 1982]. However, droplet coalescence occurs at energies nearly four orders of magnitude below those found in particle aggregation [*Beard et al.*, 2002; *Telling and Dufek*, 2012]. *Gilbert et al.* [1991], *James et al.* [2002, 2003] and *Telling and Dufek* [2012] have described particle aggregation behavior in a number of regimes. However, little work has been done to examine how atmospheric residence times might alter the efficiency of ash interactions despite the fact that *Lautze et al.* [2012] and others have shown that ash is chemically and physically altered during transport in volcanic plumes. For accurate aggregation prediction more information is needed about aggregation behavior in high residence time ash, water vapor rich flows and a wider array of particle energies, all of which are expected to be encountered during explosive volcanic eruptions.

Here we present experiments designed to investigate ash aggregation efficiency, the ratio of aggregating particles to the total number of particle collisions, across a range of conditions. In a controlled atmosphere we examined the role of residence time, atmospheric pressure, and humidity on aggregation. Data was collected from two samples of ash and an ash proxy to further allow us to compare how composition might alter aggregation behavior. In the present work we focus on processes occurring above the freezing point of water. The relationships derived from our results can be applied to

volcanic plumes and pyroclastic density currents alike, and fill a gap in our current understanding of aggregation processes.

### **3.2 Methods**

A controlled atmospheric chamber (Figure 3.1) was designed to be evacuated from ambient conditions, at sea level, to 13 kPa, which corresponds to an altitude of roughly 16 km, and a range of relative humidity values, 11-95%, likely encountered in volcanic plumes. Particles, which were released from the top of the tank at varying speeds, collided with a fixed sample to examine variable impact energies. Particle fall velocities were not controlled directly by the experiment but varied naturally between 0.08 m/s and 1.26 m/s depending on when in the experiment the particle was released and the differential pressure between the chamber and the sample holder, which was not depressurized. In order to create a uniform, stationary bed of particles, each target particle sample was adhered to a glass slide using thermal epoxy and we ensured that a monolayer of ash particles was exposed at the surface to both treat the roughness effects of natural ash and to also expose the surface for adsorption of water over time. A Phantom MIRO-4 high-speed camera was positioned directly in front of the tank and used to capture particle interactions at the bed at a rate of 2500 fps.

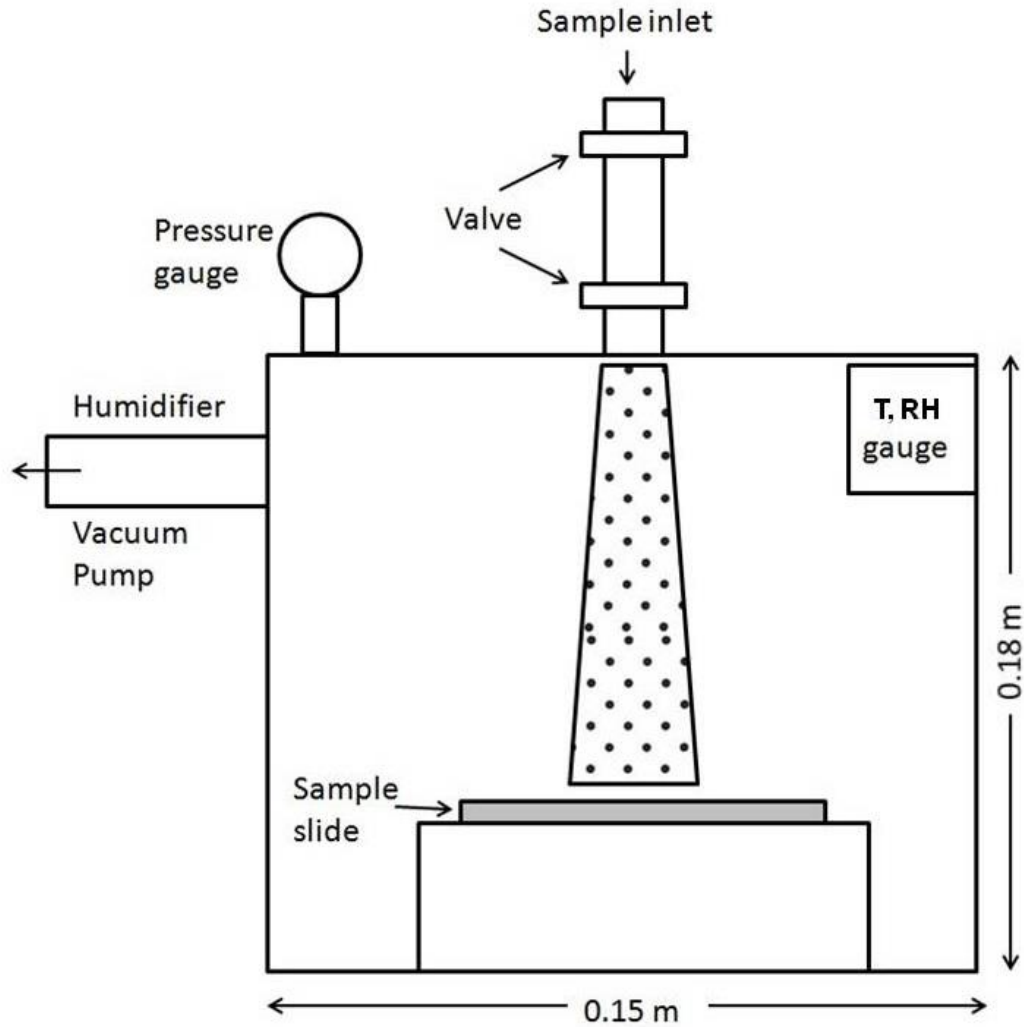


Figure 3.1. Diagram of the experimental setup. The dimensions of the closed chamber were 0.15 m x 0.18 m x 0.15 m. The sample slide was fully coated with particles such that every particle colliding with the plate interacted with another particle and not the glass slide. The camera was placed directly in front of the tank.

Three particle samples were used in the experiments. A sample of ballotini (spherical silica) with a diameter between 90 and 150  $\mu\text{m}$  was used as a proxy for ash. Samples from the Mt. St. Helens, WA, 1980 eruption (dacite composition) and the Tungurahua, Ecuador, 2006 eruption (andesite composition) were also used to examine the potential effect of composition. These ash samples were both sieved to between 90 and 106  $\mu\text{m}$  in diameter. The high humidity experiments required a minimum humidity of

71%, the point at which *Lathem et al.* [2011] predicts monolayer water coverage to begin to form. Most high humidity trials, however, occurred at greater than 90% humidity. Low pressures ranged from 13 kPa to 88 kPa and multiple trials were conducted at roughly 17 kPa intervals. Variable ash residence time was examined by maintaining conditions in the tank between 1 to 150 minutes. Only the fixed sample in the chamber interacted with the environment. The falling particle sample was dry and the sample holder maintained ambient pressure until the valve to the chamber was opened. Thirty to 36 trials were conducted on each of the samples (Appendix B).

A random sample of 20 particles was chosen from every trial, which may include up to 100 particles, and the particles were analyzed manually. We analyzed larger samples (30, 40 and 50 particles) and confirmed that aggregation efficiency was not affected by the sample size of randomly chosen particles. Twenty trials were analyzed by two separate people in order to ensure consistency and minimize aggregation efficiency error to 2.5%.

The position of each particle was tracked from the time it entered the tank until it was no longer visible. Particle positions were recorded in pixels from the raw image frames and converted to meters based on the precise resolution of each trial (Appendix B). Particle positions during the particle fall and, if present, particle bounce were used to calculate velocity and CKE (Eq. 3.1).

$$CKE = \left(\frac{1}{2}\right) \left(\frac{\rho\pi}{6}\right) \left(\frac{d_1^3 d_2^3}{d_1^3 + d_2^3}\right) v^2 \quad \text{Eq. 3.1}$$

where  $\rho$  is the particle density,  $v$  is the differential velocity between the two particles and  $d$  is the particle diameter.

Fall velocities for each particle were measured within 0.01 m/s and used to calculate an approximate CKE and restitution coefficient, the velocity ratio of incoming and outgoing particles, in the case of a bounce event. Particle motion was captured in two dimensional images. Consequently, movement toward or away from the camera could not be accounted for in the measurement of velocity and restitution coefficient. The falling particle sample was designed to fall directly downward and very little forward or backward motion was observed. However, particle bounces could not be similarly controlled so the restitution coefficient values reported are minimum values, since they do not account for possible motion in a third dimension.

Data recorded for each particle included the trial conditions, particle velocity and CKE and the outcome of each interaction, aggregation or bounce. In the event of a bounce, particle velocity was also measured after the collision and used to calculate restitution coefficient.

Aggregation efficiency is the ratio of particles that aggregate to the total number of colliding particles (bounce and aggregation events). The result of every particle interaction, bounce or aggregation, was recorded. Aggregation efficiency was then calculated for all the particles within a given energy range to produce an average aggregation efficiency at specific CKE values (Figure 3.2). In order to clearly represent the distribution of aggregation efficiency values, aggregation efficiency was calculated for random sets of 20 events, aggregation and bounce, in each sample and energy range. This calculation resulted in the spread of values seen in Figure 3.2 (a-d). In Figure 3.7 (e-f), the aggregation efficiency is reported as an average of all the particles in that CKE range and the error oval represents the spread in the data (Figure 3.2 a-d).

Overall, these experiments provided a robust data set considering ash aggregation efficiency as a function of residence time, atmospheric pressure, relative humidity and CKE.

### 3.3 Results

The aggregation efficiencies of all three samples, SiO<sub>2</sub>, Mt. St. Helens (MSH) and Tungurahua (Tu), were found to be sensitive to a range of pressure, relative humidity, residence time and CKE conditions. While CKE is the dominant factor controlling aggregation efficiency [Telling and Dufek, 2012], we also found that high (>71%) relative humidity becomes important when particles interact for long periods of time with the atmosphere (Figure 3.2). The scatter in the data reflects that natural materials were used, each with variable shape and different contact angles during impact, which affect the SiO<sub>2</sub> sample as well. We found a critical residence time by which aggregation efficiency increased by more than 60% over initial conditions for particles with identical CKE between approximately 50 min (MSH) and 110 min (Tu), when a film of water had developed on the fixed sample (Figure 3.3). In the low relative humidity condition, there is little difference between the long and short interaction time aggregation efficiencies (Figure 3.2 a-c). Decreasing atmospheric pressure enhanced CKE (and decreased collision efficiency) due to drag reduction on the particles, but otherwise played no discernible role in the collision dynamics. In general, aggregation behavior for the different compositions showed no systematic variation.

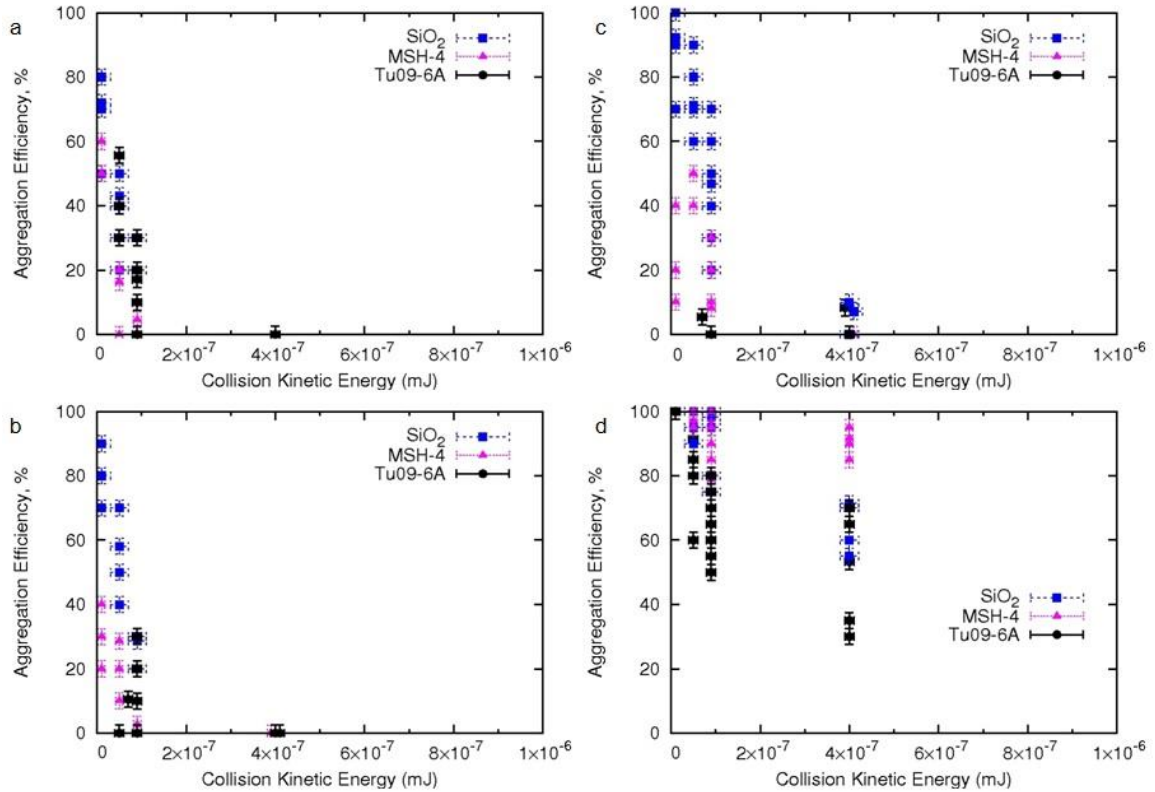


Figure 3.2. Aggregation efficiency of ash particles in (a) low relative humidity (<71%) and low residence time (<50 min), (b) low relative humidity (<71%) and high residence time (>50 min), (c) high relative humidity (>71%) and low residence time (<50 min), and (d) high relative humidity (>71%) and high residence time (>50 min). (a-d) Aggregation efficiency was calculated for random sets of 20 events, aggregation and bounce, in each sample and energy range to represent the spread of values in each data range. The error in aggregation efficiency is  $\sim 2.5\%$ . The error in CKE is based on the individual error of each variable used in the calculation of CKE.

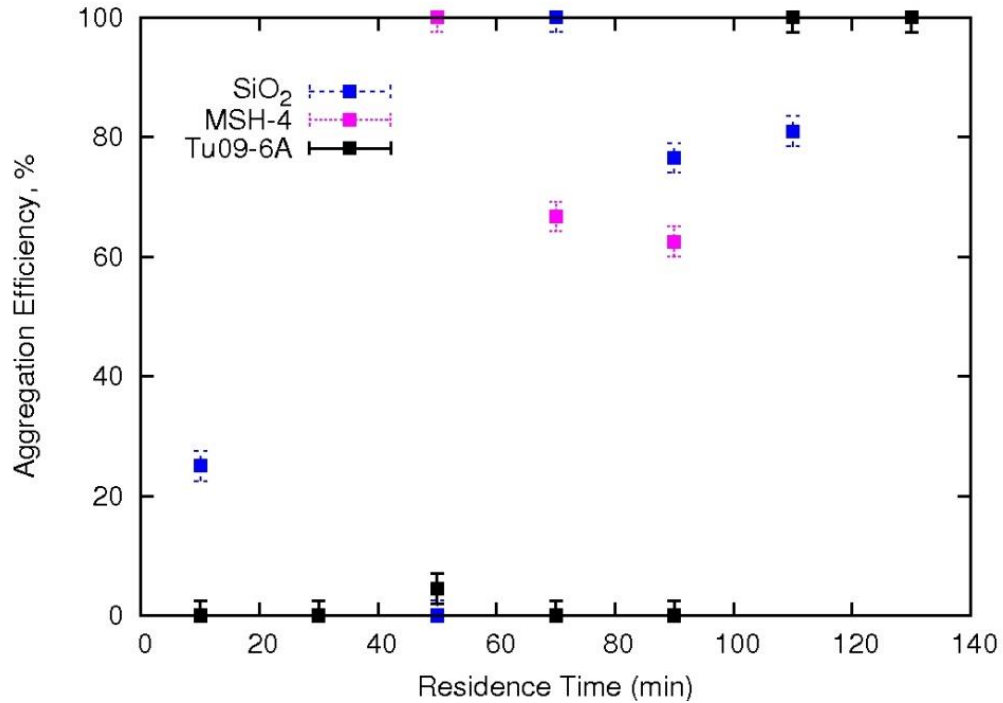


Figure 3.3. Aggregation efficiency as a function of residence time for all particles with CKE between  $2 \times 10^{-7}$  mJ and  $6 \times 10^{-7}$  mJ. A clear increase in aggregation efficiency is seen at 50 min for MSH, 70 min for SiO<sub>2</sub> and 110 min for Tu.

A single ash particle in these experiments, traveling at terminal velocity, that collided with a stationary grain of ash would have a CKE of approximately  $2 \times 10^{-6}$  mJ. In the wet case, these two particles would have roughly a 30% chance of aggregating. In the dry case, the two particles would not aggregate. Alternatively, if the largest particle and smallest particle in our experiments were both traveling at terminal velocity and collided mid-fall, the resultant CKE would be approximately  $6 \times 10^{-8}$  mJ. In the wet case, the particles would have a 90% chance of aggregating. In the dry case, they would have a 50% chance of aggregating.

### 3.4 Discussion

Electrostatic and wet aggregation processes both play a role in volcanic flows. The results of these experiments permit quantification of the flow regimes and conditions

in which each is expected to dominate [Gilbert and Lane, 1994; Telling and Dufek, 2012]. In either regime, a balance of the inertial force of two colliding particles with the force required to arrest the collision, can be used to predict whether a collision will produce an aggregation or bounce event [Schmeekle *et al.*, 2001]. In the case of particles coated by a viscous fluid, the particles can be arrested by hydrodynamic forces [Davis *et al.*, 1986; Schmeekle *et al.*, 2001; Matar *et al.*, 2006]. However, such fluid forces are much weaker in the case of dry particle collisions where the working fluid is air and, in this case, electrostatic stopping forces need to be considered for the formation of particle aggregates.

### **3.4.1 Determining Wet and Dry Flow Regimes**

A film of water was observed at  $RH > 71\%$  and interaction times longer than 50 minutes. In order to confirm the presence of a water layer, the sample slides were each dried and weighed before being placed in the experiment at high relative humidity ( $>71\%$ ). Each slide was weighed at ten minute intervals and a consistent weight increase of 0.1-0.2 g per slide was observed by 50 minutes. The increase in weight, distributed over the surface of the slide, corresponds to a water layer with a depth on the scale of tens of micrometers. Since only the fixed sample developed a water layer, the interaction time required for two wetted particles to see a substantial increase in aggregation efficiency should be less than 50 minutes. We also noted a distinct change in the restitution coefficient behavior of the particles for these conditions (Figure 3.5). The data was split up into two categories- wet, which met these conditions, and dry, which did not. The abrupt change in aggregation (Figure 3.2) and restitution coefficient (Figure 3.5) behavior after a delay period is consistent with the interpretation of water layer growth over this

time period exceeding the roughness scale of the ash particles, which typically ranges from nanometers up to a few micrometers [Delmelle *et al.*, 2007; Carter *et al.*, 2009; Ersoy, 2010].

### 3.4.2 Stokes Number Analysis

As an indicator of the importance of interstitial fluid during impact, we examined the ratio of the relative inertial timescale of a particle to the viscous fluid timescale (i.e. the Stokes number). The Stokes number is defined in Eq. 3.2 where  $m_*$  is the reduced mass,  $u$  is the particle velocity,  $\mu$  is the viscosity of the interstitial fluid at the point of collision and  $r_*$  is the reduced radius.

$$St = \frac{m_* u}{6\pi\mu(r_*^2)} \quad \text{Eq. 3.2}$$

Below a given Stokes number,  $St_{cr-a}$ , all collisions are likely to produce aggregates and above  $St_{cr-b}$  all collisions are likely to result in a bounce. This range of critical Stokes numbers is dependent on the detailed geometry of the collision and the elastic properties of the material [Davis *et al.*, 1986; Schmeckle *et al.*, 2001].

In order to consider how particle Stokes number affects aggregation efficiency, we calculated the number of aggregation and bounce events within a certain bin of Stokes numbers,  $\Delta St = 5$  for the wet case and  $\Delta St = 10$  for the dry case, and determined what percentage of events in that range produced an aggregate (Figure 3.4a). In order to reduce error, bins with only one or two events were combined with neighboring bins. The critical Stokes range for wet SiO<sub>2</sub>, MSH and Tu, respectively, was found to be 13-61, 13-64 and 20-64. These values are on the same order as those in Davis *et al.* [1986], a theoretical examination of critical Stokes number, and Schmeckle *et al.* [2001], which combined

theoretical and experimental methods for larger particles immersed in fluid. *Schmeeckle et al.* [2001] reported Stokes values between 39-105 for round spheres and 82-105 for much larger natural sediment completely immersed in water. It is important to note that particles in the *Schmeeckle et al.* [2001] experiments were moving through water prior to collision with a glass slide instead of moving through air and colliding with a bed of ash particles, as in the work presented here. It is clear that, in the case of high relative humidity, high residence time particle interaction, the Stokes number balance of inertial and hydrodynamic stopping forces is a useful way to predict collision outcomes.

However, in the dry sample, Stokes numbers ranged from 120-4200 (Figure 3.4b) much beyond the range that permits explanation of aggregation due to hydrodynamic forces. As hydrodynamic theory is a poor indicator of particle aggregation for the dry particle case, a different relationship must be used to describe this scenario.

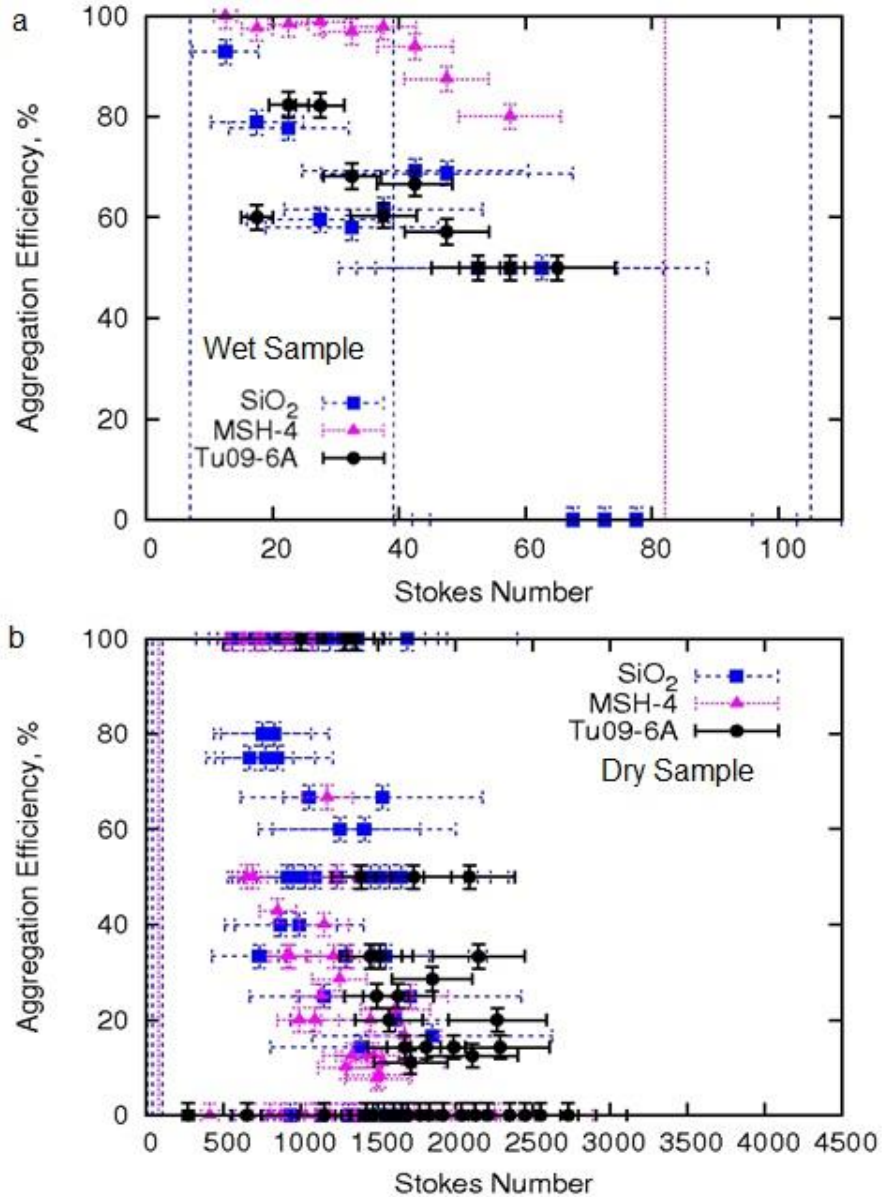


Figure 3.4. (a) The relationship between  $St$  and efficiency for the wet case. Two to 90 individual bounce and aggregation events have been averaged to make each point. (b) The relationship between  $St$  and efficiency for the dry case. Two to 20 events have been averaged to make each point. The blue lines at  $St = 7$  [Davis *et al.*, 1986] and 39 [Schmeeckle *et al.*, 2001] are thresholds below which predicted aggregation efficiency will be 100% based on previous collisional experiments in the presence of viscous fluids. Schmeeckle *et al.* [2001] also proposes a lower limit of  $St = 82$  for natural sediments and an upper limit of  $St = 105$ , above which aggregation efficiency will be 0%. The current results for the wet case provide relatively good agreement with these previous studies; however, the hydrodynamic  $St$  number is a poor fit for the case of dry aggregating particles. The reported aggregation efficiency error is based on the 2.5% error inherent in the data collection. The error in Stokes number was calculated as a percentage of Stokes number based on the individual errors of each variable in Eq. 3.2.

The wet Stokes numbers are larger than unity, and this can in part be explained by variability in contact angle and shape [Schmeeckle *et al.*, 2001]. Also the viscous term appearing in the Stokes scaling is not the only force responsible for arresting the particle motion. The energy dissipated due to surface tension and fluid inertia in the film layer also contributes to lowering the restitution coefficient and promoting aggregation [Gollwitzer *et al.*, 2012]. Including these terms, we calculate the restitution coefficient reduction relative to the dry restitution coefficient as a function of water layer thickness [Gollwitzer *et al.*, 2012]. Figure 3.5a shows the ratio of the wet restitution coefficient relative to the dry coefficient (contour lines) as functions of the water layer thickness relative to the size of the ash particle and as a function of Stokes number. The zero restitution coefficient line is equivalent to aggregation. A clear dampening effect can be seen in all three wet samples (Figure 3.5c).

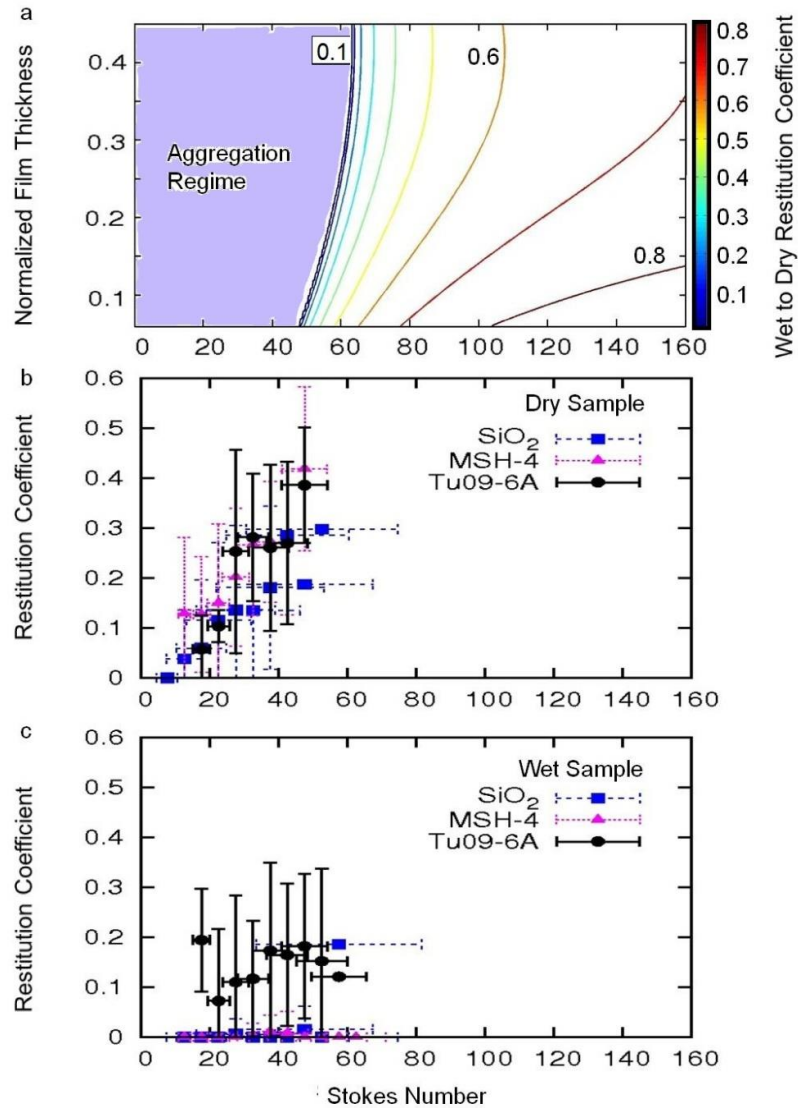


Figure 3.5. (a) The ratio of the wet restitution coefficient relative to the dry coefficient (contour lines). These are presented as functions of the water layer thickness relative to the particle diameter of the ash and as a function of Stokes number. (b) The relationship between restitution coefficient and Stokes number for the dry particle sample. Restitution coefficient is a factor of velocity and scales with Stokes number. For this plot, the restitution coefficient of the dry sample has been calculated using the viscosity of water, not air, so that the restitution coefficient results can be compared on across the same scale of Stokes number values for both the wet and dry samples. (c) The relationship between restitution coefficient and Stokes number for the wet particle sample. A clear dampening effect can be seen in all three samples. Each data point is an average of between 10 and 90 individual bounce and aggregation events in both (b) and (c). The error in restitution coefficient for (b) and (c) is based on the standard deviation and the error in Stokes number is calculated based on propagating error of each variable used in the calculation of  $St$ .

Surface tension and fluid inertia in the film layer also contribute to lowering the restitution coefficient and promoting aggregation in the case of particles colliding with a substrate covered by a thin layer of fluid [Gollwitzer *et al.*, 2012]. Including these extra terms (Eq. 3.3), we can compute the restitution coefficient reduction relative to the dry restitution coefficient as a function of water layer thickness [Gollwitzer *et al.*, 2012].  $E_i$  is the CKE and  $\Delta E_{acc}$  is the kinetic energy required to move the interstitial fluid out of the way of two colliding particles.  $\Delta E_{visc}$  is the viscous dampening experienced by the particle due to the fluid.  $\Delta E_b$  is the energy required to rupture the capillary fluid bridge during the particle rebound.

$$e_n = \sqrt{e_{dry}^2 - \frac{\Delta E_{acc}}{E_i} - \frac{\Delta E_{visc}}{E_i} - \frac{\Delta E_b}{E_i}} \quad \text{Eq. 3.3}$$

### 3.4.3 The Inertial-Electrostatic Ratio

Electrostatic aggregation is the most likely mechanism to explain aggregation in the cases where particles are not covered by a water layer. As particles become charged through particle - particle collisions or during initial fragmentation [Gilbert *et al.*, 1991; Gilbert and Lane, 1994], electrostatic bonds form, creating loosely bound aggregates. In this case, the arresting force is not viscous fluid in the space between the particles [Schmeeckle *et al.*, 2001] but an electrostatic force. We define the ratio of inertial to electrostatic forces as the inertial-electrostatic (IE) ratio (Eq. 3.4), where  $\delta$  is the distance between the two charges,  $m_*$  is the reduced mass of the particles,  $u$  is the collisional velocity,  $k$  is Coulomb's constant and  $q$  is the particle charge. Average charge density was estimated for the particles based on the range of charge estimates of Gilbert and

Lane [1994], James et al. [2003] and Telling and Dufek [2012]. As the IE ratio approaches one or greater, aggregation efficiency should decay to zero (Figure 3.6).

$$IERatio = \left( \frac{\delta m_* u^2}{kq^2} \right) \quad (\text{Eq. 3.4})$$

The IE ratio was calculated for the data as well as for two theoretical particles with the highest,  $10^{-3}$  C/kg [James et al., 2003], and lowest,  $2 \times 10^{-4}$  C/kg [Telling and Dufek, 2012], charge mass densities reported in the literature. Theoretical calculations of the IE ratio, Eq. 3.4, and aggregation efficiency, Telling and Dufek [2012], suggest that aggregation efficiency might range from 0.2 to 51% when the IE ratio equals one. The data collected for dry particles in these experiments falls into this range, with the MSH and Tu samples approaching zero efficiency at IE ratio values near 1 and SiO<sub>2</sub> efficiencies of no more than 50% as the IE ratio approaches one (Figure 3.6).

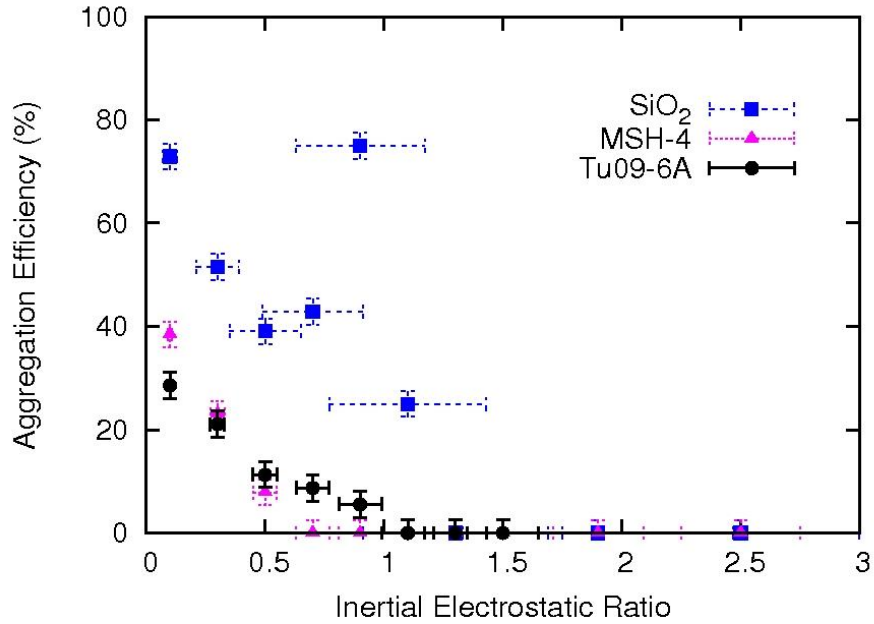


Figure 3.6. The relationship between the IE ratio and aggregation efficiency for the dry particle sample. Each data point includes between 10 and 40 individual bounce and aggregation events. The error on aggregation efficiency  $\sim 2.5\%$  and the error in the IE Ratio was calculated as a percentage based on the propagating error of each variable in Eq. 2.

### 3.4.4 Implications for Volcanic Modeling

During a collision, energy is dissipated through deformation, acoustic energy, heating and other processes. These effects are usually grouped into a restitution coefficient,  $e$ , which gives the ratio between the velocity after a collision to that before the collision. For inelastic particles,  $e$  is less than one and the energy change during a collision can be described as

$$\Delta E = E_i - e_0^2 E_i = (1 - e_0^2) E_i, \quad \text{Eq. 3.5}$$

where  $e_0$  is the 'intrinsic' restitution coefficient. If the restitution coefficient is equal to zero, aggregation occurs.

In the electrostatic case, the Coulomb force between particles also acts to dissipate energy after the collision takes place. In the wet case, surface tension and fluid inertia in the film layer contribute to lowering the restitution coefficient and promoting aggregation [Gollwitzer *et al*, 2012]. We can develop a process-based set of equations suitable for use in numerical modeling that defines the behavior of ash particles described in these experiments. One of the largest sources of variability for any given collision is the ash morphology and contact angle during collision. As ash particles will all be different it is impossible to *a priori* determine these features. We propose describing this variability through a probability distribution,

$$f_E = \frac{1}{2\sqrt{\pi}\sigma_{diss}} \exp\left[\frac{-E_{diss}}{4\sigma_{diss}}\right], \quad \text{Eq. 3.6,}$$

where  $\bar{E}_{diss}$  is a generic dissipation mechanism (either electrostatic or hydrodynamic) that can be described through a physical law and  $\sigma_{diss}$  represents the variability arising from particle shape and uncertainty in evaluating the physical parameters. In the case of

electrostatic aggregation, the dissipation is due to oppositely charged particles,  $E_{elec}$  (Eq. 3.7), and the charge is approximately  $4 \times 10^{-8}$  mJ using estimates of charge density from *James et al.* [2003] and *Telling and Dufek* [2012].

$$\bar{E}_{elec} = \frac{kq_1q_2}{r} \quad \text{Eq. 3.7}$$

In the case of hydrodynamic aggregation, using the approach of *Gollwitzer et al.* [2012], we calculate the dissipation is composed of the viscous dampening experienced by the particle (Eq. 3.8) due to the fluid,  $E_{visc}$ ,  $8.7 \times 10^{-8}$  mJ, the kinetic energy change in the fluid due to the collision,  $E_{acc}$ ,  $4.3 \times 10^{-8}$  mJ, and the surface energy change of the fluid,  $E_b$ ,  $8.4 \times 10^{-7}$  mJ.

$$E_{hyd} = \Delta E_{acc} + \Delta E_{visc} + \Delta E_b \quad \text{Eq. 3.8}$$

Integrating this probability distribution for all dissipation energies that exceed the initial inertial energy of the particle,  $E_i$ , and incorporating the energy loss described by the initial restitution coefficient,  $e_0$ , approximately 0.4, gives the following set of equations for the aggregation fraction,  $F_{agg}$ , for the electrostatic,

$$F_{agg} = 1 - \frac{1}{2} \left[ 1 + \operatorname{erf} \left[ \frac{E_i - (1 - e_0)^2 E_i - E_{elec}}{\sqrt{2\sigma_{Diss}^2}} \right] \right], \quad \text{Eq. 3.9}$$

and hydrodynamic cases

$$F_{agg} = 1 - \frac{1}{2} \left[ 1 + \operatorname{erf} \left[ \frac{E_i - (1 - e_0)^2 E_i - E_{visc} - E_{acc} - E_b}{\sqrt{2\sigma_{Diss}^2}} \right] \right]. \quad \text{Eq. 3.10}$$

The variance,  $\sigma_{Diss}$ , was varied systematically to obtain the best fit between the data and this model, while the energy components were calculated based on the physical properties of the ash and interstitial fluid using the approach of *Gollwitzer et al.* [2012].

In the wet case,  $\sigma_{\text{wet}}$  was equal to  $6.9 \times 10^{-10}$ . In the dry case, we also varied the charge to mass ratio between the values presented in *James et al.* [2003] and *Telling and Dufek* [2012] so a best fit was found for  $\sigma$  at a given charge to mass ratio.  $\sigma_{\text{dry}}$  is equal to  $7.4 \times 10^{-11}$  and was found at  $5 \times 10^{-4}$  C/kg, providing a rough estimate of particle charge in these experiments.

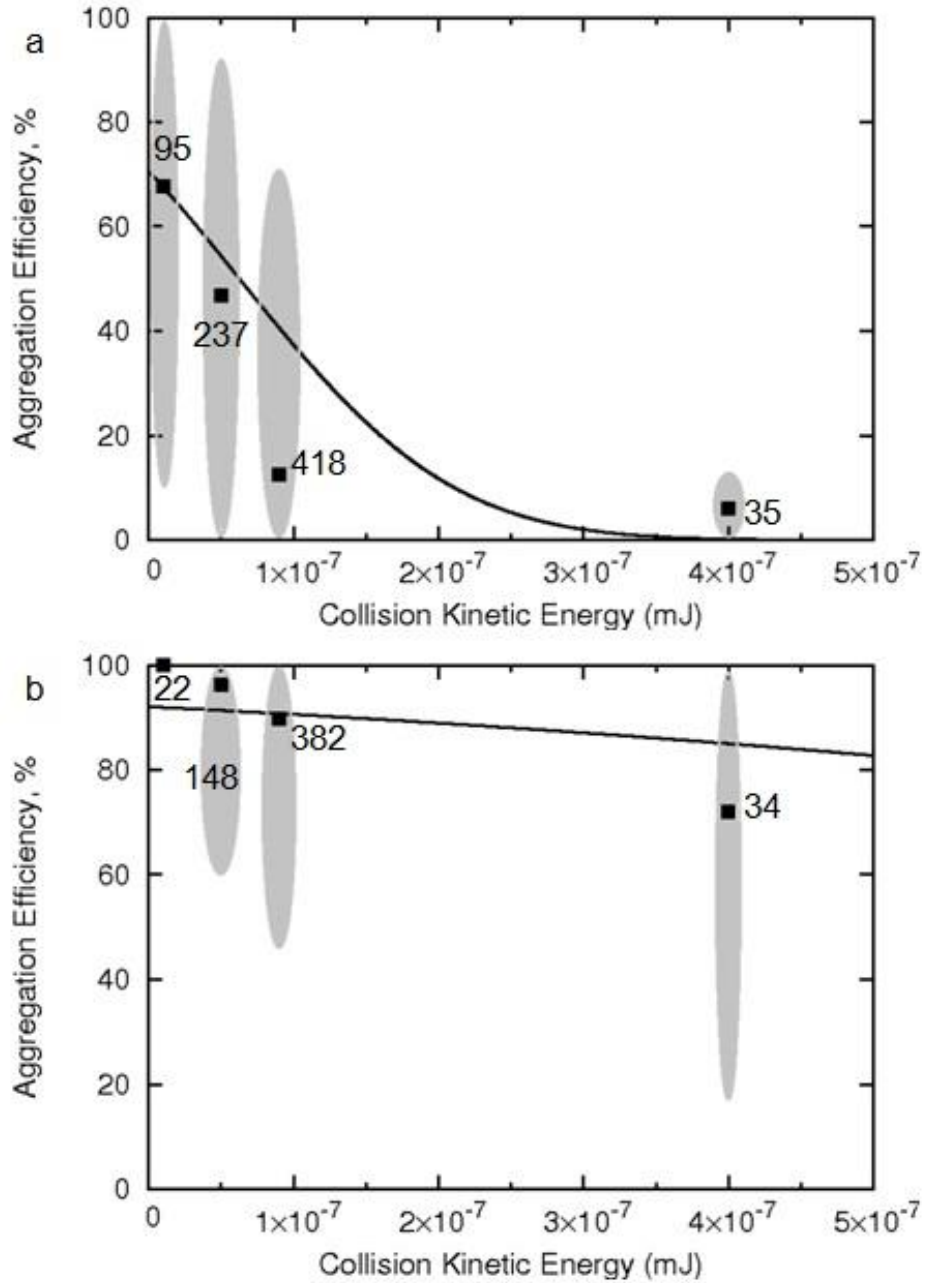


Figure 3.7. (a) The dry case, which includes Figure 3.2a-c is fit using Eq. 3.9. Aggregation efficiency was calculated as an average of all the collision events in these two figures. The numbers next to the data points represent the total number of bounce and aggregation events that were averaged to make each point. (b) The wet case (Figure 3.2d) has been fit using Eq. 3.10. The ellipses around each point represent the scatter in the aggregation efficiency measurement (Figure 3.2a-d) and the solid squares represent mean values. Aggregation efficiency was calculated as an average of all the collision events in these two figures. The numbers next to the data points represent the total number of bounce and aggregation events that were averaged to make each point.

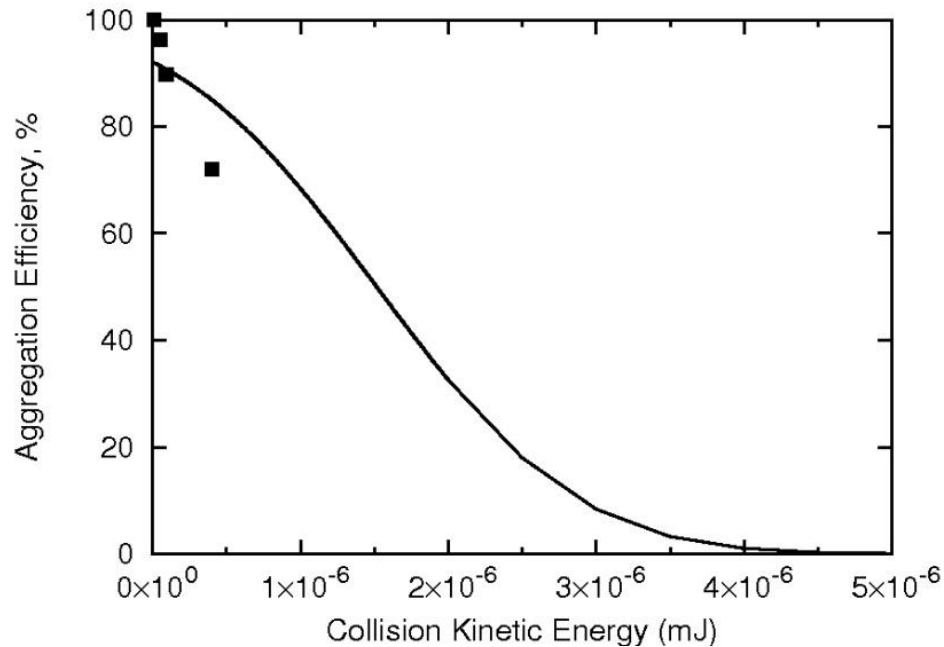


Figure 3.8. This is the full range of CKE values across which wet particles can aggregate successfully. Aggregation efficiency for the wet case approaches zero at CKE values an order of magnitude higher than in the dry case.

These fits (Figure 3.7 a-b) provide a probabilistic approach to calculating aggregation and can be incorporated into large-scale models of ash dispersal.

### 3.5 Conclusions

We present a set of experiments that investigates the importance of CKE, atmospheric pressure, residence time and subsaturated relative humidity on the aggregation potential of volcanic ash and an ash proxy. CKE is the most diagnostic parameter for ash aggregation efficiency. Relative humidity was found to become important for particles that had long residence times in a high humidity environment. In pyroclastic flows these residence times may occur during propagation, in the recirculation region near the volcanic vent or in co-ignimbrite plumes [Brown *et al.*, 2010]. In volcanic plumes residence time of fine to very fine ash can last from > 30 minutes to >10 days, often in water vapor rich environments [Rose and Durant, 2011].

The physics of wet aggregation, in high relative humidity, high residence time conditions, can be described accurately by hydrodynamic theory. Electrostatic ash aggregation is dominant in humidity regimes below 71% relative humidity and in fresh particles. For these cases, the inertial - electrostatic ratio was developed to describe aggregation efficiency. Probabilistic relationships were developed for the wet and dry cases to predict aggregation efficiency in terms of balancing the appropriate forces present during a collision. These equations can be incorporated into numerical models to improve hazards predictions and further our understanding of how pyroclastic density currents and volcanic plumes develop. Further work is required to develop a probabilistic relationship for ice-ash interactions.

# **CHAPTER 4**

## **MODELLING ASH AGGREGATION AT KILAUEA**

### **4.1 Introduction**

The historic eruption of Kilauea volcano in 1790 produced uniquely well preserved deposits rich in accretionary lapilli (AL) (Mastin, 1997; Swanson et al, 2012a). The eruption was witnessed by native Hawaiians living on the island and recorded by European visitors to Hawaii in the early 1800's (Dibble, 1843; Jaggar, 1921). The ash deposits are often called the "Footprints ash" because footprints of people walking through the fresh, wet ash deposits have been preserved since the time of the eruption (Personal correspondence- Don Swanson). Kilauea volcano is located on the south side of the island of Hawaii and is part of the Hawaii Volcanoes National Park (Figure 4.1).

Kilauea is a shield volcano that has been active throughout nearly all of its recorded history and is one of the most active volcanoes on Earth (Walker, 2000). The volcano expands outward, toward the ocean, at an average rate of decimeters per year (Walker, 2000) as fresh magma expands the dike system underlying the volcano. Currently, the magma storage zone for Kilauea resides 2-6 km below the surface (Carrigan, 2000); however, for roughly 100 years prior to 1924, there was a lava lake present at the surface in Halemaumau crater (Walker, 2000). The draining of the lava lake was accompanied by explosive eruptive activity due to the combination of both magma and water at or near the surface of the volcano (Walker, 2000).

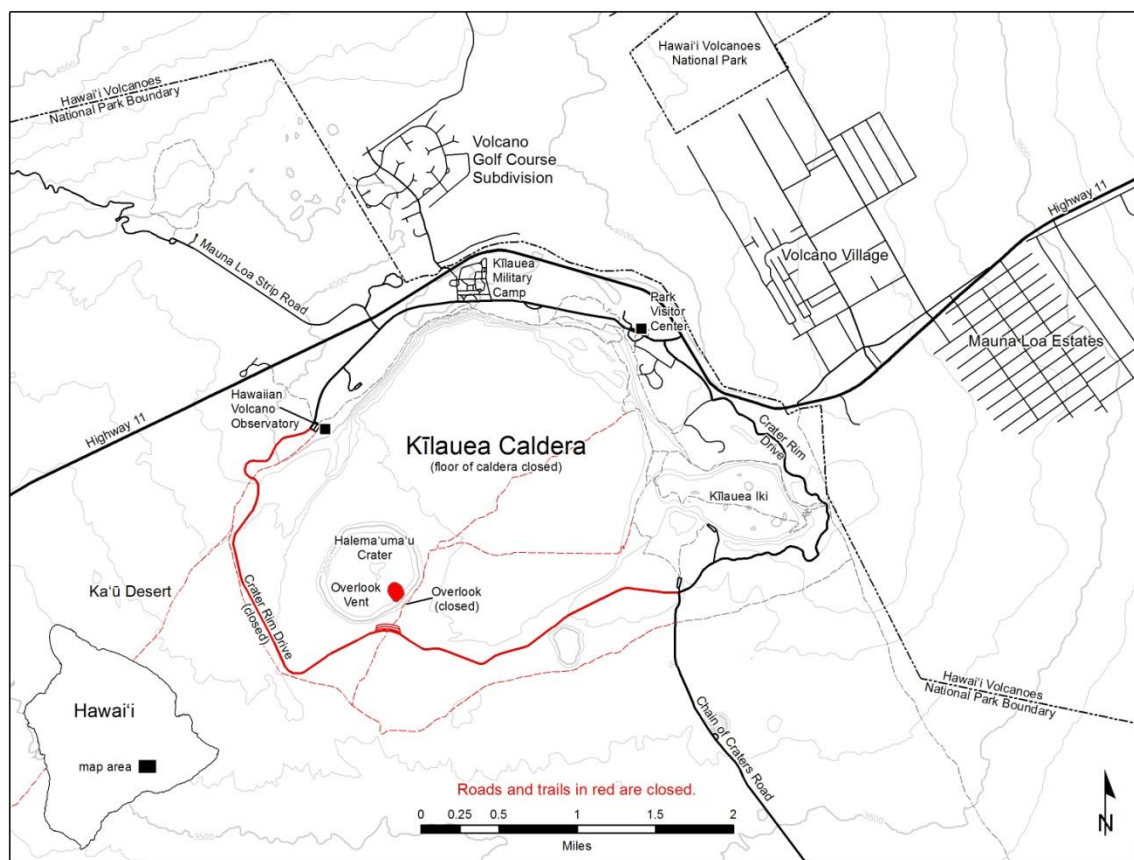


Figure 4.1. USGS map of Kilauea Volcano with an inset of the volcano location on the island of Hawai'i.

Due to the timing of the 1790 eruption, which predates scientific study of the volcano, there remains significant uncertainty in the source conditions. In general, Hawaiian magmas have relatively low magmatic water content and erupt effusively; the explosivity of this eruption is likely indicative of the incorporation of water in the volcanic edifice. Eruptions caused by interaction between groundwater or surface water and magma are known as phreatomagmatic eruptions (Morrissey et al., 2000). While phreatomagmatic eruptions can span a wide range of eruptive activity, they are characterized by the production of steam, resulting from the rapid heating of the water

interacting with the magmatic system, intense fragmentation marking the transition from a continuous melt with a dispersed gas phase to disconnected fragments of glassy, quenched melt, the ejection of rock surrounding the volcanic system and in general a fine grain size distribution (Morrissey et al., 2000).

Multiple sources agree that the eruption was phreatomagmatic (Mastin, 1997; McPhie et al., 1990; Swanson et al., 2012a) but the source of the water remains contested. McPhie et al. (1990) suggests that the eruption was initiated when water at or near the water table interacted with magma in the vent conduit. Kilauea had been active for approximately 300 years prior to the 1790 eruption (Swanson et al., 2010b) and McPhie et al. (1990) proposed that, in an eruptive lull, the magma receded to below the water table, located roughly 500 m below the surface. Once the level of the magma in the conduit at Kilauea was below the water table, McPhie et al. (1990) proposed that there was an inflow of groundwater from the surrounding aquifer that initiated the 1790 eruption of Kilauea. However, Mastin (1997) suggests that an inflow of water from a ground source into the volcanic conduit was unlikely and that the water source was more likely to be located at the surface. The key difference between the two studies is the interpretation of eruptive layers. McPhie et al. (1990) interprets the difference between eruptive layers in the deposit to indicate pauses in the eruption cycle that would have allowed for the recession of magma below the water table and a subsequent inflow of water into the conduit, reinitiating explosive activity. Mastin (1997), however, suggests that there is not sufficient evidence in the deposits to conclude that there were pauses in the eruptive activity that would have allowed for the magma – water interaction proposed in McPhie et al. (1990). Swanson et al. (2012a) examined ballistic blocks around Kilauea

caldera and, modeling their trajectories through EJECT! (Mastin, 2001), found that they could reasonably have been emplaced from an explosion depth of 600m, which is the approximate elevation of the water table. Swanson et al. (2012a) does note though that the precise vent location is not known and that a different vent location could alter this interpretation.

The deposits from the 1790 eruption of Kilauea are densely populated with accretionary lapilli (Figure 4.2). Extensive field work has been done to map their distribution around the volcano (Swanson, 2012- AGU) and in deposit stratigraphy (McPhie et al., 1990; Mastin, 1997). McPhie et al. (1990) includes the footprints ash in Unit 9 of the stratigraphy and Mastin (1997) places it in Unit III, just above a notable surge unconformity that does not appear as prominently in McPhie et al. (1990). A dataset containing the maximum and average accretionary lapilli sizes at hundreds of sites has been compiled to give a detailed picture of their distribution (Personal correspondence- Don Swanson). The locations of the largest accretionary lapilli and isobars describing the locations are shown in Figure 4.3. The largest accretionary lapilli are located west of the presumed vent location, which has been marked with an open black circle.



Figure 4.2. Accretionary lapilli collected at Kilauea from the Footprints Ash deposit. The accretionary lapilli on the right is the largest sample collected from the deposit, with a diameter of approximately 3 cm. Photo courtesy of the USGS.

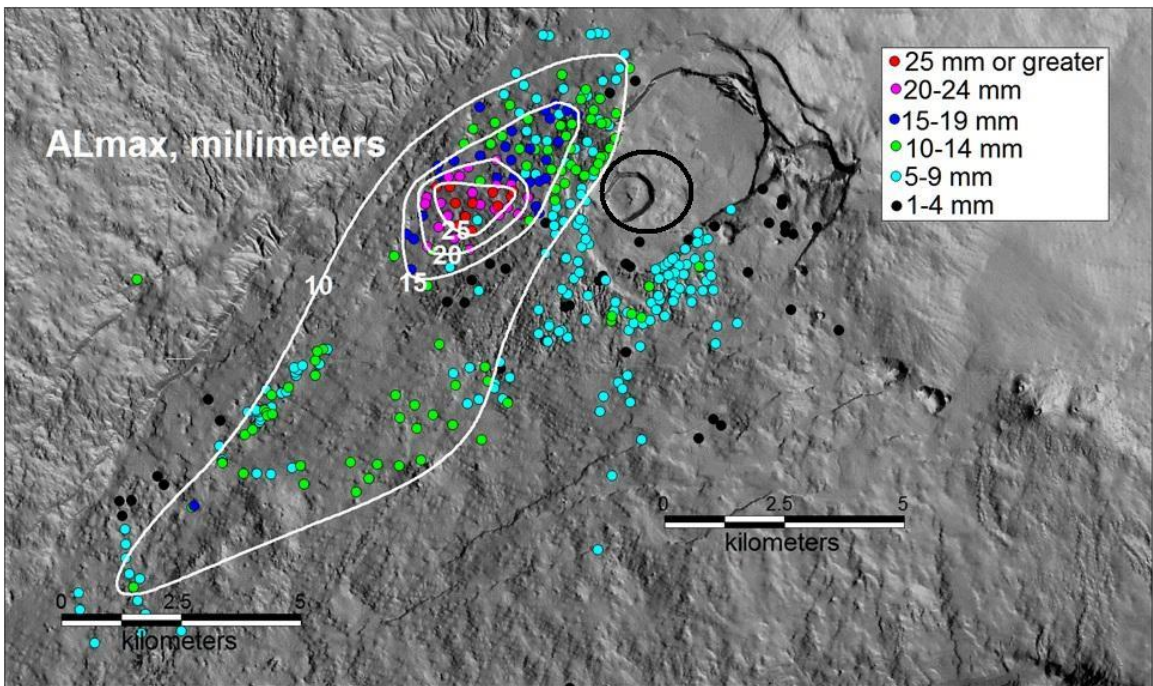


Figure 4.3. Topographic map of Kilauea Volcano with the presumed vent location marked with an open black circle. The location of the largest accretionary lapilli in each sample area is marked on the map with isobars to describe their distribution.

Understanding where and how ash is removed from the atmosphere is crucial to improving predictions of atmospheric ash transport (Folch et al., 2010; Textor et al., 2006a). The final distribution of ash that has been removed by aggregation has been

observed to be different than the distribution of ash removed by settling alone (Folch et al., 2010; Textor et al., 2006a; Veitch and Woods, 2001). Textor et al. (2006b) modeled a generalized large, buoyant eruption and found that aggregation could remove roughly 50% of the ash mass from the lower atmosphere and 30% from the troposphere. It is clear that understanding how much ash is removed by aggregation, and where these processes take place, makes a significant difference to the fraction of ash available for long range transport away from a volcanic source.

It is unclear whether aggregation removed material primarily from fall or flow regimes during the 1790 eruption of Kilauea. The ash deposits have been shown to include both pyroclastic flow and fall material (Mastin, 1997; McPhie et al., 1990; Swanson et al., 2012). Deposition of the Footprints ash layer primarily extends SW from the presumed vent, implying that the local wind field exercised an important control over the eruption (Personal correspondence- Don Swanson) (Figure 4.3). McPhie et al. (1990) also depicts the deposit to be “well sorted” and layered in the cross section and accompanying summary. These indicators typically suggest that the deposit was emplaced by a buoyant column.

However, the cross section presented in Mastin (1997) includes flow discontinuities in the layer directly above the Footprints ash and McPhie et al. (1990) show flow discontinuities in the middle of the Footprints ash section. Based on the lack of deposits east of the vent, the eruption did not interact with the jet stream winds, which show a direction shift towards 270° as low as 5 km over the Hawaiian Islands. A buoyant plume would have had to remain very low in the atmosphere to not interact with the jet stream, which may significantly reduce the time in which accretionary lapilli could form.

The deposits, however, include a large number of well developed, large accretionary lapilli (Mastin, 1997; McPhie et al., 1990; Swanson et al., 2012). Finally, if the accretionary lapilli were forming in a low, buoyant column, they should be removed closer to the vent than the fine ash. The largest accretionary lapilli formed downwind of the thickest fine ash deposits (Personal correspondence- Don Swanson); however, the grain size distribution of the component ash in these accretionary lapilli has not been measured. There is evidence to suggest either a buoyant or collapsing eruption column, and it is likely that both may have been present during the eruption.

We will be modeling the 1790 eruption of Kilauea using an Eulerian-Eulerian-Lagrangian (EEL) numerical model (Dufek and Bergantz, 2007; Dufek and Manga, 2008; Dufek et al., 2009). Including the relationships driving aggregation efficiency (Telling et al., 2013) is the first step towards modeling this eruption. The integration of a joint collision and aggregation function to the EEL model is presented. The new model is tested on one possible eruptive scenario for the Kilauea 1790 eruption. Analysis of the mass fraction of aggregates over time and the volume fraction and aggregation rate of different ash size ranges will be used to determine where and how effectively aggregation processes can remove ash from the atmosphere.

## **4.2 Methods**

### **4.2.1 Model Characterization**

Dufek and Bergantz (2007) developed a continuum multiphase numerical model, based on the multiphase flow with interphase exchange (MFIx) code. The model solves the conservation equations for momentum, mass and energy and includes closure

assumptions for heat and momentum transfer between phases. Six phases were solved in the model- water, gas and four particle phases (Table 4.1).

Table 4.1. Initial particle size distribution

| Name    | Range  | % Volume | Mode ( $\mu\text{m}$ ) |
|---------|--|----------|------------------------|
| Ash - 1 | $d < 30 \mu\text{m}$                         | 15       | 20                     |
| Ash - 2 | $30 \mu\text{m} \leq d < 1000 \mu\text{m}$   | 65       | 250                    |
| Ash - 3 | $1000 \mu\text{m} \leq d < 2000 \mu\text{m}$ | 20       | 1000                   |
| Lapilli | $d \geq 2000 \mu\text{m}$                    | 0        |                        |

The particle size ranges are based on the work of Rose and Durant (2009), who define the Ash-1 and Ash-2 size ranges as very fine ash and fine ash respectively, and Gislason et al. (2011). Ash size data has not been collected for the footprints member of the 1790 eruption of Kilauea. However, detailed grain size analysis of Unit II and the top Golden Pumice unit have been collected (Personal Correspondence- Larry Mastin). Field observations confirm that the footprints ash layer is predominantly fine with a significant fraction of ash falling into the Ash-1 and Ash-2 categories. Of the 53 grain size distributions collected by Mastin (Personal Correspondence), during field campaigns in 1992, 1994 and 2001, three had a predominantly coarse distribution that fell into the Ash-3 category. The remaining 50 grain size distributions were used to define the initial grain size distribution defined in Table 4.1.

#### 4.2.2 Incorporating Aggregation

The probabilistic aggregation relationships developed in Telling et al. (2013) were included as a subgrid model in the numerical simulation. Colliding particles are treated

based on two flow regimes- wet and dry. A wet collision takes place when a particle is covered in a water layer thicker than the particle surface roughness (Telling et al., 2013). The interstitial water acts as a viscous dampening force both slowing the two colliding particles directly prior to a collision and retarding the post-collision rebound, which promotes aggregation. Dry collisions may also result in aggregation due to the electrostatic forces between particles (Telling et al., 2013). Particle collisions and fragmentation are both capable of producing charged particles (Gilbert et al., 1991; James et al., 2002, 2003) though these dry aggregates typically disintegrate upon deposition (Gilbert and Lane, 1994). In this work we consider any collision occurring in above saturated conditions to be influenced by hydrodynamic interactions.

Due to the decline of aggregation with increasing CKE, we can linearize the aggregation fraction and remain within the error of the experimental measurements simplifying the aggregation calculations. The wet aggregation fraction can be rewritten as

$$F_{agg} = 1 - (4.035 \times 10^8) \pi r^3 \rho_p \Delta u^2, \quad \text{Eq. 4.1}$$

where  $\Delta u$  is the relative collision velocity,  $r$  is the reduced radius and  $\rho_p$  is the particle density. The constants  $(4.035 \times 10^8 r^3 \pi \rho_p)$  can be grouped together into one term,  $B$ , so that

$$F_{agg} = 1 - B \Delta u^2. \quad \text{Eq. 4.2}$$

The aggregation fraction must fall between 0 and 1 so a range of velocities in which aggregation will occur can be calculated. Collisional velocities that may produce

an aggregation event will range between zero and  $\frac{1}{\sqrt{B}}$ . The probability distribution for collisional velocity,  $f_{coll}$ , is

$$f_{coll} = \frac{1}{2\sqrt{\pi\theta}} \exp\left[-\frac{(\Delta u^2)}{4\theta}\right], \quad \text{Eq. 4.3}$$

where  $\theta$  is the granular temperature.

The joint probability distribution can be calculated using

$$ff_{aggregate} = 2 \int_0^{\frac{1}{\sqrt{B}}} \frac{1}{2\sqrt{\pi\theta}} \exp\left[-\frac{(\Delta u^2)}{4\theta}\right] [1 - B\Delta u^2] du \quad \text{Eq. 4.4}$$

and, after integration, the final expression for the aggregation potential of the wet case is

$$ff_{aggregate} = \text{erf}\left[\frac{1}{2\sqrt{B\theta}}\right] - 2B\theta \text{erf}\left[\frac{1}{2\sqrt{B\theta}}\right] + \frac{2\sqrt{B\theta} \exp\left[\frac{-1}{4B\theta}\right]}{\sqrt{\pi}}. \quad \text{Eq. 4.5}$$

### 4.2.3 Topographic and Atmospheric Characteristics

We conducted a series of two-dimensional simulations to determine the aggregation potential. An NE-SW running axis that runs through the center of the assumed vent and parallel to the primary ash fallout was chosen to run the simulation along (Figure 4.4). The simulation has refined resolution near the surface with a peak resolution of 20 m.

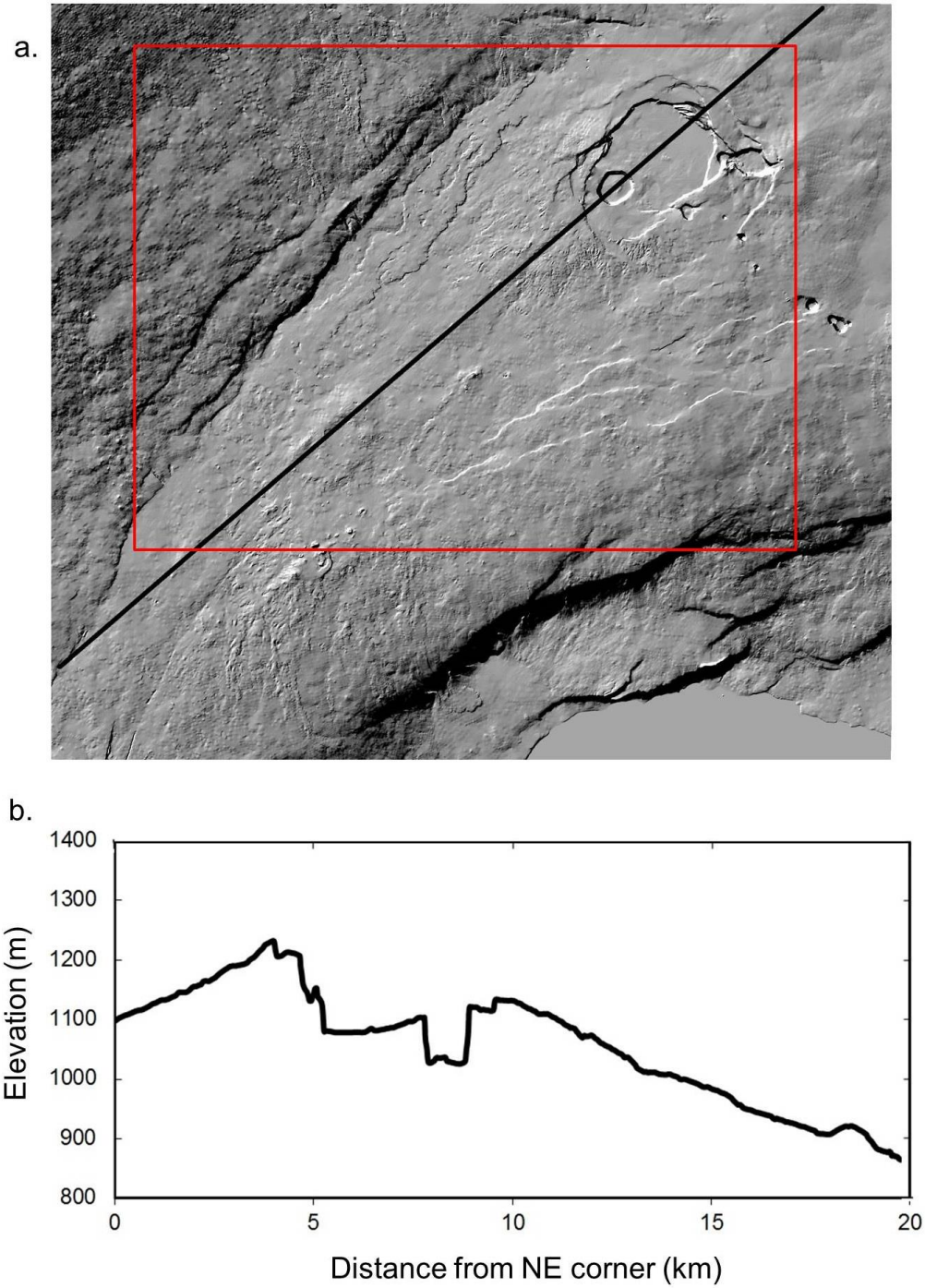


Figure 4.4. (a) Hillslope relief topography surrounding the Kilauea vent. The black line shows the cross section used for topography in the model. (b) Topography across the Kilauea vent, located at roughly 8km. The topography profile runs from the NE to the SW.

Since no atmospheric soundings are available for the day of the eruption, we used atmospheric soundings from a representative day to profile the temperature, relative humidity, lapse rate and pressure in the atmosphere. Ash dispersal from the eruption was primarily carried W-SW of the vent. The jet stream over Hawaii is historically stable between 4-15 km and typically moves from East to West (Figure 4.5). Wind speed and heading data, from the weather station at Hilo International Airport, HI (PHTO), for two months (61 days) was compiled to describe a characteristic wind field over Hawaii. The lack of ash dispersal to the East of the vent suggests that the plume was definitely less than 15 km high and likely less than 5 km high, which is the altitude at which the winds begin to shift towards the jet stream heading of 270°. An average surface wind field was developed by sampling data from the PHTO weather station, which is the closest station to the vent. The SE direction of the ash deposits indicate that surface winds came from the NE on the day of the eruption. Northeasterly winds were averaged across a one year data range to determine a wind field proxy. The average wind direction was 70° with a speed of 10 knots.

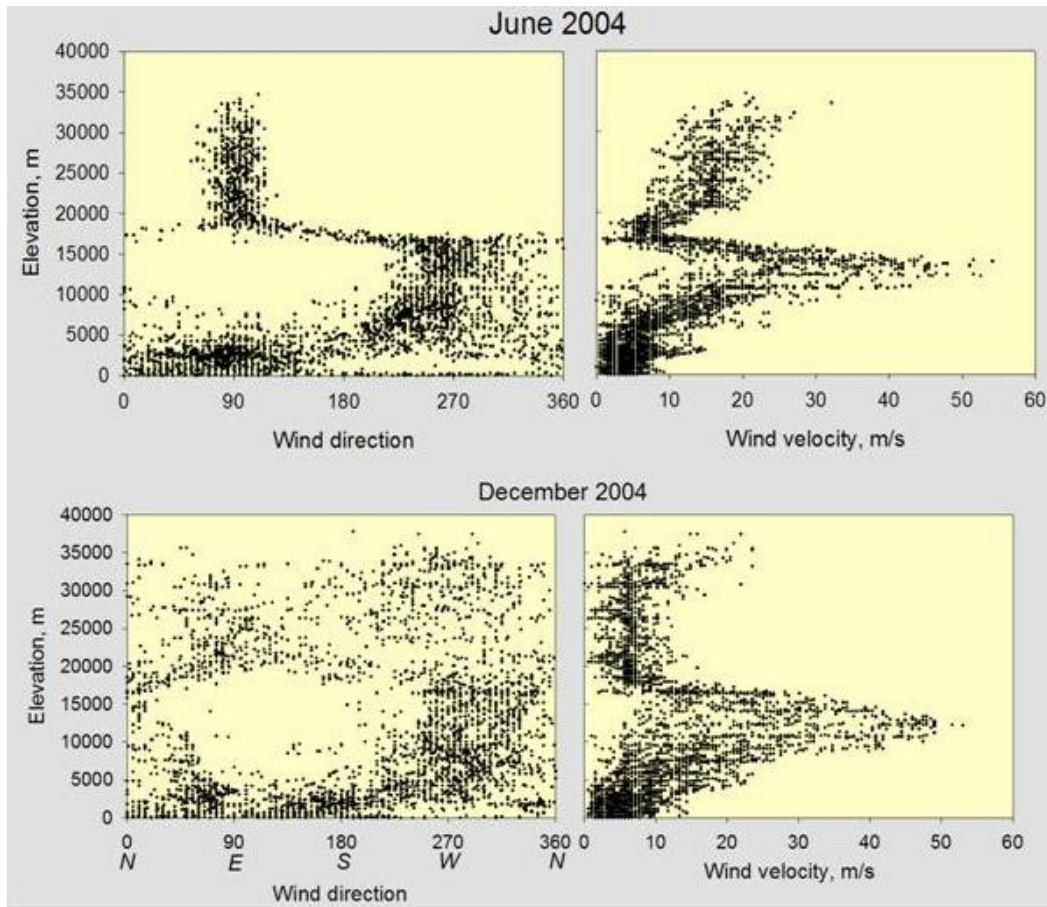


Figure 4.5. Wind direction and speed data for 61 days of 2004.

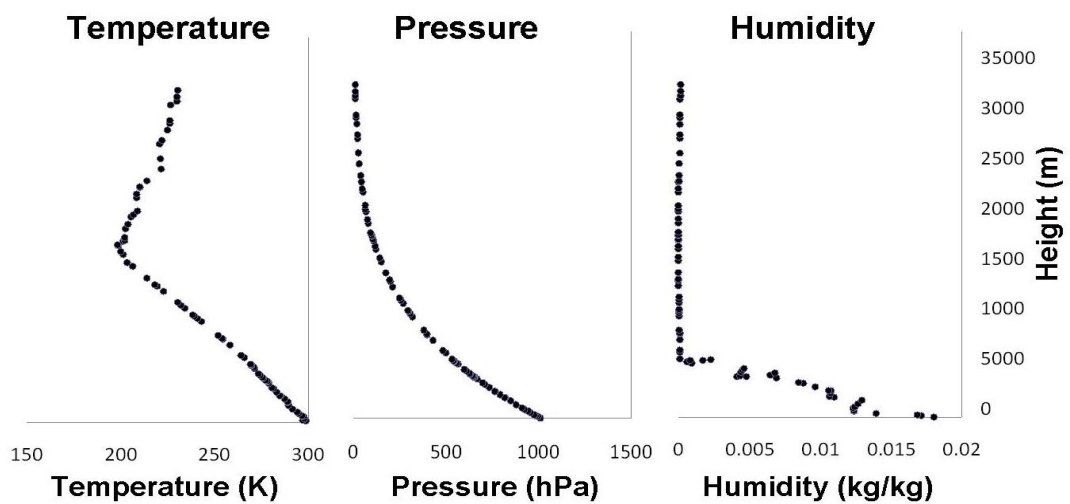


Figure 4.6. Atmospheric soundings used to create the background atmosphere during the eruption. Temperature, pressure and humidity, with respect to altitude, are all shown.

#### **4.2.4 Simulations**

The two eruptive scenarios give rise to an array of possible eruptive conditions. Estimates of explosive depth range from 400 - 700 m below the caldera rim, which used as a reference point in the literature (McPhie et al., 1990; Mastin, 1997; Swanson et al., 2012a). The approximate depth of the caldera floor below the rim was estimated in the 1820's to be 400 m. Consequently, 400 m corresponds roughly to the caldera surface and 700 m depth corresponds to an elevation of 500 m with an overlying lithostatic load of approximately 300 m. The water table depth is estimated to be 500 m (McPhie et al., 1990) to 600 m (Mastin, 1997; Swanson et al., 2012a) below the caldera rim, providing the deepest estimate for the initiation depth of the eruption. Overpressure values range from 10 - 30 MPa (Mastin, 1997). Mastin (1997) based this range on the pressure required in the conduit, considering the lithostatic load of degassed magma, to produce an eruption. The maximum estimate of 30 MPa is actually above the required pressure but is included to test a complete range of conditions for different eruptive scenarios. Appendix C summarizes the 12 numerical simulations that would test this range of data. Due to computational constraints, one simulation was run for this study to test the model. The depth of the eruption source was located 650 – 700 m below the surface and the overpressure caused by the magma – water interaction was estimated to be 1.9 MPa. This test simulation roughly corresponds to Run 11 in Appendix C.

#### **4.3 Simulation Results**

The trial simulation had an explosive source depth of 650-700 m and an overpressure of 19 MPa, roughly corresponding to Run 11 in Appendix C. This

simulation is a test of the aggregation relationships in the framework of a multifluid model and the results presented are not necessarily the best fit to the 1790 eruption of Kilauea. The test eruption produced a PDC that spread out in both directions from the vent and seemed to be controlled only weakly by the ambient wind field. Relative humidity, particle volume fraction, aggregation rates, cumulative aggregation and deposit thickness were all examined.

The mass fraction of aggregates developing throughout the eruption column with time was examined (Figure 4.7). Aggregate formation began roughly 50 s after the initiation of the eruption. The majority of the aggregates were produced in the PDC between the ground and 1200 m (Figure 4.7), a range of the flow that is less than 200 m thick near the vent (Figure 4.4b). A comparatively small amount of aggregate began to form at higher altitudes between 80 and 100 seconds after the initiation of the eruption (Figure 4.7). Roughly 10% of the total aggregate formation occurs between 1200 and 5000 m and, for this eruption, aggregation is negligible above 5000 m.

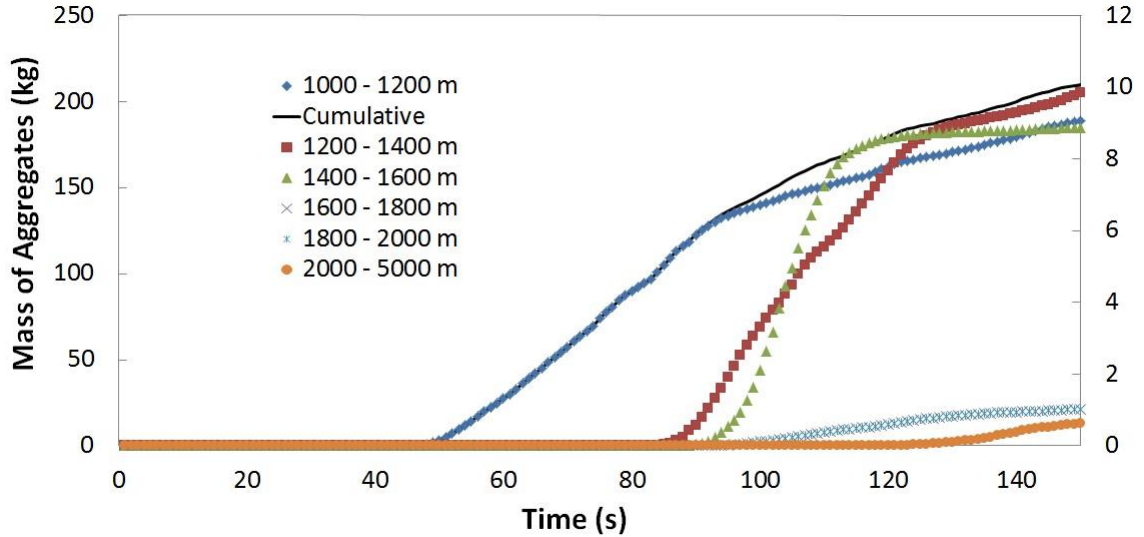


Figure 4.7. The mass of aggregates developing at different altitudes with respect to time. Aggregation between 1000 - 1200 m and the cumulative aggregation are plotted on the left axis. The mass of aggregation taking place at all other altitude levels is on the right axis.

Aggregation rate was considered with respect to both time and particle size. The relative humidity and aggregation rates for the three ash size samples are shown at 150 s. The aggregation rate for the Ash-1 sample at 150 s is shown in Figure 4.8 and the volume fraction of Ash-1 present at this time is shown in Figure 4.11a. Aggregation rates are highest near the ground and lowest along the top and the front edge of the PDC. Higher volume fractions of particles than the plume average are visible near the bottom of the flow (Figure 4.11a) and these regions also correspond to higher rates of aggregation. The coignimbrite plume beginning to form at the front of the flow behaves somewhat differently. The volume fraction of Ash-1 in this region approaches that close to the bed throughout the rest of the flow (Figure 4.11a) but aggregation rates typically remain low (Figure 4.8).

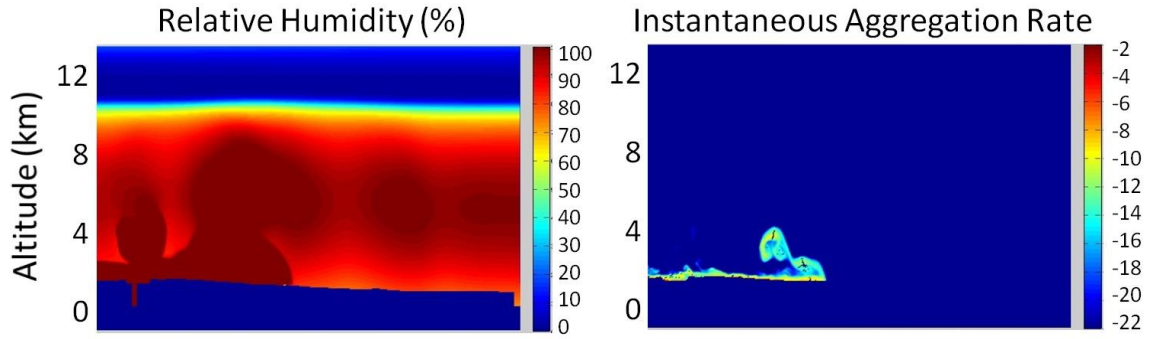


Figure 4.8. A comparison to the relative humidity, with % RH represented on the left color bar, produced by the eruption to the aggregation rate, log scale on the right color bar, of Ash-1 at 150 s after the start of the eruption. The width of the area shown is 14 km.

The instantaneous aggregation rate and volume fraction for the Ash-2 (Figures 4.9 and 4.11b) and Ash-3 (Figures 4.10 and 4.11c) samples, at 150 s into the simulation, show that both samples aggregate most efficiently in the coignimbrite column. Neither sample displays the tendency for enhanced aggregation near the bed that is seen in Ash-1.

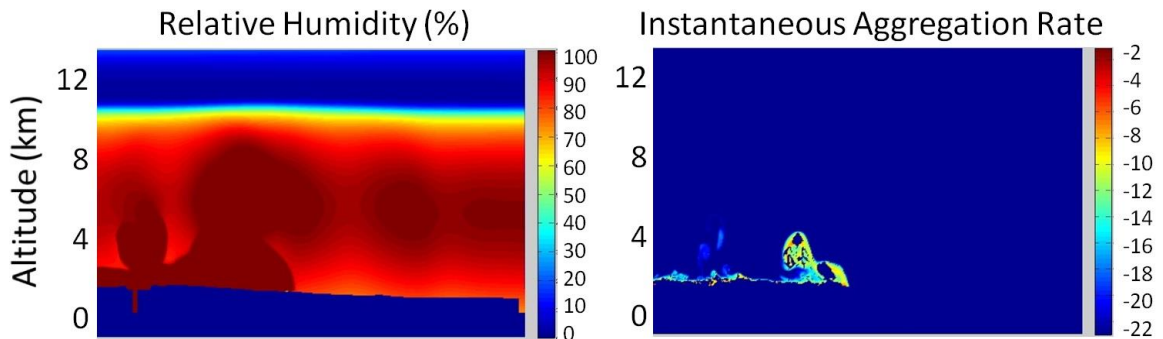


Figure 4.9. A comparison to the relative humidity, with % RH represented on the left color bar, produced by the eruption and the aggregation rate, on the right color bar, of Ash-2 at 150 s after the start of the eruption. The width of the area shown is 14 km.

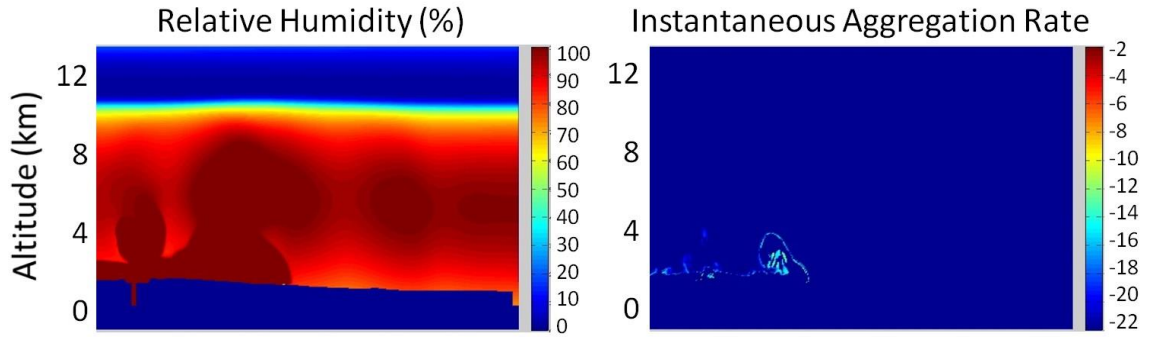


Figure 4.10. A comparison to the relative humidity, with % RH on the left color bar, produced by the eruption and the aggregation rate, on the right color bar, of Ash-3 at 150 s after the start of the eruption. The width of the area shown is 14 km.

The volume fraction of Ash-4 at 150 s is shown in Figure 4.11d. The volume fraction is highest near the ground, where aggregates are forming most efficiently in Ash-1, and in the coignimbrite column, where Ash-2 and Ash-3 are aggregating more efficiently.

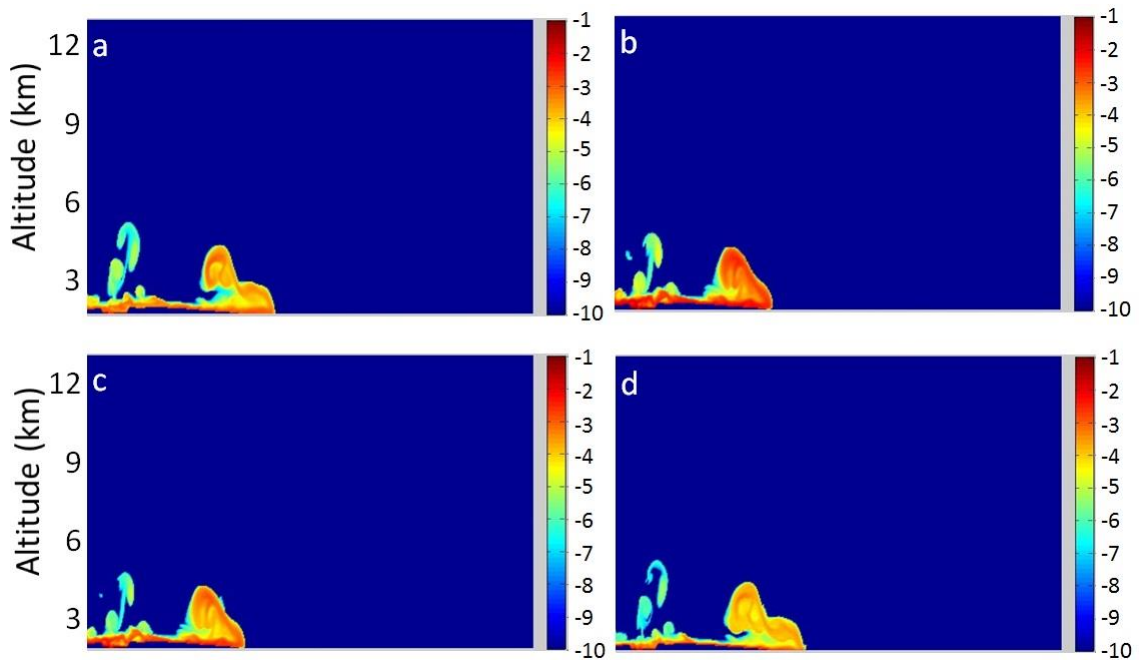


Figure 4.11. The volume fraction of Ash-1 (a), Ash-2 (b), Ash-3 (c) and Ash-4 (d) at 150s into the eruption simulation, plotted on a logarithmic scale.

The behavior of Ash-2 was also examined earlier in the simulation, at 100 s. The early injection of water vapor into the atmosphere, well ahead of the erupted Ash-2, can be seen reaching neutral buoyancy, the point where the eruption column and the atmosphere have roughly the same density, in the atmosphere and has just begun to spread out at 100 s (Figure 4.12). The Ash-2 sample is in the process of being erupted from the volcanic conduit and the material has not yet collapsed to form a PDC. Despite the eruption still being in the jet phase, when the jet density is greater than that of the atmosphere and upward motion is being controlled by the inertial energy of the eruption, aggregation is still occurring in the high volume fraction jet center (Figure 4.12 and 4.13).

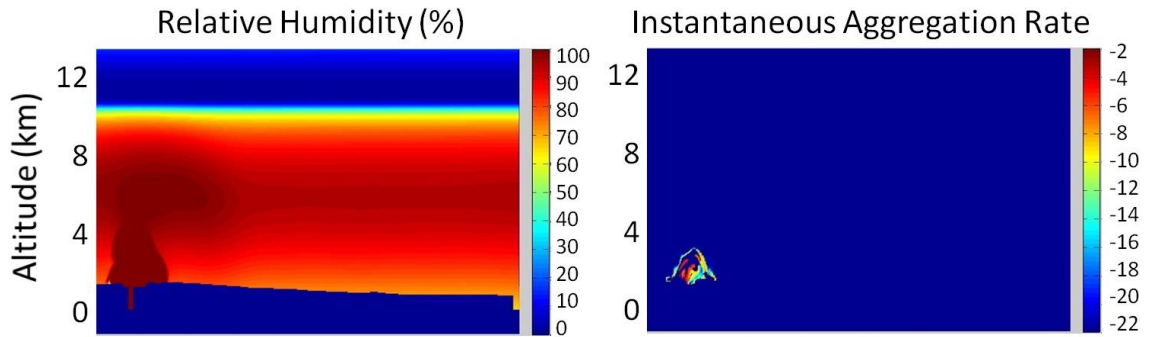


Figure 4.12. A comparison to the relative humidity, with % RH on the left color bar, produced by the eruption and the aggregation rate, on the right color bar, of Ash-2 at 100 s after the start of the eruption. The width of the area shown is 14 km.

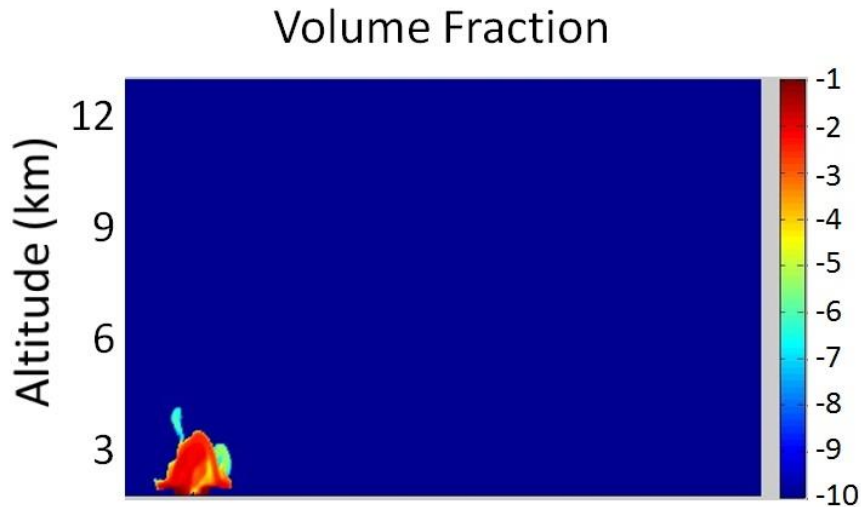


Figure 4.13. The volume fraction, plotted on a logarithmic scale, of Ash-2 present at 100 s into the simulation. The width of the area shown is 14 km.

#### 4.4 Simulation Discussion

Ample water vapor was available during the 1790 eruption of Kilauea volcano due to both the phreatomagmatic nature of the eruption (Mastin, 1997; McPhie et al., 1990; Swanson et al., 2012a) and the high level water vapor typically present in the Hawaiian atmosphere (Figure 4.6). Consequently, the ash sizes examined interact consistently in a high relative humidity environment. Additionally, the PDC resulting from the eruption is saturated for the duration of the trial so most of the ash is likely to be covered with at least a monolayer of water shortly after the start of the eruption. Telling et al. (2013) showed that the ash surface only needs to adsorb enough water for the water layer depth to exceed the porosity of the ash surface, which is typically on the order of nanometers to micrometers (Carter et al., 2009). A subsaturated atmosphere can take around 50 minutes to generate a water layer that is thicker than the ash surface porosity (Telling et al., 2013) but the saturated conditions in the modeled plume would increase

the speed of water layer development. Aggregates are first observed only 50 seconds into the simulation in the jet region and later in the PDC (Figure 4.7).

Ash-2 typically aggregates more efficiently than either Ash-1 or Ash-3. Studies of ash size distribution have shown that there is substantially less ash in the Ash-1 and Ash-3 size ranges than in the Ash-2 range (Gislason et al., 2011; Rose and Durant, 2009). Additionally, the 1790 Kilauea ash is considered to be a particularly fine ash deposit (Personal Correspondence- Larry Mastin and Don Swanson). Collisions involving Ash-3, due to its large size, have higher CKE values, lowering the probability that aggregation will occur (Gilbert and Lane, 1994; Telling and Dufek, 2012; Telling et al., 2013). Additionally, in longer duration simulations, the heavy Ash-3 sample will deposit first and will have the lowest circulation time, reducing the amount of time it is available for aggregation, though these effects are less important in the simulation presented here.

Ash-1, the finest size range of particles, undergoes aggregation throughout more of the flow (Figure 4.8) than Ash-2 (Figure 4.9) but forms measurable aggregates at lower rates. In order for an aggregate to form, it must reach the size limit for lapilli set in Table 4.1. Ash-1, due to its small size, takes significantly longer than Ash-2 or Ash-3 to grow to the size of a lapillus. The smallest size fraction of ash is more likely to travel at higher velocities, closely tracing the fluid motion, particularly near the plume boundaries, than Ash-2 or Ash-3, which results in high CKE collisions and reduces aggregation efficiency. However, a high volume fraction of Ash-1 is present near the bed (Figure 4.11a) and aggregating efficiently in this region (Figure 4.8). The high aggregation rates, particularly in the fine Ash-1 sample, indicate that the collisional frequency is particularly high in this region. Continuing the tale of the three little ash particles, Ash-2

tends to aggregate most efficiently, particularly near the front of the flow. The middle ash size range is abundant throughout the eruption, has a lower mass than Ash-3 and has, overall, less energy than Ash-1, promoting the aggregation efficiency of the sample.

Pyroclastic density currents are high energy flows and aggregates form most efficiently in low CKE collisions, leading to the question of whether PDC's can effectively produce aggregates. However, Branney et al. (2011) and Brown et al. (2010) have both shown that aggregates can form efficiently in some ground hugging flows. This simulation of a possible eruption scenario at Kilauea volcano further confirms that aggregates can, under the right conditions, form very efficiently in PDC's. Over the course of the simulation, aggregates consistently formed most efficiently in the high particle density, low energy regions of the PDC, between the ground and 1200 m, regardless of particle size. Aggregates forming higher in the atmosphere, where the volume fraction was significantly lower, took longer to initiate and account for only 10% of the total aggregate mass at the end of the simulation. The high particle density of ash in PDC's may indeed promote aggregation more than the high energy nature of the flow retards it though further comparison of aggregation in buoyant eruption columns and PDC's is needed.

#### **4.5 Conclusions**

The well preserved deposits of the 1790 Kilauea eruption provide a unique opportunity to compare volcanic modeling of aggregate distributions to field data. The eruption simulation confirmed that aggregates can and do form efficiently in PDC's and can even begin forming in the inertial jet region. Three ash size ranges were tested. The finest ash was found to aggregate in most areas of the flow but never reached the

aggregation efficiency of the mid-sized ash sample, which aggregated very efficiently along the front of the flow and in the coignimbrite column.

Water vapor from both the plume and the atmosphere are important in analyzing plume dynamics and particle interactions. The phreatomagmatic Kilauea 1790 eruption was water rich and likely mixed with an atmosphere close to saturation, which kept the eruption plume from diluting over the course of the simulation presented. Water vapor saturation throughout the eruption significantly decreased the time required for aggregation to initiate from tens of minutes to only tens of seconds.

Further study is necessary to better understand the 1790 eruption of Kilauea volcano. A complete set of numerical simulations should be completed to test the range of depth and overpressure conditions published in the literature. This will refine our understanding of what caused such an uncharacteristically large and explosive eruption of Kilauea volcano.

## **CHAPTER 5**

### **CONCLUSIONS**

Ash aggregation has been shown to be important for plume dynamics and atmospheric dispersal of ash (Stevenson et al., 2012; Taddeucci et al., 2011). However, previous studies, particularly Folch et al. (2010), Folch (2012) and Veitch and Woods (2001), have cited the need for research to examine the microphysics involved in ash aggregation. Folch et al. (2010) concluded that both atmospheric and magmatic water vapor play a role in ash aggregation. Textor et al. (2006b) suggested that atmospheric water vapor exercised little control on aggregation rates; however, Textor et al. (2006b) and Folch et al. (2010) both noted that more experimental data is needed to refine the numerical simulations that they present.

The experiments presented here seek to address this problem of limited experimental data. Over 12,000 particle interactions were recorded and the effect of atmospheric conditions, CKE and residence time was analyzed. The first experiment involved only low residence time interactions, at both low and high relative humidity, where both particles in each collision were moving. Relative humidity was observed to have no effect on the efficiency of aggregation but the important effect that CKE has on aggregation efficiency was isolated. Increasing CKE was found to significantly decrease aggregation efficiency. The earlier results of Gilbert and Lane (1994) observed a decrease in aggregation efficiency with increasing particle diameter, which, when converted to CKE, showed the same trend seen in the results of the first experiment. Probabilistic

relationships relating aggregation efficiency to CKE were determined for use in numerical modeling.

However, the results of the first experiment indicated that atmospheric water vapor has little effect on ash aggregation, as was suggested by Textor et al. (2006b), but the results of Folch (2010) strongly suggested otherwise. The second set of experiments presented here was designed to more thoroughly examine the influence of atmospheric water vapor, pressure and residence time on aggregation efficiency. Instead of examining collisions between two moving ash particles, which could only be reliably tracked for a short duration, collisions between one fixed and moving particle were observed. Fixing an ash sample to a slide prior to the particle-particle collision allowed for a more robust examination of relative humidity and particle residence time.

Aggregation efficiency was still found to decrease with increasing CKE across the range of conditions tested; however, a clear difference in this trend at high relative humidity and high residence time allowed for the definition of wet and dry aggregation regimes. Dry aggregation, due to electrostatic charging at the ash surface, was found to be dominant at low relative humidity and high relative humidity that was not maintained for a long period of time. The efficiency of dry aggregation decays swiftly with increasing CKE. Wet aggregation occurs when a particle has circulated in a high humidity atmosphere long enough to develop a surface water layer thicker than the length scale of the surface roughness. Aggregation efficiency decays more gradually with increasing CKE in this regime resulting in efficiencies that are 20-60% higher than at similar CKE values in the dry aggregation regime. More robust probabilistic relationships were determined, based on a combination of theory and experimental data, to describe

wet and dry aggregation efficiency in terms of the appropriate forces present during each type of collision.

Finally, to test the validity of these relationships, a numerical simulation of the 1790 eruption of Kilauea volcano, HI, is presented. The relationships developed after the second set of experiments were incorporated into a multiphase flow simulation and the eruption parameters were defined based on published estimates in the literature. A range of source depths and overpressures caused by the phreatomagmatic eruption was isolated and one set of source conditions was tested in depth to examine the eruption dynamics. The simulation produced a PDC with the beginning of a coignimbrite column forming by 150 s after the start of the eruption. Three ash size ranges were examined for aggregation potential and the abundant, middle Ash-2 range was found to aggregate most efficiently though the fine Ash-1 range aggregated throughout more of the PDC. The largest size range of ash aggregated least efficiently due to the high values of CKE produced by the heavier ash sample. The wet eruption and high relative humidity atmosphere were both key to maintaining high aggregation rates throughout the eruption because the atmosphere did not readily decrease the water vapor available in the plume during mixing. Finally, the simulation showed that aggregation can occur efficiently in PDC's.

The combination of experiments and simulation presented here are needed to improve our understanding of the impact that microphysical ash interactions have on eruption dynamics. Ash aggregation can alter the deposition patterns of ash in both buoyant eruption columns and pyroclastic density currents. However, past estimates of aggregation efficiency have been poor and the interaction between the ambient atmosphere, as opposed to the volcanic column, and ash has often been neglected

entirely. The experiments presented here on ash aggregation in subsaturated environments have shown that ash can and does aggregate even in these lower water vapor environments and, therefore, is important in both near-plume and distant environments. Experiments, however, cannot provide a complete picture of how ash aggregation affects plume dynamics. Numerical simulations provide a macroscopic view into the effect that these microphysical processes have on plume dynamics. Experimentation, combined with numerical modeling, has significantly improved our understanding of ash aggregation processes. These results can be expanded to model past volcanic activity, predict possible outcomes of future eruptions and even to improve our understanding of planetary environments.

## **CHAPTER 6**

### **FUTURE WORK**

#### **6.1 Ash Dispersal and Aggregation Mechanisms**

Volcanic hazards are widespread, affecting nearly all latitudes, and many volcanoes are in close proximity to population centers, posing a significant hazard (Handbook for Volcanic Risk Management). Aside from the immediate hazard posed by an eruption from PDC's or lava flows, the airborne hazard of ash, fine particulate and gas emissions can be deadly to both humans and animals (Marzano et al., 2010; Prata and Tupper, 2009). Fine ash and gas that is injected into the stratosphere can affect regional and global climate for weeks to years, depending on the size of the eruption (Niemeier et al., 2009; Robock, 2000). However, models of ash transport and settling still fall short of correctly predicting these behaviors and improving our understanding of aggregation mechanisms has been highlighted in numerous publications as one of the most important improvements to modeling efforts (DiMuro et al., 2008; Folch, 2012; Folch et al., 2012).

Aggregation produces larger, heavier particles that are removed more quickly from the atmosphere (Brown et al., 2010; Gilbert and Lane, 1994). The effect of this removal can be seen in field deposits from Mount St. Helens, where the Ritzville bulge has been attributed to the removal of fine ash from the atmosphere through aggregation (Veitch and Woods, 2001), and at Soufriere Volcano, where fine ash was not well sorted moving away from the vent and showed a distribution similar to that seen in disintegrated AL (Brazier et al., 1982). Until recently, many models have neglected aggregation

entirely (Barsotti et al., 2008; Folch et al., 2009) or oversimplified the problem by neglecting atmospheric effects or by determining the degree of aggregation occurring ahead of time (Folch, 2012). Our understanding of ash aggregation mechanisms and their importance has been improved through continued experimentation and improved numerical modeling.

The experiments of Gilbert and Lane (1994) were the first to examine wet aggregation, instead of using a water droplet proxy. However, Gilbert and Lane (1994) collides ash with fixed polystyrene spheres and suspended water droplets, not with other ash particles. The effects of atmospheric conditions on aggregation were not specifically investigated in the study though it was noted that relative humidity was low, 10-15%, during the water droplet experiments and that it could be varied during the experiments with polystyrene spheres but no record of the variation was published. Despite these limitations, Gilbert and Lane (1994) was the first study to define a relationship between ash size and aggregation efficiency.

These studies have answered important questions about aggregation processes. Eruption models of both contemporary and historic eruptions have shown that including aggregation is important to correctly modeling ash fall (Costa et al., 2010; Folch, 2012; Folch et al., 2012; Textor et al., 2006a; Veitch and Woods, 2001) and that atmospheric conditions do have an effect on aggregation rates (Folch et al., 2010; Folch, 2012). Gilbert and lane (1994) first identified the important relationship between particle size and aggregation efficiency and Costa et al. (2010) later used this data to show a further relationship between particle Stokes number and aggregation efficiency. They have also introduced important new questions about exactly what processes drive aggregation

efficiency at the particle scale, what flow regions are most likely to promote aggregation, how to define wet and dry aggregation and which atmospheric conditions are most important to consider in numerical modeling.

Telling and Dufek (2012) and Telling et al. (2013) have provided aggregation rate data for real ash samples across a wide range of conditions. The experiments in Telling and Dufek (2012) allow ash particles to collide with one another but, since ash is only allowed to interact briefly with the environment, the ash is prevented from equilibrating with the surroundings. Despite not collecting sufficient data on ash – atmosphere interactions, Telling and Dufek (2012) confirmed and expanded on the results of Gilbert and Lane (1994). The relationship between particle size, when converted to CKE, and aggregation efficiency observed by Gilbert and Lane (1994) was also observed in Telling and Dufek (2012) (Figure 2.7). Telling et al. (2013) also collided two ash particles, however, one sample was fixed but allowed to equilibrate with the atmosphere for extended time periods and the other sample was mobile but not allowed to interact with the atmosphere for more than a few seconds. These experiments further confirmed the importance of CKE in determining the aggregation efficiency of ash particles. The longer residence times tested in Telling et al. (2013) led to the definition of what is required for wet and dry aggregation to be effective and provided a more nuanced investigation of atmospheric effects on aggregation efficiency. Combining the results of these experiments with the theory of Gollwitzer et al. (2012) furthered our understanding of what microphysical forces need to be considered in each type of aggregation event. The relationships determined through this experimental work have provided new methods to model ash behavior in volcanic eruptions. The modeling work on the 1790 eruption of

Kilauea shows that these relationships can be successfully integrated into a numerical simulation without significantly increasing the computational time required. Still, a number of exciting open questions remain.

- *What is the aggregation efficiency in the collision of two moving particles that have both been allowed to equilibrate with the atmosphere?*
- *Does the atmospheric composition of gasses have an effect on aggregation efficiency?*
- *How much is the required residence time for a wet particle collision reduced by when both particles are allowed to interact with the atmosphere? How much does a supersaturated flow accelerate this effect?*

Investigating aggregation efficiency between two moving particles, both of which have been allowed time to equilibrate with their environment, would be step forward in this type of experimental research. Examining collisions between ash particles is important to further our understanding of the importance that surface chemistry and particle roughness may have in aggregation efficiency. Though, studies done to date, including Delmelle et al. (2005) and Lathem et al. (2011), indicate that chemical composition has a minimal effect on ash behavior. Allowing both particles to equilibrate with the atmosphere before colliding is likely to reduce the residence time required to significantly increase aggregation efficiency as well. Further experimentation would be necessary to determine how much the time may be reduced by and whether the effects may also be seen at lower values of relative humidity. These open questions are key to improving our ability to model volcanic eruptions.

- *What secondary mechanisms may adhere AL more thoroughly, after aggregation has occurred?*
- *What fraction of well developed wet and dry aggregates breaks up after contacting the ground?*
- *How might ambient temperature affect the efficacy of these processes?*

Research on aggregation processes has largely focused on hydrodynamic and electrostatic mechanisms for aggregate formation. However, studies, including Gilbert and Lane (1994) and Textor et al. (2006a), have suggested other primary and secondary mechanisms as well. Bacon and Sarma (1991) have shown that dust aggregates bound by water alone will break up upon contact with the ground and James et al. (2003) have found that this fate is also shared by electrostatic aggregates. However, many volcanic deposits include well preserved aggregates so clearly there are other processes at work in volcanic flows. Gilbert and Lane (1994) suggest that silicate minerals on the surface of ash particles may be partially dissolved by acids condensing from the plume, enhancing the cohesiveness of aggregates. Other minerals, including sodium chloride and calcium sulphate, have also been observed in aggregates (Delmelle et al. (2007); Gilbert and Lane, 1994). The deposition and crystallization of these secondary minerals has been suggested as a bonding mechanism that preserves aggregates through deposition (Tomita et al., 1985; Gilbert and Lane, 1994). Beyond this work isolating what types of minerals may play a role in adhering and preserving ash aggregates, little additional research has been done into where these processes are most effective or what conditions promote these processes.

Gilbert and Lane (1994) cite, in particular, the need for further research into the relationship between temperature and the efficiency of these ash surface processes. At lower temperatures, the water in wet ash aggregates can freeze, altering both the residence time of the aggregate in the atmosphere and the collection properties of the aggregate (Van Eaton et al., 2012b). Experiments conducted by Van Eaton et al. (2012) showed that, once frozen, icy ash aggregates begin to collect fine ash ( $< 31 \mu\text{m}$ ) more efficiently. However, aside from the different collection efficiencies associated with ice aggregates, there are also large scale effects on the plume associated with ice aggregate formation. The latent heat release associated with the formation of ice aggregates heats the plume and increases the buoyancy of the eruption (Van Eaton and Wilson, 2013). This secondary heating often promotes turbulence as well (Van Eaton and Wilson, 2013), which could have an important impact on an area of the volcanic plume in the upper atmosphere that would otherwise be considered a more laminar flow predominantly controlled by atmospheric winds. The amount of water vapor present in an eruption, as well as in the ambient atmosphere, may determine whether the effects of latent heat release need to be considered in eruption modeling and further numerical eruption simulations should be used to explore this forcing. Additionally, research into the composition of ash, other sulfates that may form in volcanic eruptions and glass melting at ash boundaries may improve our understanding of why some eruptions have well preserved aggregates and others do not.

## **6.2 Volcanic Modeling**

Building on the previous modeling (Swanson et al., 2012a) and field work (Mastin, 1997; McPhie et al., 1990; Swanson et al., 2012a) at Kilauea, the modeling

presented here allows us to assess both the validity of the aggregation relationships developed in earlier work and the source of the 1790 eruption of Kilauea. Continuing this modeling work could provide valuable new insights into the eruption. Completing a full suite of numerical simulations to test the range of possible depth and overpressure conditions that may have led to the 1790 eruption of Kilauea volcano is necessary to refine our understanding of the eruption source (Appendix C). Obtaining grain size distributions specific to the Footprints ash layer would refine both the estimates of aggregate size and, possibly, fallout distribution. Due to the unusually fine nature (Personal correspondence, Don Swanson, USGS) of the Footprints ash, which has a mean diameter of less than 60  $\mu\text{m}$ , a laser diffraction particle size analyzer would need to be used, in addition to traditional sieving techniques, to fully analyze the grain size distribution (Van Eaton and Wilson, 2013).

- *Can a comparison of the distribution of aggregates in the field to that produced by a numerical simulation help us to identify the source conditions of the 1790 eruption of Kilauea?*
- *Are aggregates preferentially collecting a certain size range of ash? Can a comparison of ash grain size distribution to aggregate grain size distribution help answer this?*
- *Can models predict the selective aggregation of certain grain sizes?*

A more in depth study of the aggregates themselves would answer important questions about whether any of the aggregates are cored or show layering, which is useful in determining the type of environment they were produced in. Grain size analysis of broken down aggregates from the Footprints ash could be conducted so that the actual

grain size of aggregate material could be compared to that in the modeled aggregates. Determining whether the aggregates are preferentially collecting a certain grain size material, as has been seen in other studies (Brazier et al., 1982), and whether the model can correctly capture this behavior would improve model outputs in future work and provide useful information about systemic bias in the model.

- *What is the mean and minimum grain size of AL in the Kilauea Footprints deposit?*
- *Are models better able to predict the mean or minimum AL distribution than the maximum AL size distribution?*

Further field work should also be conducted at Kilauea to more fully map the distribution of aggregates in the Footprints deposit. The current data focuses on the largest aggregates, resulting in large uncertainties in the average size of aggregates and how they are distributed around the volcano. This type of investigation, when combined with studies from other eruptions, might also help us to identify and model the relationship between aggregate distribution and maximum aggregate size. If a widely applicable model could be produced, it may serve to reduce the computational time needed to incorporate aggregation into volcanic models.

- *How sensitive are other eruption types and locations to aggregation processes?*
- *Which models react most to the addition of these aggregation relationships and why are they more sensitive?*

Lastly, the modeling efforts in this research could be applied to other eruptions and the aggregation relationships developed here could be incorporated into other types of volcanic models. Both types of modeling studies would provide sensitivity data

including where wet and dry aggregation mechanisms are most applicable, which models best represent the aggregate distribution in the field and which types of eruptions are most likely to be impacted by aggregation. Understanding whether one, or both, types of aggregation may be neglected in certain situations could simplify and shorten volcanic modeling requirements in certain areas.

### **6.3 Planetary applications**

- *Can volcanic models that include aggregation be used to estimate atmospheric conditions on Mars during periods of volcanic activity?*

Volcanism is present throughout the solar system and the experiments and modeling done here are applicable beyond Earth. Wilson and Head (2007) modeled volcanic deposits on Mars, incorporating the aggregation relationships in Gilbert and Lane (1994), and estimated a size range for aggregates on Mars. However, the model that they ran used contemporary Martian atmospheric conditions to model eruptions that took place in the Noachian and Hesperian periods, roughly 3000 – 400 million years ago. Reverse modeling to loosely estimate eruption and atmospheric conditions may be possible using the relationships developed here and deposits on Mars that have been identified to include aggregates. This type of reverse modeling is limited by the relatively few constraints that can be placed on Martian aggregate distribution but would provide an interesting point of comparison for future work.

## APPENDIX A

### TABLE OF EXPERIMENT 1 PHYSICAL RUN PARAMETERS

| <i>Date</i> | <i>Sample</i> | <i>Trial ID</i> | <i>Temperature, °C</i> | <i>Relative Humidity, %</i> | <i>Width (m)</i> | <i>Height (m)</i> | <i>Spatial Resolution (µm/pix)</i> | <i>Frame Rate (per s)</i> | <i>No. of Particles</i> |
|-------------|---------------|-----------------|------------------------|-----------------------------|------------------|-------------------|------------------------------------|---------------------------|-------------------------|
| 7-Dec-09    | Ballotini     | 1               | 20.6                   | 26.3                        | 0.036            | 0.038             | 141x148                            | 2000                      | 111113                  |
|             |               | 2               | 20.6                   | 26.3                        |                  |                   |                                    | 2000                      | 36425                   |
|             |               | 3               | 21.3                   | 73.3                        |                  |                   |                                    | 2000                      | 5698                    |
|             |               | 4               | 21.0                   | 61.6                        |                  |                   |                                    | 2000                      | 51697                   |
|             |               | 5a              | 21.2                   | 70.5                        |                  |                   |                                    | 2000                      | 19791                   |
|             |               | 5b              | 21.2                   | 70.5                        |                  |                   |                                    | 2000                      | 14422                   |
| 18-Jan-10   | Ballotini     | 1               | 20.4                   | 38.6                        | 0.042            | 0.045             | 164x176                            | 3000                      | 3725                    |
|             |               | 2               | 20.4                   | 38.5                        |                  |                   |                                    | 3000                      | 1358                    |
|             |               | 3               | 20.4                   | 37.7                        |                  |                   |                                    | 3000                      | 622                     |
|             |               | 4               | 20.4                   | 38.5                        |                  |                   |                                    | 2801                      | 3319                    |
|             |               | 5               | 20.5                   | 36.7                        |                  |                   |                                    | 2900                      | 5353                    |
|             |               | 6a              | 20.6                   | 54.6                        |                  |                   |                                    | 2900                      | 8798                    |
|             |               | 6b              | 20.6                   | 54.6                        |                  |                   |                                    | 2900                      | 10088                   |
|             |               | 7               | 20.6                   | 59.0                        |                  |                   |                                    | 2900                      | 12742                   |
|             |               | 8               | 20.5                   | 59.9                        |                  |                   |                                    | 2900                      | 31633                   |
|             |               | 9a              | 20.5                   | 65.9                        |                  |                   |                                    | 2900                      | 12353                   |
| 9b          | 20.5          | 65.9            |                        |                             |                  | 2900              | 23571                              |                           |                         |
|             |               | 10              | 20.6                   | 75.3                        |                  |                   |                                    | 2900                      | 8224                    |
| 25-Jan-10   | Ballotini     | 1a              | 19.6                   | 34.1                        | 0.045            | 0.044             | 176x172                            | 2000                      | 1943                    |
|             |               | 1b              | 19.6                   | 34.1                        |                  |                   |                                    | 2000                      | 1943                    |
|             |               | 3a              | 19.7                   | 31.5                        |                  |                   |                                    | 2801                      | 4140                    |
|             |               | 3b              | 19.7                   | 31.5                        |                  |                   |                                    | 2801                      | 2344                    |

| <i>Date</i> | <i>Sample</i> | <i>Trial ID</i> | <i>Temperature, °C</i> | <i>Relative Humidity, %</i> | <i>Width (m)</i> | <i>Height (m)</i> | <i>Spatial Resolution (µm/pix)</i> | <i>Frame Rate (per s)</i> | <i>No. of Particles</i> |
|-------------|---------------|-----------------|------------------------|-----------------------------|------------------|-------------------|------------------------------------|---------------------------|-------------------------|
| 25-Jan-10   |               | 4               | 20.2                   | 66.1                        |                  |                   |                                    | 2801                      | 6520                    |
|             |               | 5a              | 20.1                   | 66.2                        |                  |                   |                                    | 2900                      | 3697                    |
|             |               | 5b              | 20.1                   | 66.2                        |                  |                   |                                    | 2900                      | 3407                    |
|             |               | 6               | 20.1                   | 66.8                        |                  |                   |                                    | 2900                      | 1447                    |
|             |               | 7               | 20.1                   | 72.4                        |                  |                   |                                    | 2900                      | 1500                    |
|             |               | 8               | 20.1                   | 74.3                        |                  |                   |                                    | 3000                      | 2258                    |
|             |               | 9a              | 20.1                   | 75.7                        |                  |                   |                                    | 2900                      | 6637                    |
|             |               | 9b              | 20.1                   | 75.7                        |                  |                   |                                    | 2900                      | 17312                   |
|             |               | 10a             | 20.1                   | 70.3                        |                  |                   |                                    | 2900                      | 3087                    |
|             |               | 10b             | 20.1                   | 70.3                        |                  |                   |                                    | 2900                      | 5889                    |
| 1-Feb-10    | Ash           | 3a              | 20.9                   | 23.1                        | 0.045            | 0.044             | 176x172                            | 1800                      | 864                     |
|             |               | 3b              | 20.9                   | 23.1                        |                  |                   |                                    | 1800                      | 1517                    |
|             |               | 4b              | 21.0                   | 23.2                        |                  |                   |                                    | 1800                      | 1418                    |
|             |               | 5b              | 21.0                   | 23.5                        |                  |                   |                                    | 1800                      | 2376                    |
|             |               | 6b              | 21.1                   | 23.6                        |                  |                   |                                    | 1800                      | 2634                    |
|             |               | 7               | 21.1                   | 23.8                        |                  |                   |                                    | 1800                      | 809                     |
|             |               | 8b              | 21.4                   | 47.2                        |                  |                   |                                    | 1800                      | 1697                    |
|             |               | 9               | 21.6                   | 53.7                        |                  |                   |                                    | 1800                      | 3443                    |
| 3-Feb-10    | Ash           | 2a              | 20.4                   | 25.7                        | 0.045            | 0.044             | 176x172                            | 2400                      | 3092                    |
|             |               | 3a              | 20.5                   | 26.4                        |                  |                   |                                    | 2200                      | 1604                    |
|             |               | 4a              | 20.6                   | 26.3                        |                  |                   |                                    | 2000                      | 9184                    |
|             |               | 5a              | 21.2                   | 59.5                        |                  |                   |                                    | 2000                      | 1791                    |
|             |               | 6a              | 21.2                   | 62.8                        |                  |                   |                                    | 1800                      | 9347                    |
|             |               | 6b              | 21.2                   | 62.8                        |                  |                   |                                    | 1800                      | 29348                   |
|             |               | 6c              | 21.2                   | 62.8                        |                  |                   |                                    | 1800                      | 20239                   |
|             |               | 6d              | 21.2                   | 62.8                        |                  |                   |                                    | 1800                      | 14758                   |
|             |               | 7b              | 21.1                   | 64.5                        |                  |                   |                                    | 1800                      | 17477                   |
|             |               | 7c              | 21.1                   | 64.5                        |                  |                   |                                    | 1800                      | 10860                   |
|             |               | 8a              | 21.0                   | 62.1                        |                  |                   |                                    | 1800                      | 5582                    |

| <i>Date</i> | <i>Sample</i> | <i>Trial ID</i> | <i>Temperature, °C</i> | <i>Relative Humidity, %</i> | <i>Width (m)</i> | <i>Height (m)</i> | <i>Spatial Resolution (µm/pix)</i> | <i>Frame Rate (per s)</i> | <i>No. of Particles</i> |
|-------------|---------------|-----------------|------------------------|-----------------------------|------------------|-------------------|------------------------------------|---------------------------|-------------------------|
| 3-Feb-10    |               | 8b              | 21.0                   | 62.1                        |                  |                   |                                    | 1800                      | 19701                   |
|             |               | 8c              | 21.0                   | 62.1                        |                  |                   |                                    | 1800                      | 21688                   |
| 22-Feb-10   | Ash           | 5               | 20.9                   | 43.5                        | 0.045            | 0.044             | 176x172                            | 2000                      | 2062                    |

## APPENDIX B

### TABLE OF EXPERIMENT 2 PHYSICAL RUN PARAMETERS

| Date      | Run No. | Sample Type | Resolution ( $\mu\text{m}/\text{pix}$ ) | T ( $^{\circ}\text{C}$ ) | RH (%) | P (kPa) | t (min) |
|-----------|---------|-------------|---|--------------------------|--------|---------|---------|
| 2/1/2012  | 1       | SiO2        | 42                                      | 21.2                     | 34.9   | 101.4   | 10      |
| 2/1/2012  | 2       | SiO2        | 42                                      | 21.6                     | 34.4   | 101.4   | 20      |
| 2/1/2012  | 3       | SiO2        | 42                                      | 22.1                     | 34.0   | 101.4   | 30      |
| 2/1/2012  | 4       | SiO2        | 42                                      | 22.5                     | 33.6   | 101.4   | 40      |
| 2/1/2012  | 5       | SiO2        | 42                                      | 22.8                     | 32.9   | 101.4   | 50      |
| 2/1/2012  | 6       | SiO2        | 42                                      | 22.8                     | 29.0   | 101.4   | 60      |
| 2/1/2012  | 7       | SiO2        | 42                                      | 23.0                     | 31.0   | 101.4   | 70      |
| 2/1/2012  | 8       | SiO2        | 42                                      | 23.0                     | 28.4   | 101.4   | 80      |
| 2/1/2012  | 9       | SiO2        | 42                                      | 23.5                     | 29.9   | 101.4   | 90      |
| 2/13/2012 | 1       | SiO2        | 56                                      | 23.5                     | 71.5   | 102.7   | -       |
| 2/13/2012 | 2       | SiO2        | 56                                      | 24.1                     | 76.1   | 102.7   | -       |
| 2/13/2012 | 3       | SiO2        | 56                                      | 24.4                     | 80.0   | 102.7   | -       |
| 2/13/2012 | 4       | SiO2        | 56                                      | 24.5                     | 85.5   | 102.7   | -       |
| 2/13/2012 | 5       | SiO2        | 56                                      | 24.6                     | 86.4   | 102.7   | -       |
| 2/24/2012 | 1       | SiO2        | 65                                      | 21.1                     | 90.0   | 18.4    | 1       |
| 2/24/2012 | 2       | SiO2        | 65                                      | 21.3                     | 91.3   | 38.7    | 11      |
| 2/24/2012 | 3       | SiO2        | 65                                      | 21.6                     | 90.8   | 50.6    | 15      |
| 2/24/2012 | 4       | SiO2        | 65                                      | 23.1                     | 87.3   | 30.2    | 20      |
| 2/24/2012 | 5       | SiO2        | 65                                      | 23.3                     | 81.2   | 21.8    | 30      |
| 2/24/2012 | 6       | SiO2        | 65                                      | 24.5                     | 79.5   | 24.1    | 35      |
| 2/24/2012 | 7       | SiO2        | 65                                      | 24.6                     | 82.5   | 38.7    | 40      |
| 2/24/2012 | 8       | SiO2        | 65                                      | 24.7                     | 83.0   | 56.0    | 45      |
| 2/24/2012 | 9       | SiO2        | 65                                      | 22.4                     | 76.4   | 16.7    | 47      |
| 2/24/2012 | 10      | SiO2        | 65                                      | 22.6                     | 85.6   | 24.8    | 49      |
| 2/24/2012 | 11      | SiO2        | 65                                      | 22.9                     | 87.3   | 42.8    | 55      |
| 3/5/2012  | 1       | MSH         | 55                                      | 22.1                     | 20.8   | 98.9    | 10      |
| 3/5/2012  | 2       | MSH         | 55                                      | 22.5                     | 23.3   | 99.0    | 15      |
| 3/5/2012  | 3       | MSH         | 55                                      | 22.7                     | 24.2   | 99.0    | 20      |
| 3/5/2012  | 4       | MSH         | 55                                      | 23.0                     | 24.8   | 99.0    | 25      |
| 3/5/2012  | 5       | MSH         | 55                                      | 23.2                     | 25.1   | 99.0    | 30      |
| 3/5/2012  | 6       | MSH         | 55                                      | 23.5                     | 15.2   | 24.4    | 31      |
| 3/5/2012  | 7       | MSH         | 55                                      | 23.6                     | 19.9   | 60.0    | 35      |
| 3/5/2012  | 8       | MSH         | 55                                      | 24.0                     | 13.4   | 12.6    | 36      |
| 3/5/2012  | 9       | MSH         | 55                                      | 24.3                     | 11.5   | 14.3    | 37      |

| Date      | Run No. | Sample Type | Resolution ( $\mu\text{m}/\text{pix}$ ) | T ( $^{\circ}\text{C}$ ) | RH (%) | P (kPa) | t (min) |
|-----------|---------|-------------|---|--------------------------|--------|---------|---------|
| 3/5/2012  | 10      | MSH         | 55                                      | 24.4                     | 16.2   | 36.3    | 45      |
| 3/5/2012  | 11      | MSH         | 55                                      | 24.6                     | 17.6   | 65.1    | 60      |
| 3/5/2012  | 12      | MSH         | 55                                      | 24.8                     | 18.3   | 82.1    | 80      |
| 3/5/2012  | 13      | MSH         | 55                                      | 24.9                     | 12.7   | 12.6    | 81      |
| 3/5/2012  | 14      | MSH         | 55                                      | 25.0                     | 15.9   | 29.5    | 87      |
| 3/5/2012  | 15      | MSH         | 55                                      | 25.1                     | 16.9   | 43.1    | 99      |
| 3/9/2012  | 1       | MSH         | 55                                      | 17.6                     | 89.5   | 102.5   | 20      |
| 3/9/2012  | 2       | MSH         | 55                                      | 18.1                     | 90.5   | 102.5   | 35      |
| 3/9/2012  | 3       | MSH         | 55                                      | 18.4                     | 90.9   | 102.5   | 45      |
| 3/9/2012  | 4       | MSH         | 55                                      | 18.4                     | 91.4   | 102.5   | 60      |
| 3/9/2012  | 5       | MSH         | 55                                      | 19.0                     | 92.3   | 102.5   | 80      |
| 3/9/2012  | 6       | MSH         | 55                                      | 19.8                     | 92.7   | 102.5   | 100     |
| 4/16/2012 | 1       | Tu          | 44                                      | 18.3                     | 60.6   | 99.0    | 10      |
| 4/16/2012 | 2       | Tu          | 44                                      | 19.2                     | 54.2   | 99.0    | 20      |
| 4/16/2012 | 3       | Tu          | 44                                      | 19.6                     | 54.0   | 99.0    | 30      |
| 4/16/2012 | 4       | Tu          | 44                                      | 20.0                     | 54.1   | 99.0    | 40      |
| 4/16/2012 | 5       | Tu          | 44                                      | 20.4                     | 54.1   | 99.0    | 50      |
| 4/16/2012 | 6       | Tu          | 44                                      | 20.5                     | 36.1   | 14.2    | 60      |
| 4/16/2012 | 7       | Tu          | 44                                      | 21.1                     | 45.0   | 31.2    | 70      |
| 4/16/2012 | 8       | Tu          | 44                                      | 21.5                     | 47.2   | 48.1    | 80      |
| 4/16/2012 | 9       | Tu          | 44                                      | 21.7                     | 48.4   | 60.0    | 90      |
| 4/16/2012 | 10      | Tu          | 44                                      | 22.1                     | 49.6   | 77.0    | 100     |
| 4/18/2012 | 1       | Tu          | 42                                      | 20.9                     | 90.9   | 98.5    | 70      |
| 4/18/2012 | 2       | Tu          | 42                                      | 21.1                     | 91.4   | 98.5    | 76      |
| 4/18/2012 | 3       | Tu          | 42                                      | 21.5                     | 91.8   | 98.5    | 83      |
| 4/18/2012 | 5       | Tu          | 42                                      | 22.2                     | 92.2   | 98.5    | 95      |
| 4/18/2012 | 6       | Tu          | 42                                      | 22.5                     | 92.2   | 98.5    | 99      |
| 4/18/2012 | 7       | Tu          | 42                                      | 23.1                     | 91.1   | 15.5    | 120     |
| 4/18/2012 | 8       | Tu          | 42                                      | 23.3                     | 92.6   | 25.7    | 124     |
| 4/18/2012 | 9       | Tu          | 42                                      | 23.5                     | 92.9   | 34.1    | 130     |
| 4/18/2012 | 10      | Tu          | 42                                      | 23.7                     | 93.0   | 42.6    | 135     |
| 4/18/2012 | 11      | Tu          | 42                                      | 24.1                     | 92.8   | 54.5    | 140     |
| 4/18/2012 | 12      | Tu          | 42                                      | 24.3                     | 92.6   | 63.0    | 145     |
| 4/18/2012 | 13      | Tu          | 42                                      | 24.6                     | 92.3   | 73.1    | 151     |
| 4/25/2012 | 1       | Tu          | 41                                      | 19.3                     | 93.4   | 13.4    | 30      |
| 4/25/2012 | 2       | Tu          | 41                                      | 19.5                     | 94.2   | 13.4    | 40      |
| 4/25/2012 | 3       | Tu          | 41                                      | 20.1                     | 93.9   | 13.4    | 47      |
| 4/25/2012 | 4       | Tu          | 41                                      | 20.7                     | 94.2   | 21.8    | 55      |
| 4/25/2012 | 5       | Tu          | 41                                      | 21.3                     | 94.0   | 28.6    | 60      |
| 4/25/2012 | 6       | Tu          | 41                                      | 21.7                     | 93.8   | 35.4    | 65      |

| Date      | Run No. | Sample Type      | Resolution ( $\mu\text{m}/\text{pix}$ ) | T ( $^{\circ}\text{C}$ ) | RH (%) | P (kPa) | t (min) |
|-----------|---------|------------------|---|--------------------------|--------|---------|---------|
| 4/25/2012 | 7       | Tu               | 41                                      | 22.1                     | 93.6   | 42.2    | 70      |
| 4/25/2012 | 8       | Tu               | 41                                      | 22.4                     | 93.4   | 47.3    | 75      |
| 8/20/2012 | 1       | MSH              | 41                                      | 19.6                     | 91.4   | 100.9   | 75      |
| 8/20/2012 | 2       | MSH              | 41                                      | 19.8                     | 92.6   | 100.9   | 82      |
| 8/20/2012 | 3       | MSH              | 41                                      | 20.0                     | 93.0   | 100.9   | 90      |
| 8/20/2012 | 4       | MSH              | 41                                      | 20.2                     | 94.2   | 23.0    | 95      |
| 8/20/2012 | 5       | MSH              | 41                                      | 20.8                     | 94.9   | 65.3    | 100     |
| 8/20/2012 | 6       | MSH              | 41                                      | 21.2                     | 94.5   | 84.0    | 105     |
| 8/20/2012 | 7       | MSH              | 41                                      | 20.7                     | 94.0   | 100.9   | 150     |
| 8/21/2012 | 1       | SiO <sub>2</sub> | 44                                      | 21.1                     | 90.5   | 101.1   | 75      |
| 8/21/2012 | 2       | SiO <sub>2</sub> | 44                                      | 21.6                     | 92.5   | 101.1   | 90      |
| 8/21/2012 | 3       | SiO <sub>2</sub> | 44                                      | 22.1                     | 93.2   | 101.1   | 95      |
| 8/21/2012 | 4       | SiO <sub>2</sub> | 44                                      | 22.8                     | 93.0   | 16.3    | 100     |
| 8/21/2012 | 5       | SiO <sub>2</sub> | 44                                      | 23.7                     | 94.4   | 35.0    | 110     |
| 8/21/2012 | 6       | SiO <sub>2</sub> | 44                                      | 24.4                     | 94.2   | 50.2    | 115     |
| 9/4/2012  | 1       | MSH              | 40                                      | 20.2                     | 92.6   | 100.9   | 90      |
| 9/4/2012  | 2       | MSH              | 40                                      | 20.5                     | 92.7   | 100.9   | 92      |
| 9/4/2012  | 3       | MSH              | 40                                      | 20.4                     | 93.4   | 17.9    | 100     |
| 9/4/2012  | 4       | MSH              | 40                                      | 20.7                     | 94.5   | 23.0    | 115     |
| 9/4/2012  | 5       | MSH              | 40                                      | 21.0                     | 94.8   | 29.7    | 120     |
| 9/4/2012  | 6       | MSH              | 40                                      | 21.2                     | 94.8   | 33.1    | 125     |
| 9/4/2012  | 7       | MSH              | 40                                      | 21.9                     | 94.8   | 50.1    | 130     |
| 9/4/2012  | 8       | MSH              | 40                                      | 22.2                     | 93.9   | 67.0    | 155     |

## APPENDIX C

### RANGE OF ERUPTIVE CONDITIONS AT KILAUEA VOLCANO

| Run ID | Depth (m) | Pressure (MPa) |
|--------|-----------|----------------|
| 1      | 400       | 10             |
| 2      | 400       | 20             |
| 3      | 400       | 30             |
| 4      | 500       | 10             |
| 5      | 500       | 20             |
| 6      | 500       | 30             |
| 7      | 600       | 10             |
| 8      | 600       | 20             |
| 9      | 600       | 30             |
| 10     | 700       | 10             |
| 11     | 700       | 20             |
| 12     | 700       | 30             |

## REFERENCES

- Aanen, L. (2002), Measurements of turbulent scalar mixing by means of a combination of PIV and LIF, Delft University Press, Netherlands.
- Bacon, D.P. and R.A. Sarma (1991), Agglomeration of dust in convective clouds initialized by nuclear bursts, *Atmospheric Environment Part A- General Topics*, 25, 2627-2642, doi: 10.1016/0960-1686(91)90180-F.
- Barsotti, S., A. Neri, J. Scire (2008), The VOL-CALPUFF model for atmospheric ash dispersal: 1. Approach and physical formulation, *Journal of Geophysical Research*, 113, doi:10.1029/2006JB004623.
- Beard, K.V., Durkee, R.I., and Ochs, H.T. (2002), Coalescence efficiency measurements for minimally charged cloud drops, *Journal of the Atmospheric Sciences*, 59,233-243.
- Beard, K.V., Ochs, H.T., and Liu, S. (2001), Collisions between small precipitation drops. Part III: Laboratory measurements at reduced pressure, *Journal of the Atmospheric Sciences*, 58:1395-1408.
- Beard, K.V., Ochs, H.T., and Tung, T.S., 1979. "A measurement of the efficiency for collection between cloud drops." *Journal of the Atmospheric Sciences*, 36:2478-2483.
- Brand, B.D. and C.M. White (2007), Origin and stratigraphy of phreatomagmatic deposits at the Pleistocene Sinker Butte Volcano, Western Snake River Plain, Idaho, *Journal of Volcanology and Geothermal Research*, 160, 319-339, doi: 10.1016/j.jvolgeores.2006.10.007.
- Branney, M.J. and R.J. Brown (2011), Impactoclastic density current emplacement of terrestrial meteorite-impact ejecta and the formation of dust pellets and accretionary lapilli: Evidence from Stac Fada, Scotland, *The Journal of Geology*, 119(3), 275-292, doi: 10.1086/659147.
- Brazier, S., Davis, A., Sigurdsson, H. and Sparks, R. (1982), Fall-out and deposition of volcanic ash during the 1979 explosive eruption of the Soufriere of St. Vincent, *Journal of Volcanology and Geothermal Research*, 14,335-359.
- Brazier-Smith, P.R., Jennings, S.G. and Latham, J. (1972), The interaction of falling water drops: coalescence, *Proc. R. Soc. London*, 326,393-408.
- Brown, R.J., M.J. Branney, C. Maher, and P. Dávila-Harris (2010), Origin of accretionary lapilli within ground-hugging density currents: Evidence from

- pyroclastic couplets on Tenerife, *GSA Bulletin*, 122, 305-320, doi: 10.1130/B26449.1.
- Burgisser, A., Bergantz, G. and Breidenthal, R. (2005), Addressing complexity in laboratory experiments: the scaling of dilute multiphase flows in magmatic systems, *Journal of Volcanology and Geothermal Research*, 141, 245-265.
- Bursik, M.L. and A.W. Woods (1996), The dynamics and thermodynamics of large ash flows, *Bulletin of Volcanology*, 58, 175-193, doi: 10.1007/s004450050134.
- Carey, S.N. and H. Sigurdsson (1982), Influence of particle aggregation on deposition of distal tephra from the May 18, 1980, eruption of Mount St. Helens Volcano, *Journal of Geophysical Research*, 87, 7061-7062, doi: 10.1029/JB087iB08p07061.
- Carrigan, C.R. (2000), Plumbing systems, In: Sigurdsson, H. (ed) *Encyclopedia of Volcanoes*, Academic Press, San Diego, 421-430.
- Carshaw, K.S., O. Boucher, D.V. Spracklen, G.W. Mann, J.G.L. Rae, S. Woodward, and M. Kulmala (2009), Atmospheric aerosols in the earth system: a review of interactions and feedbacks, *Atmos. Chem. Phys.*, 9, 11087-11183.
- Carter, A., M.S. Ramsey, A.J. Durant, I.P. Skilling, and A. Wolfe (2009), Micron-scale roughness of volcanic surfaces from thermal infrared spectroscopy and scanning electron microscopy, *Journal of Geophysical Research*, 114, doi:10.1029/2008JB005632.
- Costa, A., A. Folch and G. Macedonio (2010), A model for wet aggregation of ash particles in volcanic plumes and clouds: 1. Theoretical formulation, *Journal of Geophysical Research*, 115, doi: 10.1029/2009JB007175.
- Davis, R.H., J. Serayssol, and E.J. Hinch (1986), The elastohydrodynamic collision of two spheres, *Journal of Fluid Mechanics*, 163, 479-497.
- Delmelle, P., F. Villi ras, and M. Pelletier (2005), Surface area, porosity and water adsorption properties of fine volcanic ash particles, *Bulletin of Volcanology*, 67, 160-169, doi: 10.1007/s00445-004-0370-x.
- Delmelle, P., M. Lambert, Y. Dufr ne, P. Gerin, and N.  skarsson (2007), Gas/aerosol-ash interaction in volcanic plumes: New insights from surface analyses of fine ash particles, *Earth and Planetary Science Letters*, 259, 159-170, doi:10.1016/j.epsl.2007.04.052.
- Dibble, S. (1843), *A History of the Sandwich Islands*, p. 451, T.G. Thrum, Lahainaluna, Hawaii.

- DiMuro, A., M. Rosi, E. Aguilera, R. Barbieri, G. Massa, F. Mundula, and F. Pieri (2008), Transport and sedimentation dynamics of transitional explosive eruption columns: The example of the 800 BP Quilotoa plinian eruption (Ecuador), *Journal of Volcanology and Geothermal Research*, *174*, 307-324, doi: 10.1016/j.jvolgeores.2008.03.002.
- Dufek, J. and G.W. Bergantz (2007), Suspended load and bed-load transport of particle-laden gravity currents: the role of particle-bed interaction, *Theoretical and Computational Fluid Dynamics*, *21*, 119-145, doi: 10.1007/s00162-007-0041-6.
- Dufek, J. and M. Manga (2008), In situ production of ash in pyroclastic flows, *Journal of Geophysical Research- Solid Earth*, *113*, doi:10.1029/2007JB005555.
- Dufek, J., J. Wexler and M. Manga (2009), Transport capacity of pyroclastic density currents: Experiments and models of substrate-flow interaction, *Journal of Geophysical Research- Solid Earth*, *114*, doi:10.1029/2008JB006216.
- Ersoy, O. (2010), Surface area and volume measurements of volcanic ash particles by SEM stereoscopic imaging, *Journal of Volcanology and Geothermal Research*, *190*, 290-296, doi:10.1016/j.jvolgeores.2009.12.006.
- Folch, A., A. Costa, and G. Macedonio (2009), Fall3D: A computational model for transport and deposition of volcanic ash, *Computers and Geosciences*, *35*, 1334-1342.
- Folch, A., A. Costa, A. Durant, and G. Macedonio (2010), A model for wet aggregation of ash particles in volcanic plumes and clouds: 2. Model application, *Journal of Geophysical Research*, *115*, 96-115, doi:10.1029/2009JB007176.
- Folch, A. (2012), A review of tephra transport and dispersal models: Evolution, current status, and future perspectives, *Journal of Volcanology and Geothermal Research*, *235*, 96-115, doi: 10.1016/j.jvolgeores.2012.05.020.
- Folch, A., A. Costa, and S. Basart (2012), Validation of the FALL3D ash dispersion model using observations of the 2010 Eyjafjallajökull volcanic ash clouds, *Atmospheric Environment*, *48*, 165-183, doi: 10.1016/j.atmosenv.2011.06.072.
- Gilbert, J.S., S.J. Lane, R.S.J. Sparks, and T. Koyaguchi (1991), Charge Measurements on Particle Fallout from Volcanic Plume, *Nature*, *349*, 598-600, doi: 10.1038/349598a0.
- Gilbert, J.S., and S.J. Lane (1994), The Origin of Accretionary Lapilli, *Bulletin of Volcanology*, *56*, 398-411, doi:10.1007/BF00326465.
- Gislason, S.R., T. Hassenkam, S. Nedel, N. Bovet, E.S. Eiriksdottir, H.A. Alfredsson, C.P. Hem, Z.I. Balogh, K. Dideriksen, N. Oskarsson, B. Sigfusson, G. Larsen, and

- S.L.S. Stipp (2011), Characterization of Eyjafjallajökull volcanic ash particles and a protocol for rapid risk assessment, *Proceedings of the National Academy of Sciences of the USA*, 108, 7307-7312, doi: 10.1073/pnas.1015053108.
- Glickman, T. (2000), American Meteorological Association: Glossary of Meteorology, Second Edition, American Meteorological Association, Cambridge, MA.
- Gollwitzer, F., I. Rehberg, C.A. Kruehle, and K. Huang (2012), Coefficient of restitution for wet particles, *Physical Review E*, 86, doi: 10.1103/PhysRevE.86.011303.
- Hall, M.L., C. Robin, B. Beate, P. Mothes, and M. Monzier (1999), Tungurahua Volcano, Ecuador: structure, eruptive history and hazards, *Journal of Volcanology and Geothermal Research*, 91, 1-21, doi: 10.1016/s0377-0273(99)00047-5.
- Handbook for Volcanic Risk Management: Prevention, Crisis Management, Resilience. MIAVITA Team, Orleans, 2012.
- Ilyinskaya, E., V.I. Tsanev, R.S. Martin, C. Oppenheimer, J. Le Blond, G. M. Sawyer, and M.T. Gudmundsson (2011), Near-source observations of aerosol size distributions in the eruptive plumes from Eyjafjallajökull volcano, March-April 2012, *Atmospheric Environment*, 45, 3210-3216, doi: 10.1016/j.atmosenv.2011.03.017.
- Jaggard, T.A. (1921), Fossil Human Footprints in Kau Desert, Hawaii, *Volcano Obs. Mon. Bull.*, 9, 114-118.
- James, M.R., J.S. Gilbert, and S.J. Lane (2002), Experimental investigation of volcanic particle aggregation in the absence of a liquid phase, *Journal of Geophysical Research*, 107(B9), doi: 10.1029/2001JB000950.
- James, M.R., S.J. Lane, and J.S. Gilbert (2003), Density, construction, and drag coefficient of electrostatic volcanic ash aggregates, *Journal of Geophysical Research –Solid Earth*, 108(B9), doi: 10.1029/2002JB002011.
- Latham, T.L., P. Kumar, A. Nenes, J. Dufek, I. Sokolik, M. Trail, A. Russell, and S. Clarke (2011), The hygroscopic properties of volcanic ash, *Geophysical Research Letters*, 38, doi: 10.1029/2011GL047298.
- Lautze, N.C., J. Taddeucci, D. Andronico, C. Cannata, L. Tornetta, P. Scarlato, B. Houghton, M.D. Lo Castro (2012), SEM-based methods for the analysis of basaltic ash from weak explosive activity at Etna in 2006 and the 2007 eruptive crisis at Stromboli, *Physics and Chemistry of the Earth*, 45-46, 113-127, doi: 10.1016/j.pce.2011.02.001.
- Low, T.B., and R. List (1982), Collision, Coalescence and Breakup of Raindrops. Part 1. Experimentally Established Coalescence Efficiencies and Fragment Size

- Distribution in Breakup, *Journal of Atmospheric Sciences*, 39, 1591-1606, doi: 10.1175/1520-0469.
- Marshall, J.R., T.B. Sauke, and J.N. Cuzzi (2005), Microgravity studies of aggregation in particulate clouds, *Geophysical Research Letters*, 32, doi: 10.1029/2005GL022567.
- Marzano, F., Barbieri, S., Picciotti, E. and Karlsdóttir, S., 2010. "Monitoring subglacial volcanic eruption using ground-based C-band radar imagery." *IEEE Transactions on Geoscience and Remote Sensing*, 48:403-414.
- Mastin, L. (1997), Evidence for water influx from a caldera lake during the explosive hydromagmatic eruption of 1970, Kilauea volcano, Hawaii, *Journal of Geophysical Research*, 102, B9, doi: 10.1029/97JB0142.
- Mastin, L. (2001), EJECT! A program for the calculation of ballistic trajectories of volcanic blocks, U.S. Geological Survey Open-File Report 01-45 (13 pp.).
- Matar, O.K., P.D.M. Spelt, and F. Stepanek (2006), Collisions of liquid coated solid spherical particles in viscous fluid, *Journal of Colloid and Interface Science*, 301, 594-606, doi: 10.1016/j.jcis.2006.05.026.
- Mather, T.A. and R.G. Harrison (2006), Electrification of volcanic plumes, *Surv. Geophysics*, 27, 387-432, doi: 10.1007/s10712-006-9007-2.
- McPhie, J., G. Walker, and R.L. Christiansen (1990), Phreatomagmatic and phreatic fall and surge deposits from explosions at Kilauea volcano, Hawaii, 1790 A.D.: Keanakakoi Ash Member, *Bulletin of Volcanology*, 52, 334-354, doi: 10.1007/BF00302047.
- Mikhailov, E., Vlasenko, S., Martin, S., Koop, T. and Poschl, U., 2009. "Amorphous and crystalline aerosol particles interacting with water vapor: conceptual framework and experimental evidence for restructuring, phase transitions and kinetic limitations." *Atmos. Chem. Phys.*, 9:9491-9522.
- Montgomery, D.N., 1971. "Collision and coalescence of water droplets." *Journal of Atmospheric Sciences*, 28:292-293.
- Morrissey, M., B. Zimanowski, K. Wohletz and R. Buettner (2000), Phreatomagmatic Fragmentation, In: Sigurdsson, H. (ed) *Encyclopedia of Volcanoes*, Academic Press, San Diego, 421-430.
- Niemeier, U., Timmreck, C., Graf, H., Kinne, S., Rast, S. and Self, S., 2009. "Initial fate of fine ash and sulfur from large volcanic eruptions." *Atmospheric Chemistry and Physics Discussions*, 9:17531-17577.

- Orme, M., 1997. "Experiments on droplet collisions, bounce, coalescence and disruption." *Prog. Energy Combust. Science*, 23:65-79.
- Prasad, A., 2000. "Particle image velocimetry." *Current Science*, 79:51-60.
- Prata, A.J. and Tupper, A., 2009. "Aviation hazards from volcanoes: the state of the science." *Natural Hazards*, 51:239-244.
- Raju, N. and Meiburg, E., 1995. "The accumulation and dispersion of heavy particles in forced two-dimensional mixing layers. Part 2: The effect of gravity." *Phys. Fluids*, 7:1241-1264.
- Robock, A., 2000. "Volcanic eruptions and climate." *Reviews of Geophysics*, 38:191-219.
- Rose, W., 1977. "Scavenging of volcanic aerosol by ash: Atmospheric and volcanologic implications." *Geology*, 5:621-624.
- Rose, W.I., and A.J. Durant (2009), Fine ash content of explosive eruptions, *Journal of Volcanology and Geothermal Research*, 186, 32-39, doi: 10.1016/j.jvolgeores.2009.01.010.
- Rose, W.I., and A.J. Durant (2011), Fate of volcanic ash: Aggregation and fallout, *Geology*, 39(9), 895-896, doi: 10.1130/focus092011.1.
- Samaniego, P., Le Pennac, J., Robin, C. and Hidalgo, S., 2011. "Petrological analysis of the pre-eruptive magmatic process prior to the 2006 explosive eruptions at Tungurahua volcano (Ecuador)." *Journal of Volcanology and Geothermal Research*, 199:69-84.
- Santiago, J., Wereley, S., Meinhart, C., Beebe, D., and Adrian, R., 1998. "A particle image velocimetry system for microfluids." *Experiments in Fluids*, 25:316-319.
- Schmeeckle, M.W., J.M. Nelson, J. Pitlick, and J.P. Bennett (2001), Interparticle collision of natural sediment grains in water, *Water Resources Research*, 37(9), 2377-2391, doi: 10.1029/2001WR000531.
- Schumacher, R. and Schmincke, H., 1995. "Models for the origin of accretionary lapilli." *Bulletin of Volcanology*, 56:626-639.
- Schumann, U., B. Weinzierl, O. Reitebuch, H. Schlager, A. Minikin, C. Forster, R. Baumann, T. Sailer, K. Graf, H. Mannstein, C. Voigt, S. Rahm, R. Simmet, M. Scheibe, M. Lichtenstern, P. Stock, H. Rueba, D. Schaeuble, A. Tafferner, M. Rautenhaus, T. Gerz, H. Ziereis, M. Krautstrunk, C. Mallaun, J.-F. Gayet, K. Lieke, K. Kandler, M. Ebert, S. Weinbruch, A. Stohl, J. Gasteiger, S. Gross, V. Freudenthaler, M. Wiegner, A. Ansmann, M. Tesche, H. Olafsson, and K. Sturm

- (2011), Airborne observations of the Eyjafjalla volcano ash cloud over Europe during air space closure in April and May 2010, *Atmospheric Chemistry and Physics*, 11, 2245-2279, doi: 10.5194/acp-11-2245-2011.
- Scollo, S., P. Del Carlo, and M. Coltelli (2007), Tephra fallout of 2001 Etna flank eruption: Analysis of the deposit and plume dispersion, *Journal of Volcanology and Geothermal Research*, 160, 147-164, doi: 10.1016/j.volgeores.2006.09.007.
- Scollo, S., Folch, A. and Costa, A., 2008. "A parametric and comparative study of different tephra fallout models." *Journal of Volcanology and Geothermal Research*, 176:199-211.
- Scott, W.E., and R.G. McGimsey (1994), Character, mass, distribution, and origin of tephra-fall deposits of the 1989-1990 eruption of Redoubt Volcano, south-central Alaska, *Journal of Volcanology and Geothermal Research*, 62, 251-272.
- Stevenson, J.A., S. Loughlin, C. Rae, T. Thordarson, A.E. Milodowski, J.S. Gilbert, S. Harangi, R. Lukács, B. Højgaard, U. Árting, S. Pyne-O'Donnell, A. MacLeod, B. Whitney, and M. Cassidy (2012), Distal deposition of tephra from the Eyjafjallajökull 2010 summit eruption, *Journal of Geophysical Research*, 117, doi: 10.1029/2011JB008904.
- Swanson, D.A., S.P. Zolkos, and B. Haravitch (2012a), Ballistic blocks around Kilauea Caldera: Their vent locations and number of eruptions in the late 18<sup>th</sup> century, *Journal of Volcanology and Geothermal Research*, 231, 1-11, doi: 10.1016/j.jvolgeores.2012.04.008.
- Swanson, D.A., T.R. Rose, R.S. Fiske and J.P. McGeehin (2012b), Keanakāko'I Tephra produced by 300 years of explosive eruptions following collapse of Kīlauea's caldera in about 1500 CE, *Journal of Volcanology and Geothermal Research*, 215, 8-25, doi:10.1016/j.jvolgeores.2011.11.009.
- Taddeucci, J., P. Scarlato, C. Montanaro, C. Cimarelli, E. Del Bello, C. Freda, D. Andronico, M.T. Gudmundsson, and D.B. Dingwell (2011), Aggregation-dominated ash settling from the Eyjafjallajökull volcanic cloud illuminated by field and laboratory high-speed imaging, *Geology*, 39(9), 891-894, doi: 10.1130/G32016.1.
- Telling, J., and J. Dufek (2012), An experimental evaluation of ash aggregation in explosive volcanic eruptions, *Journal of Volcanology and Geothermal Research*, 209, 1-8, doi:10.1016/j.jvolgeores.2011.09.008.
- Telling, J., J. Dufek and A. Shaikh (2013), Ash aggregation in explosive volcanic eruptions, *Geophysical Research Letters*, 40, doi:10.1002/grl.50376.

- Textor, C., H.F. Graf, M. Herzog, J.M. Oberhuber, W.I. Rose, and G.G.J. Ernst (2006a), Volcanic particle aggregation in explosive eruption columns. Part I: Parameterization of the microphysics of hydrometers and ash, *Journal of Volcanology and Geothermal Research*, 150, 359-377, doi:10.1016/j.jvolgeores.2005.09.007.
- Textor, C., H.F. Graf, M. Herzog, J.M. Oberhuber, W.I. Rose, and G.G.J. Ernst (2006b), Volcanic particle aggregation in explosive eruption columns. Part II: Numerical experiments, *Journal of Volcanology and Geothermal Research*, 150, 378-394, doi:10.1016/j.jvolgeores.2005.09.008.
- Tomita, K., T. Kanai, T. Kobayashi, and N. Oba (1985), Accretionary lapilli formed by the eruption of Sakurajima volcano, *J. Japan Assoc. Min. Petr. Econ. Geol.*, 80, 49-54.
- Vallance, J.W. (2000), Lahars, In: Sigurdsson, H. (ed) *Encyclopedia of Volcanoes*, Academic Press, San Diego, 601-616.
- Van Eaton, A.R., M. Herzog, C.J.N. Wilson, and J. McGregor (2012), Ascent dynamics of large phreatomagmatic eruption clouds: The role of microphysics, *Journal of Geophysical Research*, 117, doi:10.1029/2011JB008892.
- Van Eaton, A.R., J.D. Muirhead, C.J.N. Wilson, and C. Cimarelli (2012b), Growth of volcanic ash aggregates in the presence of liquid water and ice: an experimental approach, *Bulletin of Volcanology*, 74(9), doi:10.1007/s00445-012-0634-9.
- Van Eaton, A.R. and C. Wilson (2013), The nature, origins and distribution of ash aggregates in a large-scale wet eruption deposit: Oruanui, New Zealand, *Journal of Volcanology and Geothermal Research*, 250, 129-154, doi: 10.1016/j.jvolgeores.2013.10.016.
- Veitch, G., and A.W. Woods (2001), Particle aggregation in volcanic eruption columns, *Journal of Geophysical Research*, 106(B11), 26,425-26,441, doi: 10.1029/2000JB900343.
- Walker, G.P.L. (2000), Basaltic volcanoes and volcanic systems, In: Sigurdsson, H. (ed) *Encyclopedia of Volcanoes*, Academic Press, San Diego, 283-289.
- Wilson, L. and J.W. Head (2007), Explosive volcanic eruptions on Mars: Tephra and accretionary lapilli formation, dispersal and recognition in the geologic record, *Journal of Volcanology and Geothermal Research*, 163, 83-97, doi: 10.1016/j.jvolgeores.2007.03.007.
- Yamamoto, H., K. Takayama, and K. Ishikawa (2008), Model experiment on magma fragmentation in explosive volcanic, *Journal of Mineralogical and Petrological Sciences*, 103, 192-203, doi: 10.2465/jmps.060905.

Zimanowski, B., K. Wohletz, P. Dellino, and R. Büttner (2003), The volcanic ash problem, *Journal of Volcanology and Geothermal Research*, 122, 1-5, doi: 10.1016/s0377-0273(02)00471-7.